

MINISTÉRIO DA EDUCAÇÃO  
UNIVERSIDADE FEDERAL DO RIO GRANDE DO SUL  
ESCOLA DE ENGENHARIA  
PROGRAMA DE PÓS-GRADUAÇÃO EM ENGENHARIA DE MINAS,  
METALÚRGICA E DE MATERIAIS – PPGE3M

**THIAGO MARQUES IVANISKI**

PREVISÃO DE TAMANHO DE GRÃO DE AÇO BAINÍTICO FORJADO  
ASSISTIDA POR SIMULAÇÃO NUMÉRICA

Porto Alegre

2022

**THIAGO MARQUES IVANISKI**

**PREVISÃO DE TAMANHO DE GRÃO DE AÇO BAINÍTICO FORJADO  
ASSISTIDA POR SIMULAÇÃO NUMÉRICA**

Tese realizada no Departamento de Metalurgia da Escola de Engenharia da Universidade Federal do Rio Grande do Sul (UFRGS), no âmbito do Programa de Pós-Graduação em Engenharia de Minas, Metalúrgica e de Materiais (PPGE3M) e com a colaboração do Instituto de Conformação Mecânica (IBF – RWTH-Aachen) e o Instituto de Tecnologia Orientada a Materiais (IWT – Bremen) – Alemanha, como parte dos requisitos para a obtenção do título de Doutor em Engenharia – Área de Concentração: Processos de Fabricação.

Orientador: Prof. Dr. Alexandre da Silva Rocha

Porto Alegre

2022

**UNIVERSIDADE FEDERAL DO RIO GRANDE DO SUL**

Reitor: Prof. Dr. Carlos André Bulhões Mendes

Vice-Reitora: Profa. Patrícia Helena Lucas Pranke

**ESCOLA DE ENGENHARIA**

Diretora: Profa. Dra. Carla Schwengber ten Caten

Vice-Diretor: Prof. Dr. Afonso Reguly

**PROGRAMA DE PÓS-GRADUAÇÃO EM ENGENHARIA DE MINAS, METALÚRGICA E  
DE MATERIAIS – PPGE3M**

Coordenador: Prof. Dr. Afonso Reguly

**THIAGO MARQUES IVANISKI**

**PREVISÃO DE TAMANHO DE GRÃO DE AÇO BAINÍTICO FORJADO  
ASSISTIDA POR SIMULAÇÃO NUMÉRICA**

Esta Tese foi analisada e julgada adequada para a obtenção do Título de Doutor em Engenharia – Área de Concentração: Processos de Fabricação, e aprovada em sua forma final pelo Orientador e pela Banca Examinadora designada pelo Programa de Pós-Graduação em Engenharia de Minas, Metalúrgica e de Materiais (PPGE3M), da Escola de Engenharia da Universidade Federal do Rio Grande do Sul (UFRGS).

Prof. Dr. Alexandre da Silva Rocha (PPGE3M -UFRGS)

Orientador

Prof. Dr. Afonso Reguly

Coordenador do PPGE3M -UFRGS

**Aprovado com Louvor em: 23/09/2022**

**Banca Examinadora:**

Dr. Eng. Alberto Moreira Brito

Prof. Dr. Mario Wolfart Junior

Prof. Dr. Tiago Cristofer Aguzzoli Colombo

*“ Seja a mudança que você quer ver no mundo ”*

**Mahatma Gandhi**

## **AGRADECIMENTOS**

Ao meu orientador, Professor Dr. Eng. Alexandre da Silva Rocha, pela grandiosa oportunidade que me foi dada durante a minha trajetória acadêmica no PPGE3M-UFRGS. Pelo conhecimento compartilhado. Muito obrigado.

Aos meus colegas do Laboratório de Transformação Mecânica (LdTM-UFRGS) e ao Grupo de Engenharia de Superfícies (GES), pela troca de conhecimento e todo apoio durante a condução deste trabalho.

Aos Professores, Dr. Ing. Lírío Schaeffer e Dr. Ing. Gehart Hirt por possibilitar a condução de parte dos experimentos deste trabalho na Universidade Técnica de Aachen (RWTH-Aachen), Alemanha. Em especial a Msc. Eng. Michel Henze e toda a equipe do grupo IBF- RWTH-Aachen.

Ao Dr. Ing. Jérémy Épp, pela oportunidade de adquirir experiência em caracterização de materiais durante o período sanduíche no Leibniz-Institut für Werkstofforientierte Technologien IWT-Bremen, Alemanha.

A agência de fomento do Conselho Nacional de Desenvolvimento Científico e Tecnológico MCTI/CNPq pela concessão da bolsa de doutorado processo n° 167948/2017-2.

A Coordenação de Aperfeiçoamento de Pessoal de Nível Superior CAPES pelo apoio ao desenvolvimento do projeto “Manufatura Energeticamente Eficiente para Aços Bainíticos Avançados Baseada no Processamento Termomecânico” através do auxílio de número 1844/2017 e pelo financiamento bolsa de estudos sanduíche (n° do processo 99999.000290/2016-05), no âmbito do programa “Iniciativa Brasil-Alemanha para Pesquisa Colaborativa em Tecnologia de Manufatura - BRAGECRIM”.

Aos meus pais Alexandre e Cláudia, irmãos Alexandra e Milaine, a minha noiva, Paula, por todo amor e apoio durante essa longa aventura chamada “vida acadêmica”.

## RESUMO

Aços bainíticos avançados de resfriamento contínuo podem substituir materiais que passam pelo processo de têmpera e revenimento (**T&R**) sendo, desta forma, econômicos e benéficos ao meio ambiente. No entanto, para se obter mais eficiência energética é necessário compreender a sinergia dos parâmetros de forjamento a quente, a qual trará como resposta diferentes microestruturas. Sendo uma delas, a evolução na estrutura dos grãos. Indubitavelmente, a predição das transformações microestruturais por tais parâmetros complexos é importantíssima para fabricação de produtos forjados de precisão. O modelo semi-empírico de *Johnson-Mehl-Avrami-Kolmogorov* JMAK é uma excelente ferramenta para a predição e o controle de grão austenítico durante o processamento termomecânico. Porém, a acuracidade dos resultados obtidos com modelos complexos é reduzida devido a suposições que levam a uma inadequada calibração, causada por gradientes de temperatura, diferentes sítios de nucleação, e devido à distribuição de deformações. Portanto, é um desafio em aplicações industriais a implementação da simulação de tamanho de grão austenítico. Este trabalho teve como objetivo desenvolver estratégias de calibração por simulação numérica computacional para o forjamento de um novo aço bainítico por resfriamento contínuo. De modo que seja permitido verificar a influência que diferentes parâmetros de forjamento a quente implicam no tamanho de grão austenítico. Na primeira parte, buscou-se investigar a aplicabilidade da simulação do grão, utilizando modelo de JMAK no forjamento em matriz aberta do aço DIN 20MnCr5. A seguir, foram modeladas matematicamente as curvas de escoamento plástico de um novo aço bainítico livre de carbonetos, denominado nesta tese como DIN 18MnCrSiMo6-4, para a futura implementação em software de simulação computacional. O êxito desta aquisição permitiu constituir um modelo reológico com o uso das equações cinéticas de Arrhenius e de JMAK, para o qual adquiriu-se os parâmetros de encruamento, recuperação e recristalização dinâmica dependentes das curvas de escoamento. Foram realizados testes industriais de forjamento em matriz fechada de uma pré-forma de engrenagem helicoidal em altas taxas de deformação e diferentes temperaturas. Criou-se um modelo computacional para simular o processo industrial, mostrando que, as equações utilizadas, bem como a modificação realizada na dependência dos parâmetros de crescimento de grão mitigou a diferença entre valores experimentais e simulados. Com a caracterização microestrutural, avaliou-se a dependência da temperatura de forjamento, correlacionando o tamanho de grão com as propriedades mecânicas após o resfriamento contínuo.

**Palavras-chave:** Aços bainíticos avançados, Forjamento a Quente, Evolução Microestrutural, Simulação Numérica

## ABSTRACT

Advanced continuous cooling bainitic steels can replace materials that go through the quenching and tempering (Q&T) process, thus being economical and beneficial to the environment. However, to obtain more energy efficiency it is necessary to understand the synergy of the hot forging parameters, which will bring different microstructures as a response. One of them is the evolution in the structure of the grains. Undoubtedly, the prediction of microstructural transformations by such complex parameters is very important for the manufacture of precision forged products. The Johnson-Mehl-Avrami-Kolmogorov JMAK semi-empirical model is an excellent tool for predicting and controlling austenitic grain during thermomechanical processing. However, the accuracy of the results obtained with complex models is reduced due to assumptions that lead to an inadequate calibration caused by temperature gradients, different nucleation sites, and due to the distribution of strains. Therefore, it is challenging in industrial applications to implement austenitic grain size simulation. This work aimed to develop calibration strategies by computational numerical simulation to forging new bainitic steel by continuous cooling. So that it is possible to verify the influence that different hot forging parameters have on the austenitic grain size. In the first part, we sought to investigate the applicability of the grain simulation using a JMAK model in the open-die forging of a DIN 20MnCr5 steel. Next, the plastic flow curves of a new carbide-free bainitic steel, named in this thesis as DIN 18MnCrSiMo6-4, were mathematically modeled for future implementation in computer simulation software. The success of this acquisition allowed the construction of a rheological model using the Arrhenius and JMAK kinetic equations, for which the parameters of hardening, recovery, and dynamic recrystallization dependent on the flow curves were acquired. Industrial tests of closed die forging of a helical gear preform were carried out at high strain rates and different temperatures. A computational model was created to simulate the industrial process, showing that the equations used and the modification carried out depending on the grain growth parameters mitigated the difference between experimental and simulated values. With the microstructural characterization, the dependence of the forging temperature was evaluated, correlating the grain size with the mechanical properties after continuous cooling.

**Keywords:** Advanced bainitic steels, Hot Forging, Microstructural Evolution, Numerical Simulation, Efficiency.

## **PUBLICAÇÕES RELACIONADAS A ESTA TESE**

IVANISKI, T. M. et al. Numerical and experimental study of an industrial case for grain size evolution in bainitic steel in controlled hot forging and its influence on mechanical performance. *Materials Research*, [s. l.], v. 25, n. 1, 2022.

IVANISKI, T. M. et al. Constitutive Modelling of High Temperature Flow Behaviour for a Low Carbon High Silicon Bainitic Steel. *Materials Research*, [s. l.], v. 23, n. 5, 2020.

IVANISKI, T. M. et al. Austenitic grain size prediction in hot forging of a 20MnCr5 steel by numerical simulation using the JMAK model for industrial applications. *Materials Research*, [s. l.], v. 22, n. 5, 2019.

IVANISKI, T. M.; HATWIG, R. A.; DONG, J.; ÉPP, JÉRÉMY; ZOCH, H-W.; ROCHA, A. S. An approach using JMAK model in numerical simulation to control of austenitic grain size in hot forming In: *International Forging Conference, 39th SENAFOR, 2019.*, 2019, Porto Alegre.

IVANISKI, T. M.; ÉPP, JÉRÉMY; ROCHA, A. S. Determination of austenitic grain size in hot forming as a function of its variables with the application of subroutines in numerical simulation In: *International Forging Conference, 41th SENAFOR, 2022.*, 2022, Porto Alegre.

IVANISKI, T. M.; HATWIG, R. A.; ROCHA, A. S., Uma abordagem usando o modelo JMAK na simulação computacional para o controle no tamanho de grão em forjamento a quente. *Revista Forge (Versão Impressa)*., p.14 - 19, 2019.

CASTRO, P. J. de; SILVEIRA, A. C.; IVANISKI, T. M.; TURRA, C. J; EPP, J; ROCHA, A. da Silva. Two-Step Continuous Cooling Heat Treatment Applied in a Low Carbon Bainitic Steel. *Materials Research*, [s. l.], v. 24 n. 2, 2021.

## SUMÁRIO

<b>RESUMO.....</b>	<b>XI</b>
<b>ABSTRACT.....</b>	<b>XIII</b>
<b>PUBLICAÇÕES RELACIONADAS A TESE.....</b>	<b>X</b>
<b>CAPÍTULO 1 - INTRODUÇÃO.....</b>	<b>1</b>
1. Introdução.....	1
1.1 Objetivos.....	6
1.1.1 Objetivo geral .....	6
1.1.2 Objetivos Específicos .....	6
<b>CAPÍTULO 2 – INTEGRAÇÃO DOS ARTIGOS CIENTÍFICOS .....</b>	<b>7</b>
2.1 Viabilização do modelo em macro escala no controle do tamanho de grão austenítico em forjamento a quente .....	7
2.2 Constituição dos modelos matemáticos para as curvas de escoamento do aço bainítico DIN 18MnCrSiMo6-4 e os modelos de recristalização.....	8
2.3 Implementação e validação numérica computacional de um novo aço bainítico em processos industriais de forjamento .....	8
<b>CAPÍTULO 3 – ARTIGOS PUBLICADOS .....</b>	<b>10</b>
3.1 Austenitic grain size prediction in hot forging of a 20mncr5 steel by numerical simulation using the JMAK model for industrial applications.....	11
3.1.1 Introduction .....	11
3.1.2 Materials and Methods .....	13
3.1.2.1 Acquiring the Experimental Data.....	13
3.1.2.2 Boundary Conditions for Simulation.....	14
3.1.2.3 Recrystallization Modelling .....	15
3.1.3 Results and Discussion .....	16

3.1.4 Conclusions .....	24
Acknowledgements .....	24
3.1.8 References .....	24
3.2 Constitutive Modelling of High Temperature Flow Behaviour for a Low Carbon High Silicon Bainitic Steel .....	28
3.2.1 Introduction .....	28
3.2.2 Experimental procedures .....	30
3.2.3 Results and Discussion .....	32
3.2.3.1 Flow Curves.....	32
3.2.3.2 Parametrization of Arrhenius Equation .....	35
3.2.3.3 Determination of recovery (DRV) and (DRX) parameters ( $\sigma_{WH}$ , $\sigma_{sat}$ , $\sigma_p$ , $\sigma_c$ , $\sigma_{ss}$ , $\epsilon_c$ , $\epsilon_p$ ) .....	37
3.2.3.4 Analysis of the Dynamic Recrystallization DRX Kinetics .....	43
3.2.3.5 Modelling Flow Curves .....	46
3.2.4 Conclusions.....	48
Acknowledgement .....	49
3.2.5 References .....	49
3.3 Numerical and experimental study of an industrial case for grain size evolution in bainitic steel in controlled hot forging and its influence on mechanical performance.....	53
3.3.1 Introduction .....	53
3.3.2 Materials and Methods .....	55
3.3.2.1 Grain Growth Kinetic of Annealing test.....	55
3.3.2.2 Flow Curves and Microstructure Analysis .....	57
3.3.2.3 Metallography Analysis.....	57
3.3.2.4 Recrystallization Model.....	58
3.3.2.5 Forging Trial and Numerical Modeling.....	62

3.3.2.6 Strength and Toughness Analysis.....	65
3.3.3 Results and Discussion .....	66
3.3.3.1 Grain Growth Model of Annealing .....	66
3.3.3.2 Model Validation.....	68
3.3.4 Industrial Application .....	74
3.3.4.1 Microstructure Simulation in the bainitic steel .....	74
3.3.4.2 Grain Growth Simulation after Hot Forging .....	77
3.3.4.3 Mechanical Properties response .....	79
3.3.5 Conclusion.....	83
Acknowledgement.....	84
3.3.6 References .....	85
<b>CAPÍTULO 4 - CONCLUSÕES.....</b>	<b>89</b>
4.1 Conclusões gerais da pesquisa.....	89
4.2 Sugestões para trabalhos futuros .....	91
4.3 Referências complementares .....	92
<b>APÊNDICE 1A Difração de Elétrons Retroespalhados (Back Scattering Diffraction-EBSD) por microscopia eletrônica de varredura (MEV) .....</b>	<b>96</b>
<b>APÊNDICE 1B Curvas de Escoamento e Validação da Força de Recalque.....</b>	<b>99</b>
<b>APÊNDICE 1C Implementação de uma nova sub-rotina no software QFORM UK. ....</b>	<b>101</b>

## LISTA DE FIGURAS

### ARTICLE #1

<b>Figure 3.1.1.</b> Conceptual scheme of experiments.....	14
<b>Figure 3.1.2.</b> Modelling proposed. ....	14
<b>Figure 3.1.3.</b> Conceptual flowchart used to compare experimental results and computational simulation. ....	15
<b>Figure 3.1.4.</b> Numerical results of temperature fields after 40% and 60% height reduction. ....	17
<b>Figure 3.1.5.</b> Numerical results of (a) Effective strain, (b) Average Strain rate. ....	17
<b>Figure 3.1.6.</b> (a) Von Mises stress field, (b) Fiberling and effect of stress triaxiality.....	18
<b>Figure 3.1.7.</b> Numerical results of (a) Dynamically recrystallized fraction ( $X_{DRX}$ ), (b) Zener-Hollomon parameter. ....	19
<b>Figure 3.1.8.</b> Numerical results of (a) Average grain size in the forging instant, (b) Average grain size after quenching.....	20
<b>Figure 3.1.9.</b> (a) Metadyninamic recrystallized fraction ( $M_{DRX}$ ), (b) Static recrystallized fraction ( $S_{RX}$ ).....	21
<b>Figure 3.1.10.</b> Experimental macrography and austenitic grain size results for forged and water quenched samples. Picral etching with 3vol. % Picric Acid in destined water.....	23
<b>Figure 3.1.11.</b> Numerical results of (a) Flow curves generated in different regions of the workpiece, (b) $X_{DRX}$ cycles response. ....	23
<b>Figure 3.1.12.</b> Average grain size comparison between experimental results and calculated.....	23

### ARTICLE #2

<b>Figure 3.2.1.</b> As-received microstructure revealed by optical microscopy of the DIN 18MnCrSiMo6-4. ....	31
<b>Figure 3.2.2.</b> Representation of the hot compression tests. ....	31
<b>Figure 3.2.3.</b> True Stress versus True Strain curves of studied steel at four different strain rates and temperatures (a) $0.1 \text{ s}^{-1}$ , (b) $0.5 \text{ s}^{-1}$ , (c) $1 \text{ s}^{-1}$ , (d) $5 \text{ s}^{-1}$ . ....	33
<b>Figure 3.2.4.</b> Surface plot of the effect of strain rate and temperature on the strain rate sensitivity at 0.5 of plastic deformation. ....	34

<b>Figure 3.2.5.</b> Peak stress and peak strain relationship to determine the coefficients: (a) $n'$ , (b) $\beta$ , (c) $n$ , (d) $Q$ .	35
<b>Figure 3.2.6.</b> Linear correlation between $\log[\sinh a\sigma]$ and $\log Z$ under different hot work conditions for the bainitic steel.	37
<b>Figure 3.2.7.</b> $\theta$ - $\sigma$ curves on different temperatures and strain rates: (a) 1123 K; (b) 1223 K; (c) 1323 K; (d) 1423 K.	38
<b>Figure 3.2.8.</b> Plot of $\theta\sigma$ vs. $\sigma^2$ employed to determine the slope $m$ for the steel at different temperatures and strain rates.	39
<b>Figure 3.2.9.</b> Athermal work hardening ( $h$ ) as a function of peak stress for DIN 18MnCrSiMo6-4 steel.	41
<b>Figure 3.2.10.</b> Linear relationship between (a) $\sigma_p$ , $\sigma_c$ , $\varepsilon_c$ , $\varepsilon_p$ and (b) Steady-state stress for $Z$ parameter.	42
<b>Figure 3.2.11.</b> JMAK plot for 18MnCrSiMo6-4 during the hot compression showing the effect of the temperature in the softening rate.	44
<b>Figure 3.2.12.</b> $X_{DRX}$ volume fraction of recrystallized grains during the hot working condition as a function of (a) Temperature, (b) Strain rate.	45
<b>Figure 3.2.13.</b> Comparison between experiment flow curves and the two different models with high strain extrapolation for the DIN 18MnCrSiMo6-4 steel for different strain rates and temperatures, (a) Strain rate $0.1s^{-1}$ , (b) $0.5s^{-1}$ , (c) $1s^{-1}$ and (d) $5s^{-1}$ .	47

### ARTICLE #3

<b>Figure 3.3.1.</b> (a) 1 PAGES as received $23,5 \mu m$ , (b) 2 Initial Microstructure BF – Bainitic Ferrite, GB – Granular Bainite, PF – Polygonal Ferrite, A – Retained Austenite, M – Martensite.	56
<b>Figure 3.3.2.</b> Flowchart of modeling interaction to calibrate the experiment.	58
<b>Figure 3.3.3.</b> (a) Thermomechanical routes on industrial environment steps, (b) Experiment forged samples indicating the regions of metallography analysis.	63
<b>Figure 3.3.4.</b> The axisymmetric model implemented in DEFORM for gear forging and a cross-section of the simulated forging profile of the preform showing the analyzed areas. 1 - Billet, 2 - Upper die, 3- Lower die, 4 - Knock-off.	64
<b>Figure 3.3.5.</b> Representative and machined zone of collected samples for the micro-tensile and Charpy V-notch.	66

<b>Figure 3.3.6.</b> Modeled Annealing curves for 18MnCrSiMo6-4 steel; (a) Natural logarithm of grain size and time, (b) Grain size and inverse of temperature, (c) Comparison between experiment and simulation grain growth evolution.....	67
<b>Figure 3.3.7.</b> (a) Modeled flow curves and predicted for high strain rates on temperature dependence [9], (b) $X_{DRX}$ kinetics on strain rate dependence, modeled and predicted, (c) Comparison between experiment and prediction of a load of a compression test, (d) FEM recrystallization results.....	70
<b>Figure 3.3.8.</b> Simulation of austenitic grain size in isothermal compression test (a) 950 °C 0.1 (1/s), (b) 1150 °C 1150 °C 0.1 (1/s).....	71
<b>Figure 3.3.9.</b> Predicted austenitic grain size of hot compressed samples $\epsilon = 0.69$ .....	72
<b>Figure 3.3. 10.</b> EBSD map showing the temperature dependence in different sizes of crystallographic units. (a) P3 - T = 950 °C / $\epsilon = 0.1 \text{ s}^{-1}$ , (b)P3 - T = 1150 °C / $\epsilon = 0.1 \text{ s}^{-1}$ .....	73
<b>Figure 3.3.11.</b> Histogram of measured crystallographic units grain sizes, (a) T = 950 °C / $\epsilon = 0.1 \text{ s}^{-1}$ , (b) T = 1150 °C / $\epsilon = 0.1 \text{ s}^{-1}$ .....	73
<b>Figure 3.3.13.</b> Simulated evolution of (a) average strain rate ( $\epsilon$ ) and (b) effective strain ( $\epsilon$ ) on the industrial preform forged gear.....	75
<b>Figure 3.3.14.</b> Recrystallization kinetics of the modeled pre-form hot forged; (a) $X_{DRX}$ ; (b) $M_{DRX}$ ; (c) $S_{RX}$ .....	76
<b>Figure 3.3.15.</b> X-Y Plane view of the grain size evolution computed on the tracked points: (a) Forged at 1030 °C, (b) Forged at 1130 °C.....	78
<b>Figure 3.3.16.</b> Local austenitic grain size comparison after industrial hot forging between experiment and numerical simulation results.....	79
<b>Figure 3.3.17.</b> Austenitic grain and continuously cooled microstructure in R2 region: (a,b) and (c) Forged at 1030 °C, quenched and cooled in calm air; (d,e) and (f) forged at 1130 °C quenched and cooled in calm air.....	80
<b>Figure 3.3. 18.</b> Boxplot results of the (a) Yield stress YS and (b) Ultimate stress US in MPa....	81
<b>Figure 3.3. 19.</b> (a) Impact energy through of Charpy- V notch tests; (b) Local Elongation in %.	82
<b>Figure 3.3. 20.</b> SEM results of the micro-tensile specimen regions showing the final continuous cooled microstructure of pre-form gear. (a) R1, (b) R2 and (c) R3 Forged at 1030 °C; (d) R1, (e) R2 and (f) R3 Forged at 1130 °C, respectively.....	82

## LISTA DE TABELAS

### ARTICLE #1

<b>Table 3.1.1.</b> Chemical composition of the experimental DIN 20MnCr5.....	13
<b>Table 3.1.2.</b> Boundary conditions used in the numerical computational simulation from the data collected in experiments. ....	15
<b>Table 3.1.3.</b> Equations to describe the microstructure evolution.....	16

### ARTICLE #2

<b>Table 3.2.1.</b> Chemical composition of the experimental DIN 18MnCrSiMo6-4. ....	30
<b>Table 3.2.2.</b> Dynamic recovery parameter ( $r$ ) obtained from the flow curves of DIN 18MnCrSiMo6-4. ....	40

### ARTICLE #3

<b>Table 3.3.1.</b> Chemical composition for steel 18MnCrSiMo6-4, mass percentage. ....	55
<b>Table 3.3.2.</b> Processing conditions in the industrial forging experiments. ....	63
<b>Table 3.3.3.</b> Thermal properties in the numerical model.....	65
<b>Table 3.3.4.</b> Constants used in DEFORM® after calibration of the experiment for microstructural modeling of DIN 18MnCrSiMo6-4 steel.....	69
<b>Table 3.3.5.</b> Values of $m$ exponent implemented in DEFORM®, computed as a temperature function in non-isothermal condition after $D_{RX}$ , $M_{DRX}$ and $S_{RX}$ .....	77

## **LISTA DE ABREVIATURAS E SIGLAS**

AISI	American Iron and Steel Institute
ASTM	American Society for Testing and Materials
CC	Continuous Cooling
DIN	Deutsches Institut für Normung
DRX	Dynamic Recrystallization
DDRX	Dynamic Recrystallized Grain Size
DMDRX	Metadynamic Recrystallized Grain Size
DRV	Dynamic Recovery
DSRX	Static Recrystallized Grain Size
EBSD	Energy Backscattering Spectroscopy Dispersive
EDM	Electrical Discharge Machining
FEM	Finite Element Simulation
GS	Grain Size
HT	Heat Treatment
IBF	Institut Für Bildsame Formgebung
ISO	International Organization for Standardization
IWT	Institut für Werkstofforientierte Technologien
JMAK	Johnson-Mehl-Avrami-Kolmogorov
LdTM	Laboratório de Transformação Mecânica
LVDT	Linear Variable Displacement Transducer

MEF	Método de Elementos Finitos
PAGS	Prior Austenitic Grain Size
Q & T	Quenching and Tempering
RWTH	Rheinisch-Westfälische Technische Hochschule
SAE	Society of Automotive Engineers
SEM	Scanning Electron Microscopy
T & R	Têmpera e Revenido
XDRX	Dynamic Recrystallized Fraction
XMDRX	Metadynamic Recrystallized Fraction
XSRX	Static Recrystallized Fraction
WH	Work Hardening

## LISTA DE SÍMBOLOS

### ARTICLE #1

$\varphi$	[mm/mm]	Effective Strain
$\varphi_c$	[mm/mm]	Critical Strain
$\dot{\varphi}$	[s <sup>-1</sup> ]	Effective Strain rate
$Q_{DRX}$	[J/mol.K]	Activation Energy to recrystallization
$n$	[-]	Avrami Exponent
$b$	[ $m$ ]	Avrami Coefficient
$t$	[s]	Time
$\bar{m}$	[-]	Friction factor
$\mu$	[-]	Friction coefficient
$d_0$	[ $\mu\text{m}$ ]	Initial Grain Size
$\varphi_{0.5}$	[-]	Strain at 50% of Recrystallization
$R$	[J/mol.K]	Gas Constant
$T$	[K or °C]	Temperature
$t_{0.5}$	[s]	Time at 50% of Recrystallization
$d_{gg}$	[ $\mu\text{m}$ ]	Final grain growth
$Z$	[s <sup>-1</sup> ]	Zenner- Hollomon Parameter
$\sigma$	[MPa]	True Stress
$X$	[-]	Recrystallized Fraction

### ARTICLE #2

$\varepsilon$	[mm/mm]	Strain
$\varepsilon_c$	[mm/mm]	Critical Strain
$\varepsilon_p$	[mm/mm]	Peak Strain
$\dot{\varepsilon}$	[s <sup>-1</sup> ]	Strain rate

Q	[J/mol.K]	Flow curves Activation Energy
$n'$	[MPa]	Numerical Coefficient
$\beta$	[-]	Numerical Coefficient
$\alpha$	[MPa <sup>-1</sup> ]	Material parameter of Peak Stress
n	[-]	Material Constant
m	[-]	Numerical Coefficient
A'	[s <sup>-1</sup> ]	Material Constant
A''	[s <sup>-1</sup> ]	Material Constant
$\rho$	[m <sup>-1</sup> ]	Dislocation Density
A	[1/mm <sup>2</sup> ]	Material Constant
$\Theta$	[MPa]	Work Hardening Rate
R	[J/mol.K]	Gas Constant
T	[K]	Temperature
$t_{0.5}$	[s]	Time at 50% of Recrystallization
$d_{gg}$	[ $\mu\text{m}$ ]	Final grain growth
Z	[s <sup>-1</sup> ]	Zenner- Hollomon Parameter
X	[-]	Recrystallized Fraction
$\sigma_{WH}$	[MPa]	Work Hardening Stress
$\sigma_{sat}$	[MPa]	Saturation Stress
$\sigma_p$	[MPa]	Peak Stress
$\sigma_c$	[MPa]	Critical Stress
$\sigma_{ss}$	[MPa]	Steady-State Stress
h	[m <sup>-2</sup> ]	Mean Free Path of the Dislocations
r	[MPa]	Dynamic Recovery Coefficient
$\mu$	[GPa]	Shear Modulus
b	[nm]	Magnitude of Burgers Vector
q	[-]	Numerical Exponent
v	[-]	Numerical Exponent

$\tau$	[-]	Avrami Exponent
$b$	[-]	Avrami Coefficient
$k_0, k_1, k_2$	[-]	Material Constants

### ARTICLE #3

$\varepsilon$	[mm/mm]	Strain
$\varepsilon_c$	[mm/mm]	Critical Strain
$\varepsilon_p$	[mm/mm]	Peak Strain
$\dot{\varepsilon}$	[s <sup>-1</sup> ]	Strain rate
$\bar{\varepsilon}_{0.5}$	[-]	Strain at 50% of Recrystallization
$Q_{gg}$	[J/mol.K]	Activation Energy of Grain Growth
$d_0$	[ $\mu\text{m}$ ]	Initial Grain Size Diameter
$t$	[s]	Time
$d$	[ $\mu\text{m}$ ]	Grain Size Diameter
$n$	[-]	Material Constant
$m$	[-]	Grain Growth Exponent
$\alpha$	[MPa <sup>-1</sup> ]	Material parameter of Peak Stress
$A$	[1/mm <sup>2</sup> ]	Material Constant
$\theta$	[MPa)	Work Hardening Rate
$R$	[J/mol.K]	Gas Constant
$T$	[K]	Temperature
$t_{0.5}$	[s]	Time at 50% of Recrystallization
$d_{gg}$	[ $\mu\text{m}$ ]	Final grain growth
$d_f$	[ $\mu\text{m}$ ]	Post-Recrystallization Grain Growth
$Z$	[s <sup>-1</sup> ]	Zenner- Hollomon Parameter
$X$	[-]	Recrystallized Fraction
$\sigma_{WH}$	[MPa]	Work Hardening Stress
$\sigma_{sat}$	[MPa]	Saturation Stress

$\sigma_p$	[MPa]	Peak Stress
$\sigma_c$	[MPa]	Critical Stress
$\sigma_{ss}$	[MPa]	Steady-State Stress
$Q_1$ to $Q_9$	[J/mol.K]	Numerical Activation Energy
$r$	[MPa]	Dynamic Recovery Coefficient
$Q_{Total}$	[J/mol.K]	Total Activation Energy From Flow Curves
$a_1$ to $a_{10}$	[-]	Numerical Dependent Material Parameter
$m_1$ to $m_8$	[-]	Strain Rate Dependent Material Parameter
$n_1$ to $n_8$	[-]	Strain Dependent Material Parameter
$k_d, k_m, k_s$	[-]	Avrami Exponent
$\beta_d, \beta_m, \beta_s$	[-]	Avrami Coefficient

# CAPÍTULO 1 - INTRODUÇÃO

## 1. Introdução

Na indústria, o forjamento a quente é um dos principais processos de fabricação devido a sua flexibilidade e diversidade para a produção de geometrias complexas com alta produtividade. Este processo é presente, em grande parte, nos setores automotivo, aeroespacial e naval, podendo-se citar como alguns exemplos a fabricação de engrenagens, virabrequins, grandes eixos rotores e componentes estruturais.

A maneira convencional de forjar materiais metálicos, para que não haja o emprego de grandes tensões, é o aquecimento até temperaturas adequadas, no forjamento a quente, acima da temperatura de recristalização do material. Após a sua forja, convencionalmente, os aços passam por tratamentos térmicos e termoquímicos que exigem reaquescimentos do material, fazendo com que se aumente o custo de produção do componente. Desta forma, impactando negativamente no ciclo de produção sustentável e na emissão de gases de efeito estufa. Hoje o processo produtivo deve envolver ao máximo o uso das chamadas “*Green Manufacturing Technologies*” (tecnologias aplicadas a manufatura verde), o que exige um conhecimento e domínio profundo do processamento termomecânico a fim de reduzir-se o número de etapas de fabricação e o consumo energético nestas etapas, por exemplo.

A necessidade em melhorar a eficiência energética na fabricação motivou o desenvolvimento do projeto de pesquisa intitulado “*Manufatura energeticamente eficiente para aços bainíticos avançados baseado no processamento termomecânico*” junto ao programa de cooperação internacional BRAGECRIM (*Brazilian-German Collaborative Research Initiative on Manufacturing Technology*) realizado em parceria entre o Laboratório de Transformação Mecânica (LdTM-UFRGS) e o Instituto de Tecnologia em Materiais (IWT- UB Bremen, Alemanha), coordenado no Brasil pelo Prof. Dr. Alexandre da Silva Rocha, fomentado pela CAPES (Auxílio 1844/2017) e DFG EP 128/6-2. Diversos trabalhos acadêmicos como dissertações de mestrado, teses de doutorado e artigos científicos no tema processamento termomecânicos de aços bainíticos e manufatura energeticamente eficiente foram realizados. O projeto de pesquisa visou o desenvolvimento de uma nova cadeia de processamento sustentável no forjamento a quente e

engenharia de superfícies com a redução no consumo energético causado por tratamentos térmicos subsequentes como têmpera e revenido (T & R), conforme demonstram algumas referências (DALCIN et al., 2022; TURRA, et al., 2021; HATWIG et al., 2021; BELIVAQUA et al., 2021; CASTRO, et al., 2021; DONG, et al., 2020; MENEZES, 2021; SILVEIRA, et al., 2020). A presente tese faz parte deste contexto de pesquisa em desenvolvimento.

Nos últimos anos, o desenvolvimento de aços de microestrutura bainítica livre de carbonetos focam em aplicações que demandam alta resistência mecânica e boa tenacidade. Na formação dos aços bainíticos, em comparação aos aços ferrítico-perlíticos, a quantidade estequiométrica dos elementos de liga, como o Silício (Si), é maior, evitando a formação de carbonetos de ferro (cementita) nos contornos de grão (SOURMAIL, 2017; BHADSHIA, 2019). Permite a formação de uma microestrutura com diferentes morfologias, em aspectos granulares e em ripas. A combinação de subunidades refinadas e dos filmes de austenita fazem aumentar substancialmente a resistência mecânica, bem como a ductilidade (HOFER et al., 2015). Portanto, desenvolver produtos forjados com a microestrutura bainítica em resfriamento contínuo é atrativo para a indústria, principalmente pela demanda em eficiência energética, pois se pode adquirir alta performance dos componentes, sem a utilização de processos subsequentes de tratamentos térmicos que envolvem temperaturas elevadas e longos tempos com consequente elevado consumo energético.

Estudos recentes confirmam que o refino no tamanho de grão austenítico acelera a reação bainítica devido ao aumento de sítios de nucleação. Assim, facilitando a taxa de crescimento dos feixes da bainita devido a maior área de contornos de grão por unidade de volume (HAN et. al., 2017; HU et. al., 2014; XU et. al., 2017). É mostrado também que, o refino do grão em transformações adifusionais, como o da martensita, reduz o tamanho de seus pacotes, bem como o comprimento dos blocos, porém a largura não modifica, como consequência, aumenta a sua resistência a tração e ductilidade (HANAMURA et al., 2013). Portanto, o controle do grão austenítico prévio é uma importante etapa pois a variação do seu diâmetro levará a efeitos significativos no desempenho mecânico final.

Grãos recristalizados e refinados podem diminuir as temperaturas finais de transformação em resfriamento contínuo, o que significa uma transformação bainítica no campo martensítico dentro da curva CCT (PEROZZO, 2019). Essa afirmação corrobora com a formação de um

constituente terciário chamado de M/A, que é uma fração de austenita e martensita (HOFER et al., 2015; SILVEIRA, 2019). A alta densidade de defeitos cristalinos é uma condição natural da M/A, que se demonstra mais favorável ao crescimento na austenita deformada em ligas com baixos teores de carbono. Por exemplo, a redução da temperatura do processamento termomecânico pode causar o aumento na densidade de constituintes M/A, aumentando a dureza da microestrutura bainítica (BEVILAQUA, 2021). A M/A apresenta uma ampla variação de tamanho e morfologia, e cada variação afeta as suas propriedades mecânicas, sendo assim, o controle do tamanho de grão é fundamental para tais transformações (LI, B. et al., 2019; RAMACHANDRAN et al., 2020; TAKAYAMA; MIYAMOTO; FURUHARA, 2018).

Nesta tese, a principal motivação para o uso da simulação numérica está em buscar soluções em respeito às dificuldades em medir ou instrumentar processos termomecânicos industriais. Dessa forma, é possível reduzir consideravelmente as tentativas e erros de processos, bem como a quantidade de experimentos necessários para a determinação de parâmetros em uma condição crítica de trabalho.

Uma maneira de melhorar a aproximação com os processos reais de fabricação por forjamento a quente é combinar a mecânica da plasticidade com os fenômenos metalúrgicos pelo método de elementos finitos (MEF). Portanto, prever matematicamente os fenômenos de recristalização e crescimento de grão em processos de forjamento a quente é fundamental quando se visa o controle do grão em processos industriais. Em casos específicos, essa modelagem computacional pode ser útil na previsão microestrutural a fim de se obter propriedades desejadas.

Pode-se dividir em duas categorias os tipos de modelos microestruturais: os modelos físicos avançados baseados na matemática e os modelos fenomenológicos (HALBERG, 2011). Os modelos físicos avançados ou em meso-escala são empregados em estudos a respeito da Plasticidade em Cristais (*Crystal Plasticity*), Autômato Celular e abordagem em Campo Médio (BLESGEN, 2016; CHEN, et. al., 2019; ZOUARI, et. al., 2016). Esses propiciam modelos matemáticos que levam em consideração todos os aspectos da evolução microestrutural do material durante o processamento em uma escala microscópica. Porém, são modelos que envolvem elevado custo computacional, necessitam de computadores com uma elevada capacidade de processamento, e que, portanto, ainda fogem das práticas industriais.

Já os modelos fenomenológicos ou macro-escala são matematicamente estáveis e mais acessíveis devido a sua simplicidade e abrangem uma escala maior de predição, por exemplo, na aplicação de processos de forjamento como abordados por (HIRT, SCHÄFER, 2010 ; COLOMBO, BRITO, SCHAEFFER, 2014). Além disso, os custos computacionais exigidos para a realização dos cálculos são em ordem de magnitude menores, em comparação aos modelos em meso-escala, porém envolvem muitas suposições, que levam a diminuição da acurácia em comparação aos modelos físicos.

Um dos principais problemas da diminuição da acurácia dos modelos fenomenológicos é a inadequada calibração experimental, onde não é trivial encontrar um padrão na literatura que nos guie de maneira adequada para a predição no tamanho de grão recristalizado (BYLYA, et. al., 2017). Normalmente, a estrutura matemática desses modelos é baseada em curvas de tensão deformação geradas por simuladores físicos em laboratórios, limitadas a um determinado grau de deformação, taxa de deformação e temperatura.

No entanto, as condições reais de forjamento em matriz fechada, por exemplo, são mais complexas devido aos gradientes térmicos locais que são dependentes de sua geometria e as elevadas taxas de deformação envolvidas. A desconsideração da sinergia entre os parâmetros como o alto grau de deformação, taxas de deformação e temperatura, levam a imprecisões. Mesmo assim, os modelos fenomenológicos ainda são promissores em termos de predição microestrutural pelo fato de se obter o controle em peças em maiores dimensões.

Ainda há dificuldades em encontrar métodos simples e de baixo custo operacional e computacional para a caracterização e a aquisição de coeficientes que descrevem empiricamente a recristalização e crescimento de grão em novos materiais forjáveis. Estes são necessários para implementação em simulação computacional de processos industriais. Portanto, neste trabalho realizou-se uma abordagem metodológica para a calibração de simulações computacionais, visando a observação dos fenômenos reológicos e microestruturais. Para isso, fez-se experimentos para aquisição de dados necessários para a obtenção dos parâmetros cinéticos de recristalização e crescimento de grão de um novo aço DIN 18MnCrSiMo6-4. O modelo matemático de JMAK (*Jhonson –Mehl – Avrami- Kolmogorov*) foi utilizado para a previsão da cinética de recristalização e de crescimento de grão (KOLMOGOROV, 1937; JHONSON, MEHL, 1939; AVRAMI, 1939). Por meios analíticos e de regressões não lineares, fez-se a verificação e a validação de modelos

numéricos de forjamento a quente, onde comparou-se os resultados obtidos por experimentos industriais de forjamento a quente. Pode-se observar que os resultados foram satisfatórios e que a simulação permitiu mapear o comportamento termomecânico e metalúrgico dos aços DIN 20MnCr5 e DIN 18MnCrSiMo6-4 aqui estudados.

## 1.1 Objetivos

### 1.1.1 Objetivo geral

O objetivo geral desta tese foi modelar, prever e comparar diferentes parâmetros de forjamento a quente em um novo aço bainítico avançado DIN 18MnCrSiMo6-4, tendo-se como resposta o tamanho de grão austenítico e as propriedades mecânicas do material pós-processamento.

### 1.1.2 Objetivos Específicos

- Modelar numericamente o processo de forjamento a quente pelo método de elementos finitos MEF. Propor um método de calibração feito por diferentes experimentos e validá-lo em processos de forjamento e simulação física.
- Com base nos conceitos de encruamento, recuperação *DRV*, recristalização *DRX* e crescimento de grão *CG*, validar o modelo semiempírico probabilístico de (*Jhonson-Mehl-Avrami-Kolmogorov* JMAK) do aço DIN 18MnCrSiMo6-4.
- Modelar matematicamente as curvas de escoamento para implementação em software comercial de elementos finitos e implementar o modelo de microestrutura do aço bainítico avançado DIN 18MnCrSiMo6-4.
- Comparar as simulações com os resultados obtidos experimentalmente do forjamento em matriz fechada com os modelos fenomenológicos propostos para o novo aço bainítico, desta forma validando o modelo em escala industrial.
- Comparar as propriedades mecânicas dos forjados na indústria em diferentes condições de processo afim de se obter os melhores parâmetros, baseando-se na relação resistência e ductilidade.

## CAPÍTULO 2 – INTEGRAÇÃO DOS ARTIGOS CIENTÍFICOS

Na presente tese, uma metodologia foi desenvolvida para a calibração e a obtenção de parâmetros fundamentais para modelar matematicamente a microestrutura de um novo aço bainítico em um forjamento controlado. O cerne deste trabalho foi o entendimento e o controle do tamanho de grão austenítico durante o forjamento a quente em escala industrial, visando uma determinada microestrutura bainítica com melhores propriedades mecânicas em função da temperatura de processamento.

Os trabalhos realizados durante esta tese foram desenvolvidos no Laboratório de Transformação Mecânica (LdTM- UFRGS), IBF- RWTH- Aachen e IWT- Bremen. Os testes industriais de forjamento foram realizados em uma fabricante de engrenagens, indústria INPEL S.A, em Sapucaia do Sul-RS. Como resultado da pesquisa, foram realizadas diversas publicações, dentre as quais se destacam 3 artigos de autoria principal do presente autor desta tese, que foram selecionados para compor este trabalho e são referenciados (IVANISKI, et. al., 2019; IVANISKI, et. al., 2020; IVANISKI, et. al., 2022).

### **2.1 Viabilização do modelo em macro escala no controle do tamanho de grão austenítico em forjamento a quente**

O primeiro artigo publicado na *Materials Research* Volume 22, N° 5, 2019, intitulado “*Austenitic grain size prediction in hot forging of a 20mncr5 steel by numerical simulation using the JMAK model for industrial applications*” viabilizou a metodologia de caracterização e validação do modelo numérico computacional de tamanho de grão austenítico, utilizando o modelo de JMAK para o aço ferrítico-perlítico DIN 20MnCr5. A sinergia entre as variáveis dos processos de forjamento a quente como atrito, tensões, deformações e taxas de deformação e a resposta na evolução de tamanho de grão foram interpretadas. Permitindo, dessa forma, entender os principais efeitos causados pelo forjamento a quente frente a recristalização dinâmica  $X_{DRX}$ , metadinâmica  $M_{DRX}$  e estática  $S_{RX}$  na distribuição do tamanho grão no final do processo.

A calibração frente ao modelo computacional foi razoavelmente precisa, de maneira que todas as interpretações descritas numericamente e empiricamente fossem usadas como base na aplicação deste modelo em macro escala para o novo aço bainítico avançado. Porém, curvas de

escoamento plástico da simulação não apresentam um comportamento real na cinética de recristalização dinâmica e do seu regime estacionário, por mais que a calibração do recalque cilíndrico seja uma boa metodologia para uma aproximação experimental. As curvas de Hensel-Spittel, disponíveis do banco de dados do software FORGE®, não representam a recuperação dinâmica DRV do processo.

## **2.2 Constituição dos modelos matemáticos para as curvas de escoamento do aço bainítico DIN 18MnCrSiMo6-4 e os modelos de recristalização**

Devido à falta de informações sobre o comportamento plástico do aço DIN 18MnCrSiMo6-4, foi necessário um estudo reológico do material. Portanto, na segunda publicação científica intitulada, “*Constitutive Modelling of High Temperature Flow Behaviour for a Low Carbon High Silicon Bainitic Steel*” *Materials Research* Volume 23, N° 5, 2020, foi delimitado as curvas de escoamento a quente do aço bainítico avançado DIN 18MnCrSiMo6-4, como também os coeficientes de encruamento, recuperação e recristalização dinâmica do material para diferentes condições de processamento. Isto permitiu constituir um modelo reológico com o uso das equações cinéticas de Arrhenius e de *JMAK*, e os parâmetros de recristalização dinâmica dependentes das curvas de escoamento. Portanto, se pode quantificar os efeitos causados pelo acúmulo de discordâncias, a aniquilação e o rearranjo e modelar a cinética de recristalização dinâmica, baseando-se nas curvas de tensão deformação.

No estudo, se pode comparar diferentes modelos matemáticos para a descrição do comportamento das curvas de escoamento em altas deformações plásticas, por meio de ensaios de compressão. O estado de tensões em compressão é comum em processos de forjamento a quente, como se pode observar nos resultados do primeiro artigo teórico-empírico.

## **2.3 Implementação e validação numérica computacional de um novo aço bainítico em processos industriais de forjamento**

Uma das demandas na indústria é entender os mecanismos de recristalização em diferentes campos de deformações e taxas de deformação, o que torna esta ciência menos trivial em processos de forjamento em matriz fechada. Pois, haverá diferentes interações geométricas e diferentes estados de tensões responsáveis por tal complexidade. Portanto, com base no conhecimento já

adquirido nas últimas décadas em respeito ao estudo de recristalização e crescimento de grão, o terceiro artigo “*Numerical and experimental study of an industrial case for grain size evolution in bainitic steel in controlled hot forging and its influence on mechanical performance*” *Materials Research*, Volume 23, N° 5, 2022 contribuiu:

- Nos efeitos da sinergia entre os campos de deformação, taxa de deformação e temperatura em uma peça forjada em matriz fechada e sua evolução microestrutural;

- Na calibração e validação no modelo de grão austenítico de um aço bainítico avançado em uma aplicação industrial, com base nos resultados adquiridos do segundo artigo utilizando o software comercial DEFORM® V.11.0.;

- Em mostrar o efeito que o expoente de crescimento de grão ( $m$ ) possui, devido ao gradiente de temperatura e no tamanho de grão final em processos não-isotérmicos de forjamento. Mostrando a importância de uma calibração correta na simulação do tamanho considerando o crescimento do grão austenítico recristalizado, que variam dependendo da distribuição de temperatura na peça e deformação residual;

- Em afirmar que o controle da temperatura de forjamento a quente com a base nos resultados do modelamento numérico do grão permitiu um aumento considerável na relação resistência e ductilidade do aço DIN 18MnCrSiMo6-4 devido ao refino de grão.

## **CAPÍTULO 3 – ARTIGOS PUBLICADOS**

**Austenitic grain size prediction in hot forging of a 20MnCr5 steel by numerical simulation using the JMAK model for industrial applications**

Artigo publicado no periódico Materials Research, Volume 22, N° 5, 2019. Páginas. 1-7.

### 3.1 Austenitic grain size prediction in hot forging of a 20MnCr5 steel by numerical simulation using the JMAK model for industrial applications

Thiago Marques Ivaniski <sup>1</sup>, Jérémy Epp <sup>2</sup>, Hans-Werner Zoch <sup>2</sup>, Alexandre da Silva Rocha <sup>1</sup>

<sup>1</sup> Metal Forming Laboratory - LdTM – PPGE3M - UFRS, Porto Alegre, RS, Brazil

<sup>2</sup>Leibniz-Institut für Werkstofforientierte Technologien – IWT, Bremen, Germany

e-mail: [thiago.ivaniski@ufrgs.br](mailto:thiago.ivaniski@ufrgs.br)

Yield strength and toughness in steels are directly associated with hot forging processes, especially by controlling austenitic grain size and cooling conditions. The phenomenological JMAK model in macroscale has been applied in different material classes to predict grain size after hot forming. However, on an industrial application, there is still a lack of understanding concerning the synergic effects of strain rate and temperature on recrystallization. This preliminary study aimed at investigating the applicability of coupled semi-empirical JMAK and visco-elastoplastic models in numerical simulation to predict austenitic grain size (PAGS). Hot forging of cylindrical samples of a ferritic-perlitic DIN 20MnCr5 steel was performed followed by water quenching. The main influences, such as temperature, strain and strain rate fields following the recrystallization model were investigated using the subroutine of FORGE NxT 2.1 software. The results were evaluated by comparing experimentally measured and simulated PAGS at process end. The forging process generates different strain and strain rate fields in the workpiece, which in turn lead to a variation in the PAGS and recrystallization fractions. The simulation was able to detect the PAGS variation showing a good agreement between the experimental forging results and the applied model.

**Keywords:** Numerical Simulation, JMAK's model, Hot Forging, Grain Size.

#### 3.1.1 Introduction

Microstructure control is a key to the development of high-performance alloy steels, especially for applications requiring toughness, high fatigue strength, and hardness in automotive components. Several studies report the phenomena of hardening, dynamic recovery, dynamic recrystallization, and austenitic grain growth, and how these phenomena affect the steel mechanical properties. The control of such mechanisms by thermomechanical processing is most commonly implemented in rolling processes [1,4-6]. However, they are often more challenging to be implemented for forging processes. As an economically feasible alternative that has excellent potential for forging solutions, Finite Element Method (FEM) using computer simulation seeks to reduce the try-outs in an industrial scenario. Moreover, the classic JMAK model (Johnson-Mehl-Avrami-Kolmogorov) is mathematically stable and can be applied to predict recrystallization and grain growth phenomena [7]. The JMAK model is presently available in several numerical simulation software. For more than a decade it has been shown that the semi-empirical analytical

model JMAK can describe the global recrystallization kinetics (Eq. 3.1.1), where  $X(t)$  represents the recrystallized grain fraction as a function of time ( $t$ ).

$$X(t) = 1 - e^{-b \cdot t^n} \quad (3.1.1)$$

The exponent ( $b$ ) represents the Avrami coefficient, therefore very sensitive to variation in temperature. The Avrami exponent ( $n$ ) is related to the mechanism of phase transformation, for example, if the nucleation rate remains constant or even increases during the transformation progress or if the nucleation rate reaches zero soon after the onset of growth.

Many articles report the strong influence of parameters such as temperature, deformation and strain rate on dynamic ( $X_{DRX}$ ), metadynamic ( $M_{DRX}$ ) and static ( $S_{RX}$ ) recrystallization [8-10]. Innovative studies have considered the quantitative dependence of XDRX activation energy and strain rate exponent on the temperature variation in high carbon steels. They also were successful in minimizing errors between the experimental values and correspondent finite element solutions using optimization tools [11-13]. However, there are some implications concerning the validation of a robust model for hot forging processes that should be considered, such as thermomechanical history, complex strain fields, fibering zones as well as steady-state conditions in flow curves. These influences are not isolated in forged parts and are driven by industrial demands. Therefore, more efforts must be given to reach more accurate results by FEM simulation models in industrial forging applications.

This preliminary study aimed at investigating the applicability of a semi-empirical model of JMAK coupled to the visco-elastoplastic model in numerical simulation. A ferritic-perlitic DIN 20MnCr5 steel microstructural was used to carry out this work. Subsequent steps of the process were performed to represent an industrial process. The main influences, such as temperature, strain and strain rate fields following the recrystallization model were investigated using a subroutine of the FORGE NxT 2.1.

## 3.1.2 Materials and Methods

### 3.1.2.1 Acquiring the Experimental Data

Cylindrical samples with a diameter of 25.4 mm and a height of 35 mm were manufactured from a DIN 20MnCr5 steel. The chemical composition of the steel is shown in [Table 3.1.1](#). Hot forging (upsetting) experiments were carried out in a hydraulic press with a capacity of 400 kN, as shown schematically in [Figure 3.1.1](#).

**Table 3.1.1.** Chemical composition of the experimental DIN 20MnCr5.

% wt	C	Si	Mn	Cr
	0.19	0.2	1.25	1.15

Samples were heated in the furnace to 1200 °C and then moved to the press where a 60% reduction in height was applied. The temperature evolution in the workpiece was measured by a thermal imager Fluke® Ti400. The temperature frames obtained by the thermal imager were corrected by thermocouple analysis for higher accuracy in the temperature determination. After that, the collected results were used as boundary conditions into the Forge® software. The austenitic grain size was analysed by Optical Microscopy following the ASTM E112 standard. The forged samples were quenched in water directly after forging to stop changes in grain size, in order to preserve the austenitic grain size from deformation end. Samples were etched to reveal the prior austenite grain boundaries (PAGBs) with an etching prepared with 3g of picric acid in a solution of 30% liquid detergent in water.

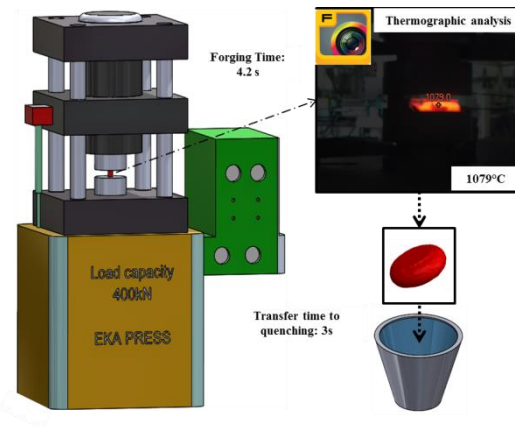


**Figure 3.1.1.** Conceptual scheme of experiments.

### 3.1.2.2 Boundary Conditions for Simulation

Finite Element Method was carried out using tetrahedral (deformable) mesh with volumetric elements for the billet and triangular (rigid) surface elements for the dies, as illustrated in [Figure 3.1.2](#). The average mesh size was enough refinement for high convergence in the calculations.

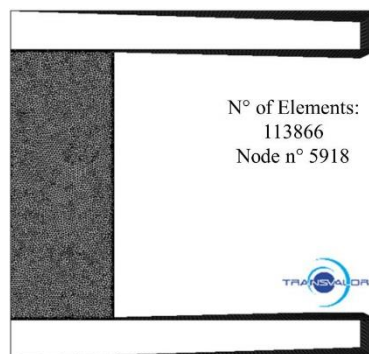


**Figure 3.1.2.** Modelling proposed.

[Table 3.1.2](#) shows the boundary conditions used for modelling, including friction and thermal parameters. The forming velocity of the hydraulic press was calculated from displacement data acquired during forming by an LVDT (Linear Variable Displacement Transducer) coupled to the upper die and with the end in contact with the lower (stationary) die. Regarding the friction

between the systems, the best fitting condition of no lubrication was chosen from the software database.

**Table 3.1.2.** Boundary conditions used in the numerical computational simulation from the data collected in experiments.

PARAMETERS	VALUE
Initial steel temperature (°C)	1180
Environment temperature (°C)	50
Dies temperature (°C)	190 Upper /250 Lower
Tool velocity (mm/s)	5
Heat transfer coefficient with pressure (dies) (W/m <sup>2</sup> .K)	500
Heat transfer ambient media (W/m <sup>2</sup> .K)	10
Friction coefficient (Coulomb) ( $\bar{m}$ and $\mu$ )	0.8 and 0.4

### 3.1.2.3 Recrystallization Modelling

The recrystallization kinetics and austenitic grain growth were based on the global JMAK model. The output results consisted of the percentage value of the recrystallized fraction, as demonstrated in Equation (1). This model is embedded into the commercial FEM metal forming software FORGE® software and can be seen in [Table 3.1.3](#), where all the constants necessary to predict the behaviour in the recrystallization of DIN 20MnCr5 steel are presented [14]. [Figure 3.1.3](#) shows a conceptual flowchart of the methodology used to perform the study and a comparison of the expected experimental results.

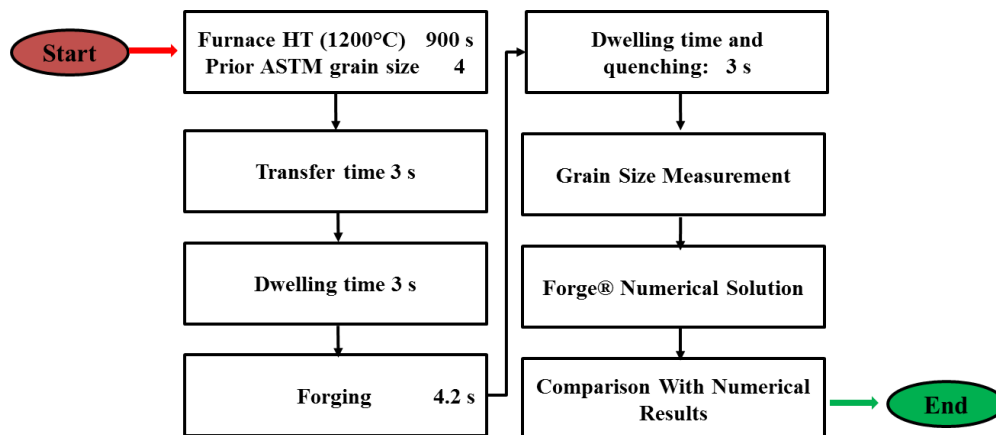


**Figure 3.1.3.** Conceptual flowchart used to compare experimental results and computational simulation.

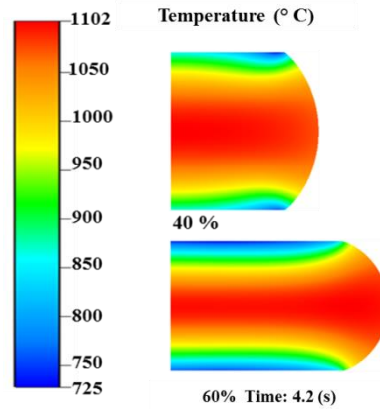
**Table 3.1.3.** Equations to describe the microstructure evolution.

PARAMETERS	EQUATION
<b>Recrystallization</b>	
Critical Strain	$\varphi_c = 3.92 \cdot 10^{-4} d_0^{0.5} \cdot Z^{0.15}$
<b>Kinect parameters</b>	
Zener-Hollomon	$Z = \dot{\varphi} \cdot e^{\left(\frac{310244}{RT}\right)}$
Dynamic recrystallization fraction, $D_{RX}$	$X_{DRX} = 1 - e^{(-0.693147 \cdot \left(\frac{\varphi - \varphi_c}{\varphi_{0.5} - \varphi_c}\right)^2)}$
50% recrystallization, $D_{RX}$	$\bar{\varphi}_{0.5} = 1.14 \cdot 10^{-3} \cdot d_0^{0.28} \cdot \dot{\varphi}^{0.05} \cdot Z \cdot e^{\left(\frac{53379}{RT}\right)}$
Static recrystallization fraction, $S_{RX}$	$X_{SRX} = 1 - e^{(-0.693147 \cdot \left(\frac{t}{t_{0.5}}\right))}$
Metadynamic recrystallization fraction, $M_{DRX}$	$X_{MDRX} = 1 - e^{(-0.693147 \cdot \left(\frac{t}{t_{0.5}}\right))}$
Time for 50% $M_{DRX}$ , $t_{0.5}$	$t_{0.5} = 1.06 \cdot 10^{-5} \cdot Z^{-0.6} \cdot e^{\left(\frac{300000}{RT}\right)}$
<b>Grain Coarsening</b>	
For $D_{DRX}$	$D_{DRX} = 2.26 \cdot 10^4 \cdot Z^{0.5}$
For $S_{RX}$	$D_{SRX} = 0.5 \cdot \bar{\varphi}^{-1} \cdot d_0^{0.67}$
For $M_{DRX}$	$M_{DRX} = 1.8 \cdot 10^4 \cdot Z^{0.5}$
Diameter for a full $M_{DRX}$	$t_{0.5} = 1800 \cdot Z^{-0.15}$
Grain growth	$d_{gg}^{4.74} - d_0^{4.74} = 1.41 \cdot 10^{23} \cdot e^{\left(\frac{-433500}{RT}\right)} \cdot t$

In [Table 3.1.3](#), critical strain ( $\varphi_c$ ) is the minimum strain required for the dynamic recrystallization. The Zener – Hollomon parameter ( $Z$ ) is a function of the strain rate as well as the material activation energy ( $Q_{DRX}$ ) associated with recrystallization occurrence. This parameter is important because it establishes relationships between grain size and strain rate in the steel. The other kinetic parameters are related to recrystallization of DIN 20MnCr5 steel [14]. The  $t_{0.5}$  is the time for  $M_{DRX}$  equal to 0.5. The  $d_0$  represents the initial grain growth and  $d_{gg}$  the final grain growth for full recrystallization.

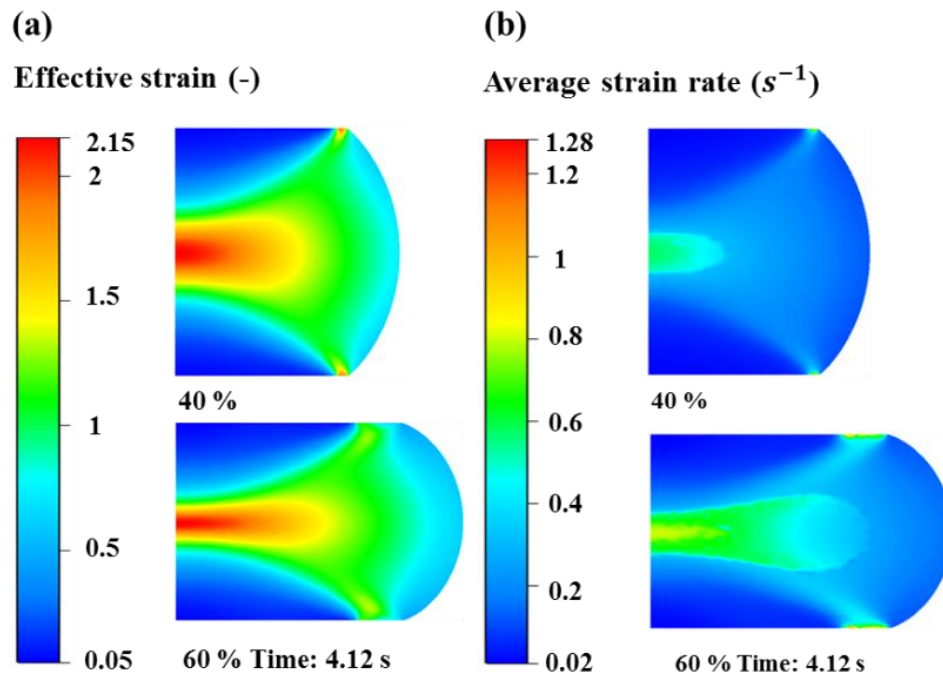
### 3.1.3 Results and Discussion

[Figure 3.1.4](#) illustrates the temperature fields in the samples after forming for two different height reductions, 40 and 60%. A considerable decrease of temperature is seen in the upper and lower surfaces, which are in contact with the dies due to thermal exchange.



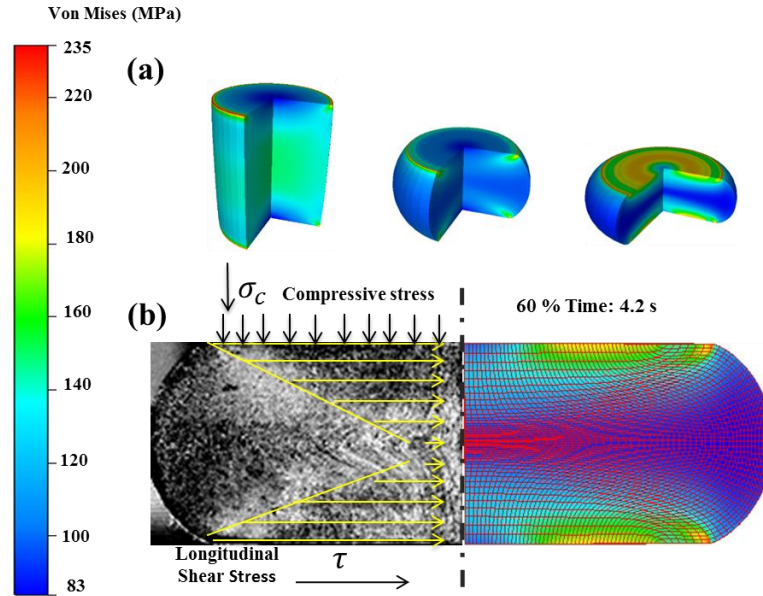
**Figure 3.1.4.** Numerical results of temperature fields after 40% and 60% height reduction.

Figure 3.1.5 (a) and (b) show the effective strain and strain rate, respectively. An ample variation of the plastic strain field was observed from the centre of the workpiece, as well as the barrelling of the samples due to the frictional forces in the sample/die interfaces. The average strain rate increases in the sample corner regions due to the high friction. The sample/die contact increases the heat transfer in the interface, leading to lower temperatures for samples faces than in the middle.



**Figure 3.1.5.** Numerical results of (a) Effective strain, (b) Average Strain rate.

Figure 3.1.6 (a) and (b) show, respectively, the Von Mises stress distribution and the fibering zone of the material as affected by shear stresses. After 60% of height reduction, higher local stresses are seen in the billet corners, which leads to an increase of strain rate and a decrease of the effective stress in the middle. The shear stress component increases gradually from the sample centre to the corner.



**Figure 3.1.6.** (a) Von Mises stress field, (b) Fibering and effect of stress triaxiality.

It is clear that the time evolution and distribution of stresses in the workpiece interact with strain rate and temperature, thus affecting recrystallization kinetics and finally the resulting austenitic grain size. Therefore, the temperature variation and the strain rate in the corners of the workpiece should be considered. This is an important issue to obtain a better agreement between the experimental process and simulation. Taking into account these considerations, forging parameters can be improved with the aid of FEM simulation.

Figure 3.1.7 (a) shows the dynamic recrystallization behaviour at 40% and 60% height reduction. In the centre of the sample with 60% reduction, a smaller recrystallized fraction is seen compared to other regions. According to Luton and Sellars [15], the reason for this could be that at lower strain rates and higher temperatures, distinct recrystallization cycles at a higher plastic strain are provoked. Furthermore, it could be associated with the shear stress gradient seen in the

fibering zones (Figure 3.1.6 (b)). The evolution of parameter ( $Z$ ), which depends on the strain rate, is presented in Figure 3.1.7 (b). There was a considerable increase in the Zener parameter, precisely in the corners of the workpiece, showing the proportionality of the shear stress and the increase of the strain rate. Sakai and Jonas [16] have already established relationships between the initial grain size and the parameter ( $Z$ ), demonstrating that at higher strain rates, smaller nucleated grain sizes are reached. When the strain rate increases, hardening is increased, this consequently decreases the effect of dynamic recrystallization and recovery. Thus, the accumulated energy due to the increase of the dislocation density after the forging unloads provided the necessary driving force for the metadynamic recrystallization [17]. Different values of ( $Z$ ) were found during the plastic deformation, which resulted in substantial grain size variations in the sample at the end of the process.

In laboratory experiments with constant temperature, it is possible to correlate the amount of stored energy with the dislocation density to grain refining [18]. However, in an industrial environment using low-speed hydraulic presses, one must take into account the temperature distribution in the component, and how this also affects the strain rate and nucleation of new grains. In this way, heterogeneous strain distribution occurs in the workpiece, not only by triaxiality, which directly affects the austenitic grain size, as well as by different strain rates and temperature.

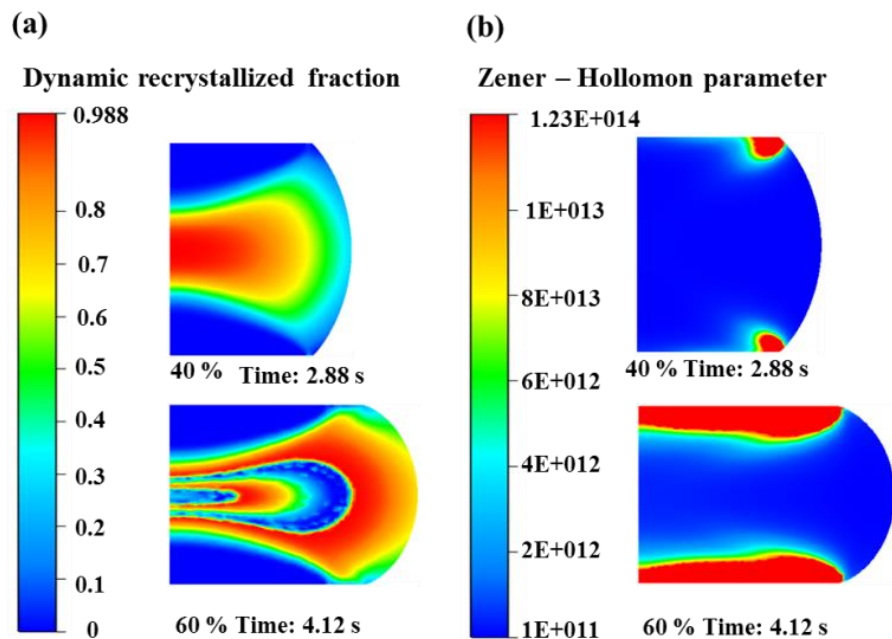


**Figure 3.1.7.** Numerical results of (a) Dynamically recrystallized fraction ( $X_{DRX}$ ), (b) Zener-Hollomon parameter.

Figure 3.1.8 (a) displays the simulation results of austenitic grain size after 60% height reduction, at the final time of forging, while Figure 3.1.8 (b) shows the results after simulated water quenching. It is possible to observe that there is a significant increase in the grains after forging ending (unload) and 35 seconds after the water quenching process. The differences in grain size are due to the mechanisms of meta-dynamic recrystallization included in the FEM calculation.

Figure 3.1.9 (a) illustrates the calculated meta-dynamic and static recrystallization in the final stage. The temperature field at steady-state (after 35 seconds in water) resulted in a higher fraction of metadynamic recrystallized grains in the regions with lower strain, strain rate and temperatures. According to Hodgson [19], metadynamic recrystallization depends on the strain rate, being little influenced by temperature and alloying elements. However, the Zener parameter, which means the temperature corrected strain rate [16], was sensitive to forging temperature. Therefore, the temperature gradients must be taken into account during forming, for example, in the corners of the workpiece, where the ( $Z$ ) value is larger and more refined grains were seen.

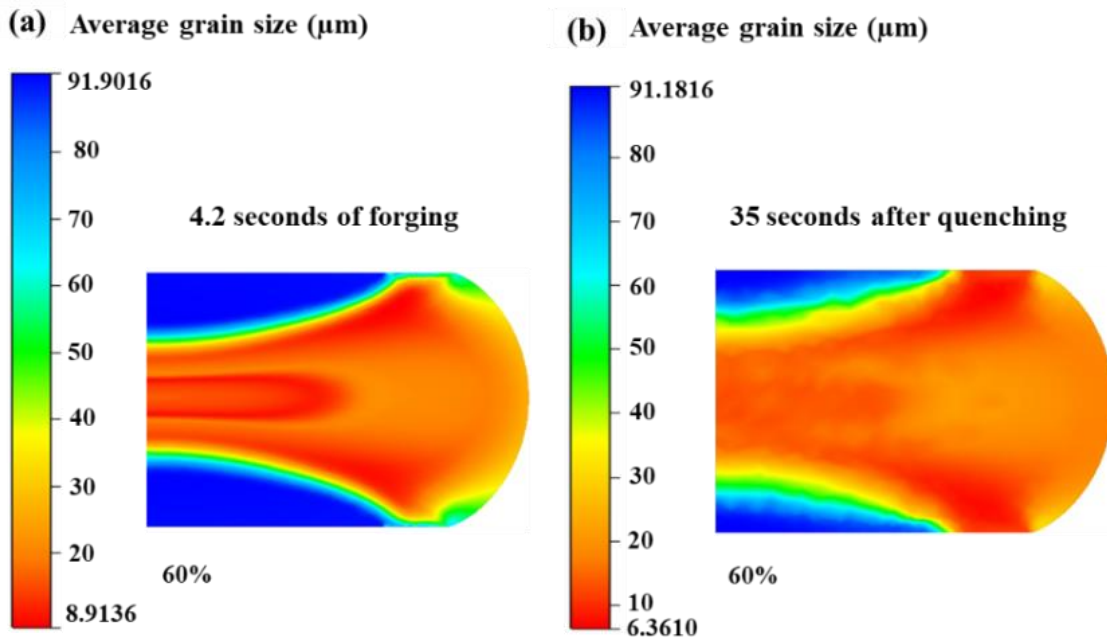
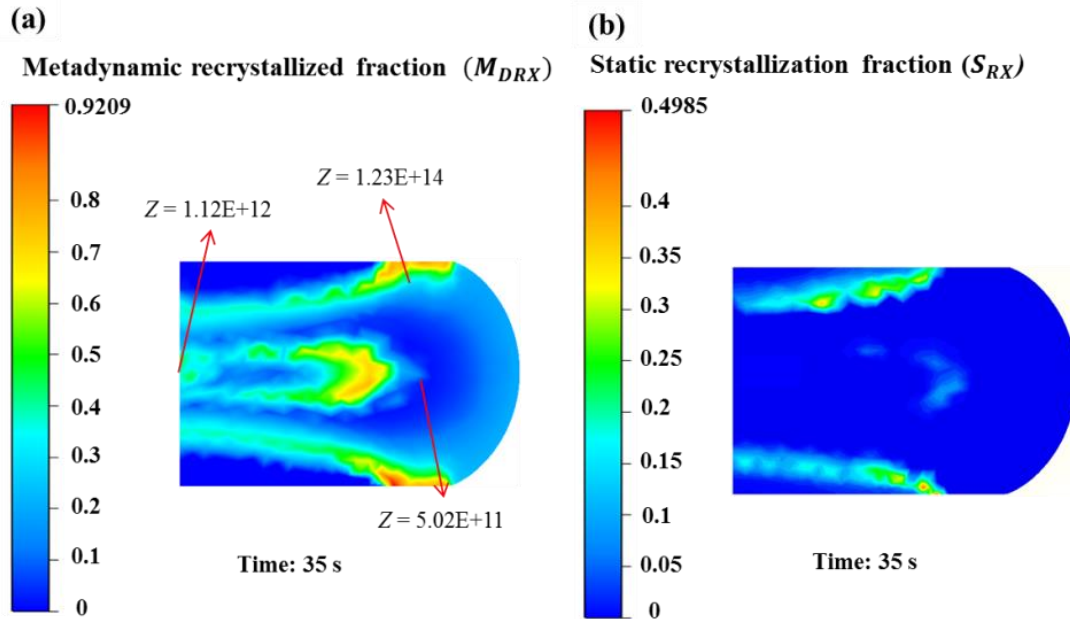


Figure 3.1.8. Numerical results of (a) Average grain size in the forging instant, (b) Average grain size after quenching.



**Figure 3.1.9.** (a) Metadynamic recrystallized fraction ( $M_{DRX}$ ), (b) Static recrystallized fraction ( $S_{RX}$ ).

Figure 3.1.10 presents the results obtained from the experimental austenitic grain size in four different selected region (R1, R2, R3 and R4). The analysis of the microstructure shows an apparent variation of grain size, as predicted by numerical simulation, however different grain morphologies could be seen which represent different recrystallization mechanisms. Therefore, the temperature and strain rate variation corrected by Z parameter should be considered in this case. In R1, there was no dynamic recrystallization ( $\varphi_c < \bar{\varphi}$ ), therefore sheared and polygonal grain characteristics which could represent a static recrystallized fraction mechanism. Figure 3.1.9 (b) shows the calculated results for the same region R1. In the region R2 a metadynamic recrystallization, as well as a geometric coalescence of the grains, was observed. This is attributed to the more significant thermodynamic potential at this point. It was also observed in the experimental analysis that in the region R3 higher grain refining was found ( $20 \mu\text{m}$ ), on the other hand for region R4 larger grain sizes ( $30 \mu\text{m}$ ) were measured when compared to R2 and R3. Those results confirm the difference of the Z parameter in both cases is related to the temperature variation, being lower in the middle of the workpiece.

Numerical simulated stress-strain curves for the forging process are shown in Figure 3.1.11(a), which presents several oscillations which are typical for dynamic recrystallization. The

decrease in stress after each plateau may be attributed to the new  $X_{DRX}$  cycle [20]. Figure 3.1.11 (b) shows the recrystallized fractions at each chosen region and the flow curve's response. It seems clear that an evident dynamic recrystallization cycle has occurred in R2 and R4. The reason for that is because there was both high temperature and considerable plastic strain, where new nucleated grains appear in the zone before full recrystallization ( $X_{DRX} > 0.95$ ). Therefore, the degree of plastic strain coupled with the strain rate and temperature individually influenced the cycles of dynamic recrystallization showing the time required to reach the steady-state during the deformation process, as a function of  $X_{DRX}$ . The  $X_{DRX}$  cycles in R2 is higher than R4 showing that the reduction of recrystallization rate decreases proportionally with the temperature, and can be confirmed in the R3 which presented the unfull recrystallization ( $X_{DRX} < 0.95$ ).

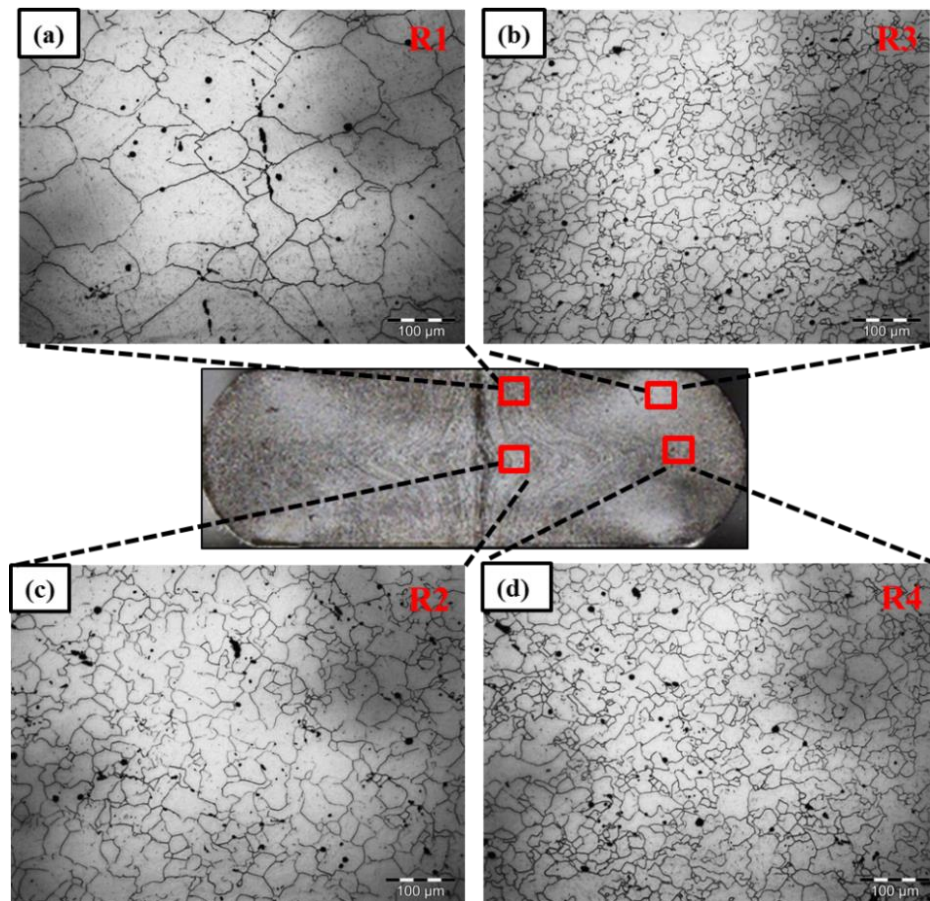


**Figure 3.1.10.** Experimental macrography and austenitic grain size results for forged and water quenched samples.

Picral etching with 3vol. % Picric Acid in destined water.

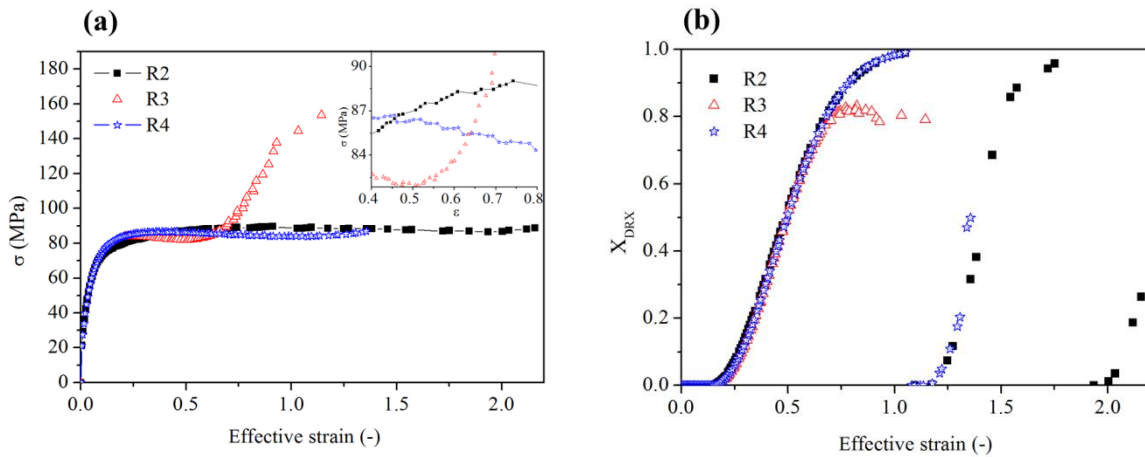


**Figure 3.1.11.** Numerical results of (a) Flow curves generated in different regions of the workpiece, (b)  $X_{DRX}$  cycles response.

Figure 3.1.12 compares measured and simulated grain sizes at four selected regions after the quenching process. The general behaviour and the dependencies with processing parameters were well described by simulation, however differences in the absolute values are seen. Possibly a significant factor influencing the simulation results is the heat transfer model for the water quenching, which shows the importance of controlling thermomechanical history. Besides that, considering a large number of possible impressions in the input data, as flow curves for different temperatures and strain rates, friction coefficient, heat transfer coefficients, among others contribute to the observed differences.

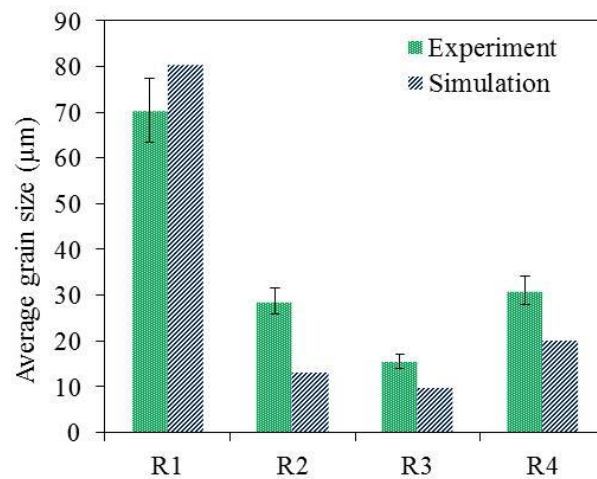


**Figure 3.1.12.** Average grain size comparison between experimental results and calculated.

### 3.1.4 Conclusions

This article showed the applicability of a model coupling the semi-empirical JMAK and a visco-elastoplastic model in numerical simulation of hot forging a 20MnCr5 steel followed by water quenching aiming at austenitic grain size prediction.

The results showed a good agreement between experimentally measured and simulated PAGS after hot forging and water quenching. Different distributions in austenitic grain size and recrystallized fractions were found in the forged part due to different strain-rate a temperature field, however, as demonstrated in this article the interaction of strain-rate and temperature plays an important role. The implemented models were able to detect those effects by showing the influences on the Zener-Hollomon parameter, which leads to PAGS non-homogenous distribution.

Finally, we can conclude that the numerical simulation using the already mentioned models is able to make a reasonable prediction of PAGS; however, there is still the need to improve boundary conditions with a precise determination of flow curves dependence on strain-rate and temperature.

### Acknowledgements

The authors thank the Brazilian agency CAPES (Project 1844/2017) and the German agency DFG (Project ZO140/21-1) for the financial support by means of the BRAGECRIM program (Brazilian German Cooperation Research in Manufacturing). Thiago Ivaniski also thanks CNPq (process number 167948/2017-2) for scholarship support.

### 3.1.8 References

- [1] Jorge Junior AM, Balancin O. “Prediction of steel flow stresses under hot working conditions”. *Materials Research*, v 8, n. 3, pp. 311-315, Jun-Jul. 2005.
- [2] Hanamura, Toshihiro et al. Effect of Austenite Grain Size on Transformation Behavior, Microstructure and Mechanical Properties of 0.1C–5Mn Martensitic Steel. *ISIJ International*, [s. l.], v. 53, n. 12, p. 2218–2225, 2013.

- [3] Sellars CM, Whiteman J A. “Recrystallization and grain growth in hot rolling”. *Metal Science*, v 13, pp. 187-194, April 1978.
- [4] Jorge AM, Regone W, Balancin O. “Effect of competing hardening and softening mechanisms on the flow stress curve modelling of ultra-low carbon steel at high temperatures”. *Journal Materials Process Technology*, v 142, n 2, pp. 415-421, Mar. 2003.
- [5] Lan L-Y, Qiu C-L, Zhao D-W, Gao X-H, Du L-X. “Dynamic and Static Recrystallization Behavior of Low Carbon High Niobium Microalloyed Steel”. *Journal Iron Steel Research International*. v 18, n 1, pp. 55-60, 2011.
- [6] Mirzadeh H., Najafizadeh A. “Prediction of the critical conditions for initiation of dynamic recrystallization”. *Materials and Design*. v 31, pp. 1174-179, set 2009.
- [7] Hallberg H. “Approaches to Modeling of Recrystallization”. *Metals (Basel)* [Internet]. 2011;1(1):16–48. Available from: <http://www.mdpi.com/2075-4701/1/1/16/>
- [8] Bylya, Olga et al. Applicability of JMAK-type model for predicting microstructural evolution in nickel-based superalloys. *Procedia Engineering*, [s. l.], v. 207, n. January, p. 1105–1110, 2017.
- [9] Stefani, N. et al. On the applicability of JMAK-type models in predicting IN718 microstructural evolution. *Computer Methods in Materials Science*, [s. l.], v. 17, n. 1, 2017.
- [10] Bylya, O. I. et al. Simulation of the material softening during hot metal forming. *Archives of Metallurgy and Materials*, [s. l.], v. 60, n. 3A, p. 1887–1893, 2015.
- [11] Moraes ALI, Balancin O. “Numerical Simulation of Hot Closed Die Forging of a Low Carbon Steel Coupled with Microstructure Evolution 2”. *Material Research*. , v 18, n. 1, pp. 92-97, Jun 2015.
- [12] Irani, Missam; Joun, Mansoo. Determination of JMAK dynamic recrystallization parameters through FEM optimization techniques. *Computational Materials Science*, [s. l.], v. 142, p. 178–184, 2018.
- [13] Irani M, et al. Experimental and numerical study on the temperature sensitivity of the dynamic recrystallization activation energy and strain rate exponent in the JMAK model. *J Mater Res Technol*. 2018. <https://doi.org/10.1016/j.jmrt.2018.11.007>
- [14] FORGE®. FORGE NxT V 2.1 System Documentation, Transvalor, Sophia Antipolis, Cedex, 2018.
- [15] Luton, M. J; Sellars, C.M. Dynamic recrystallization in nickel and nickel-iron alloys during high-temperature deformation. *Acta Metallurgica*, v. 17, p. 1033-1043, 1969.
- [16] Sakai, T.; Jonas, J. J., “Overview no. 35 dynamic recrystallization: mechanical and microstructural considerations”. *Acta Metallurgica*, v. 32, n. 2, p. 189-209, 1984.
- [17] Shen WF, Zhang C, Zhang LW, Xia YN, Xu YF, Shi XH. Metadynamic recrystallization of Nb-V micro-alloyed steel during hot deformation. *J Mater Res*. 2017;32(3):656–65.
- [18] Lin, Y. C., Chen, M-S, Zhong, J., “Numerical simulation for stress/strain distribution and microstructural evolution in 42CrMo steel during hot upsetting process”. *Computational Materials Science*, v. 43, n. 4, p. 1117-1122, 2008.
- [19] Hodgson, P. D.; Gibbs, R. K. A Mathematical Hot Rolled C-Mn Model to Predict and Microalloyed the Mechanical Properties of Steels. *ISIJ International*, [s. l.], v. 32, n. 12, p. 329–338, 1992.

[20] Mirzadeh, Hamed; Najafizadeh, Abbas. Hot Deformation and Dynamic Recrystallization of 17-4 PH Stainless Steel. *ISIJ International*, [s. l.], v. 53, n. 4, p. 680–689, 2013.

**Constitutive Modelling of High Temperature Flow Behaviour for a Low Carbon High Silicon Bainitic Steel**

Artigo publicado no periódico Materials Research, Volume 23, N° 5, 2020. Páginas. 1-10

## 3.2 Constitutive Modelling of High Temperature Flow Behaviour for a Low Carbon High Silicon Bainitic Steel

Thiago Marques Ivaniski <sup>1\*</sup>, Tomaz Fantin de Souza<sup>2</sup> Jérémy Épp <sup>3,4</sup>, Alexandre da Silva Rocha<sup>1</sup>

<sup>1</sup> Laboratório de Transformação Mecânica – Centro de Tecnologia –Departamento de Metalurgia – Universidade Federal do Rio Grande do Sul – Porto Alegre, RS, Brazil;

<sup>2</sup> Instituto Federal de Educação, Ciência e Tecnologia – IFSUL – Sapucaia do Sul, RS, Brazil;

<sup>3</sup> Leibniz-Institut für Werkstofforientierte Technologien – IWT, Bremen, Germany

<sup>4</sup> MAPEX Centre for Materials and Processes, University of Bremen, Germany

\* [thiago.ivaniski@ufrgs.br](mailto:thiago.ivaniski@ufrgs.br)

It is well recognized the importance of the rheological characterization for the development of the steel in thermomechanical treatments, especially for the mechanical properties' improvement of bainitic steels in subsequent hot forging optimization. Therefore, the plastic strain behaviour of a low carbon high silicon bainitic steel was studied through isothermal compression tests using a thermomechanical simulator at temperatures of 1123 K – 1423 K and strain rates of 0.1 – 5 s<sup>-1</sup>. Arrhenius equation was used to obtain the constitutive constants, which represents the material behaviour of flow stress in high temperature. Besides, work hardening, dynamic recovery, and the JMAK model in the dynamic recrystallization (DRX) of the steel parameters were determined. The second part of this research compared two proposed modified models from the literature, which showed the differences in modelled flow curves behaviour when they are applied for high strain levels. The flow curves were modelled in high strain levels for further implementation in numerical simulation, thus allowing an adjustment of parameters in hot forming processes for this bainitic steel. The proposed models presented an agreement with experimental values. However, only the Avrami equation to DRX showed the dynamic recovery mechanism in high strain levels, which has represented physical behaviour during the thermomechanical process.

**Keywords:** Flow Curves Modelling; Dynamic recovery and Dynamic recrystallization Kinetics; Bainitic Steels.

### 3.2.1 Introduction

Applications of advanced continuous cooling bainitic steels have received extensive attention in the past of decade due to their mechanical properties which can reach high levels of tensile strength and energy absorption. As a consequence, it has a considerable interest in industrial applications such as gears, crankshafts, side doors, railways and chassis [1,2,3].

There is a continuous challenge for discovering the best parameters to reach outstanding mechanical properties with lower energy consumption. For that reason, this shortcoming can be improved by microstructure optimization, avoiding subsequent heat treatments. Thereby, the

microstructure can be influenced by grain refining mechanisms, which brings different bainitic morphologies after continuous cooling [4].

Consequently, the determination of steel's flow curves is essential for proper identification of process windows and to guarantee good mechanical properties of the final products. They also provide data that will bring technical support to forging factories, which produce a large proportion of components in the automotive industry. Therefore, efforts concerning the hot-working conditions such as a dependence of flow stress with dynamic recovery (DRV), dynamic recrystallization (DRX) plays an essential role regarding the interactions of applied process parameters. Thus, the application Arrhenius-type model for flow curves and Johnson-Mehl-Avrami-Kolmogorov (JMAK) for recrystallization kinetics are indispensable. JMAK kinetics has a consolidated application in phase transformation of precipitation through nucleation and growth, which gives the content of a new phase as a function of time [5,6,7]. The global kinetics has been applied in the industrial field of hot forging steels because it represents a "semi-empirical" method, the numerical simulation results of the dynamically recrystallized volume fraction and austenitic grain size [8,9,10]. Besides, in terms of the flow curves, it can be used to model the softening mechanism during the plastic deformation in metallic materials [6,7].

In previous research, constitutive flow curves and microstructural models have been proposed for different bainitic steel grades, such as DIN 29MnSiCrAlNiMo, considered as a low carbon (0.3 wt.% C) bainitic steel [11]. Also, the flow curves and microstructure evolution by JMAK approach of DIN 70MnCrSiMo carbide-free bainitic steel, containing a higher carbon amount of 0.7 %C studied by Han, Y. et al [12]. They have reported as well in [13], the effect of temperature and strain rate on dynamic recrystallization of the 0.5 %C bainitic steel. It was developed accurately a kinetic model which reflects the dynamically recrystallized volume fraction ( $X_{DRX}$ ) changes.

A critical characteristic of the presented material which differs from the others studied bainitic steels, is the low carbon content, below 0.2 % C. Also, it is already known in recent reports that the continuous cooling of DIN 18MnCrSiMo6-4 bainitic steel has a suitable amount of silicon (>1.0%) used to avoid cementite precipitation which is replaced by stabilized austenite as the second constituent in bainite [4]. Thus, offering a considerable increase in yield strength and ductility. Moreover, the thermomechanical processing does not change the maximum attainable fraction of bainite, but clearly refines the microstructure after the austenite plastic deformation due to recrystallization mechanism [14]. However, there is still lacking information regarding different

hot working conditions, which is essential to obtain input data to Finite Element Models, including *DRX* microstructure evolution—in this way, optimizing the production of hot forged components.

In order to study how this material behaves in hot work conditions, this paper aim at obtaining flow curves in isothermal compression tests at different temperatures and strain rates.

Mathematical models were applied to obtain the constitutive constants of (*DRV*) and dynamic recrystallization (*DRX*). Moreover, two modified models presented by Xiao et al., 2011 [15], and Mirzadeh et al., 2010 [16], which include the Avrami-type equation, were used in this work. This equation has taken in to account the softening mechanism caused by the *DRX* in high-temperature plastic strain [17]. Both models were extrapolated for high plastic strain levels and compared with the experimental results.

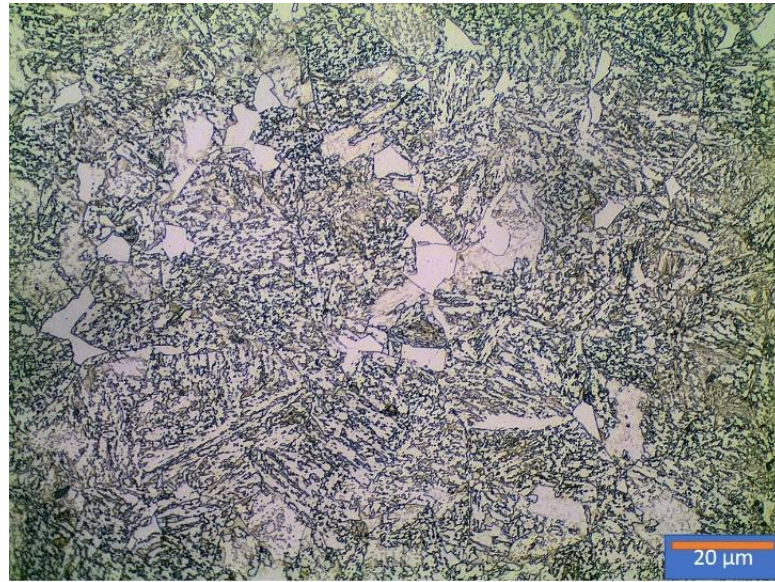
### 3.2.2 Experimental procedures

Table 3.2.1 shows the chemical composition of the low carbon bainitic steel DIN 18MnCrSiMo6-4, which was developed and produced by the Swisstec (Swiss Steel), Emmenbrücke, Switzerland. Fig. 3.2.1 shows the as-received microstructure composed by Granular Bainite (GB), which is characterized by Bainitic Ferrite (White Regions), Retained Austenite (RA) and Polygonal Ferrite (PF) [4].

**Table 3.2.1.** Chemical composition of the experimental DIN 18MnCrSiMo6-4.

Element	C	Si	Mn	S	Ni	Cr	Cu	Mo	Al	Ti	N	Fe
wt. %	0.18	1.19	1.42	0.015	0.063	1.17	0.10	0.27	0.005	0.004	0.01	Bal.

Compression tests in a DIL 805A/T dilatometer of TA instruments were implemented in order to obtain flow curves that represent material's behavior in hot forming conditions. The choice of testing parameters is typical for hot forging using hydraulic and friction presses [18].



**Figure 3.2.1.** As-received microstructure revealed by optical microscopy of the DIN 18MnCrSiMo6-4.

The specimens were cylinders with a height of 10 mm and a diameter of 5 mm. Fig. 3.2.2 shows representative values of the temperature versus time cycle and the main steps in the hot compression tests. The deformation was carried out at temperatures ranging from 1123 K to 1423 K with an interval of 100 K and strain rates of  $0.1 \text{ s}^{-1}$ ,  $0.5 \text{ s}^{-1}$ ,  $1 \text{ s}^{-1}$  and  $5 \text{ s}^{-1}$ . The average heating rate and cooling rate was 10 K/s and 50 K/s, respectively.

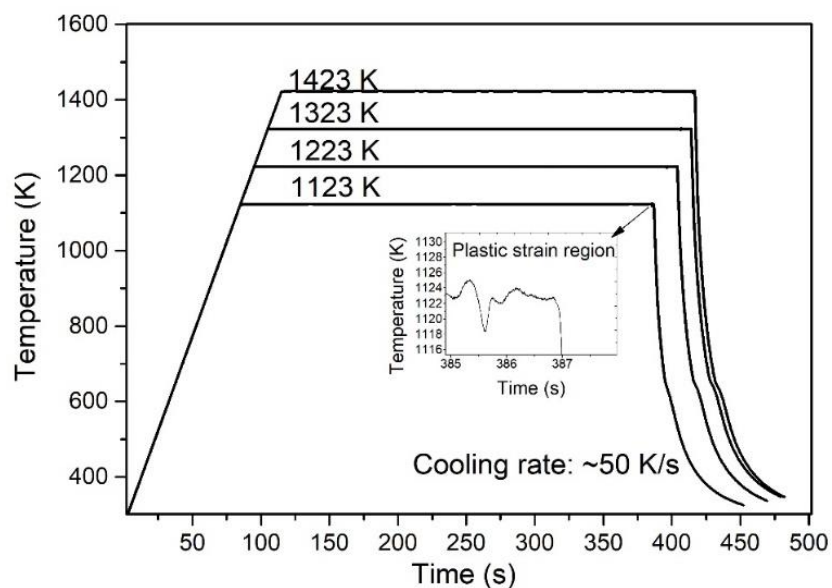


**Figure 3.2.2.** Representation of the hot compression tests.

The samples were heated in vacuum atmosphere until reach the chosen temperature. Then, they were kept at this temperature during 300 s (soaking time), before compressive deformation begins. After compression, the samples were quenched instantaneously by an inert gas flow. In order to reduce friction effects, a tantalum foil was placed at the interface formed by sample and die. The correction for friction effects on flow curves was made according to Han, Y. et al, and the Eq. 3.2.1 shows flow stress data formulation to attained the frictionless effect.

$$\bar{\sigma} = \frac{\sigma}{1 + \left(\frac{2}{3\sqrt{3}}\right)m\left(\frac{r_0}{h_0}\right)\exp\left(\frac{3\varepsilon}{2}\right)} \quad (3.2.1)$$

Where,  $\bar{\sigma}$  is the corrected flow stress,  $\sigma$  is the measured flow stress given in (MPa),  $\varepsilon$  is the measured strain,  $r_0$  and  $h_0$  is initial radius and height in (mm) respectively, finally  $m$  represents the friction factor. Behind of  $m$  value results for each flow stress, there are relations which is calculated only by measuring of the maximum radius,  $Rm$ , and the calculation of the height after the plastic deformation. Detailed formulation and explanation of the procedure can be consulted in [19].

### 3.2.3 Results and Discussion

#### 3.2.3.1 Flow Curves

Fig. 3.2.3 shows the resulting flow stress curves of steel obtained from the hot compression tests at the four different temperatures (from 1123 K to 1423 K) and strain rates (from 0.1 s<sup>-1</sup> to 5 s<sup>-1</sup>). The mean flow stress decreases with temperature increase for the same strain rate and, higher stress gradient can be seen proportional to applied strain rates, when they are compared at same temperatures.

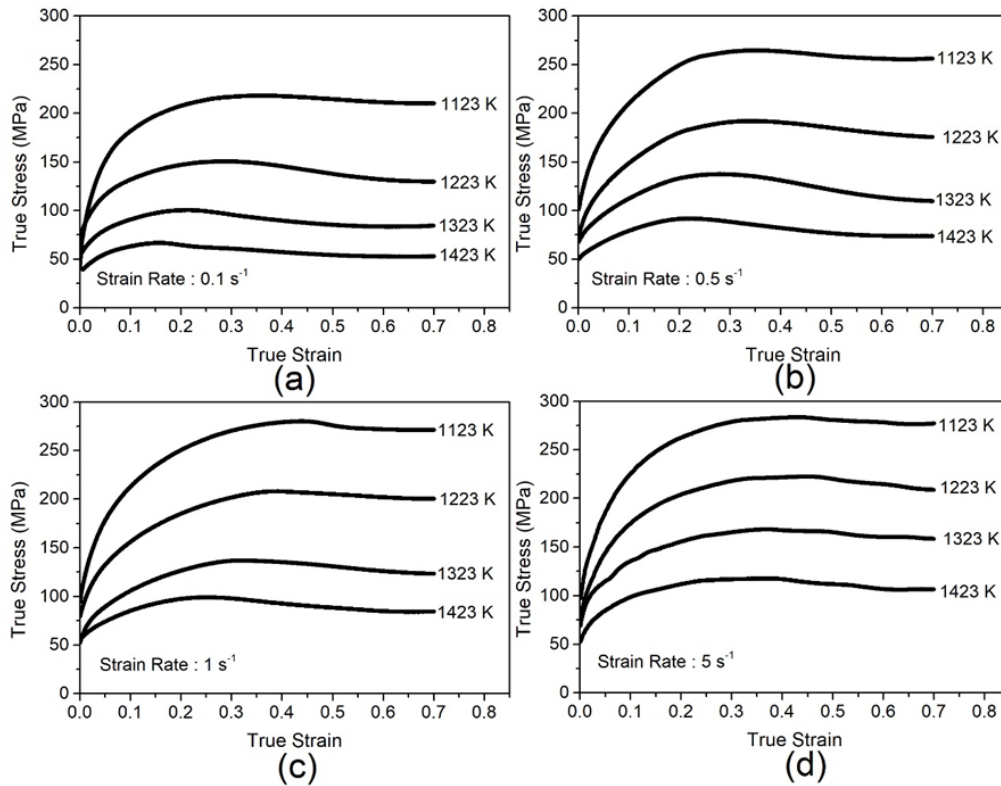


**Figure 3.2.3.** True Stress versus True Strain curves of studied steel at four different strain rates and temperatures (a)  $0.1 \text{ s}^{-1}$ , (b)  $0.5 \text{ s}^{-1}$ , (c)  $1 \text{ s}^{-1}$ , (d)  $5 \text{ s}^{-1}$ .

The activation of dynamic softening is higher when temperature increases in overall curves. However, the gradient between the peak stress and steady state at the same temperature, decreases at higher strain rates, as one can see by comparing Fig. 3.2.3a and Fig. 3.2.3d. For the lowest temperature, 1123K, the maximum stress level variation is lower at all strain rates when compared to the temperature of 1423K, the highest one.

Fig. 3.2.4 shows the surface plot of the strain rate sensitivity variations (Eq. 3.2.2) [18] according to the different strain rate and temperature levels. This behaviour indicates a reduction of strain rate sensitivity ( $\omega$ ) with the temperature, which represents lower dislocation mobility during plastic deformation.

$$\omega = \frac{\partial \text{Log}(\sigma)}{\partial \text{Log}(\dot{\epsilon})_{T,\epsilon}} \quad (3.2.2)$$

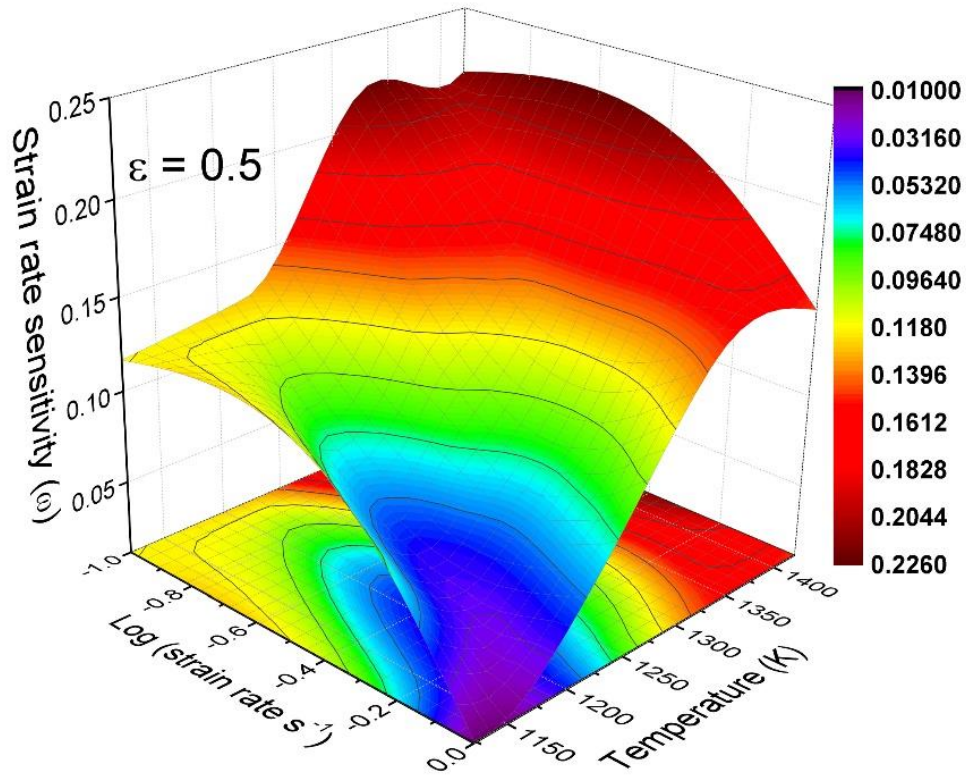


**Figure 3.2.4.** Surface plot of the effect of strain rate and temperature on the strain rate sensitivity at 0.5 of plastic deformation.

In summary, the flow stress for this steel, can be divided into three stages which correspond to work hardening (*WH*), dynamic softening and steady-state stress. The (*WH*), first stage, represents a rapid increase of the material strength due to the accumulation of dislocation and the piling up by barriers, which is increasing with the strain rate [7,20]. The dynamic softening is characterized by the appearance of a second peak in the flow curve, in the second stage of deformation. Hence, the dynamic softening mechanisms occur due to the annihilation and rearrangement of mobile dislocation, demonstrating a DRX characteristic behaviour [12]. The dynamic balance in the dislocations remained constants when the flow curves achieved the third stage and the stress, which is represented in that point the steady-state stress.

### 3.2.3.2 Parametrization of Arrhenius Equation

Flow stress and dynamic recrystallization Kinect were modelled based on equations for low alloy and micro-alloyed steels as given by [7,20,21] where the work-hardening and dynamic recovery have been taken into account. In the flow softening behaviour, the Zener-Hollomon parameter ( $Z$ ) Eq. 3.2.3, representing the strain rate factor in ( $s^{-1}$ ), compensated by temperature.

Arrhenius-type equation, which represents the correlation between flow stress ( $\sigma$ ), temperature and strain rate are available as given in Eq. 3.2.4 and Eq. 3.2.5 for lower stress level. The Eq. 3.2.6 is applied for higher stress levels and for overall stress [13].

Applying natural logarithms of Eq. 3.2.4, Eq. 5 and Eq. 3.2.6, based on experimental data plotted in Fig. 3.2.5a, the coefficient  $n'$  is 6.3858, was obtained through the mean of the linear fits of  $\text{Log } \sigma - \text{Log } \dot{\epsilon}$  in different temperatures. The mean  $\beta$  value obtained by the linear fit, presented in Fig. 3.2.5b is 0.06283. Therefore,  $\alpha$  is the material parameter regulating the peak stress ( $\text{MPa}^{-1}$ ), can be calculated by  $\alpha = \beta/n' = 0.009838$ .

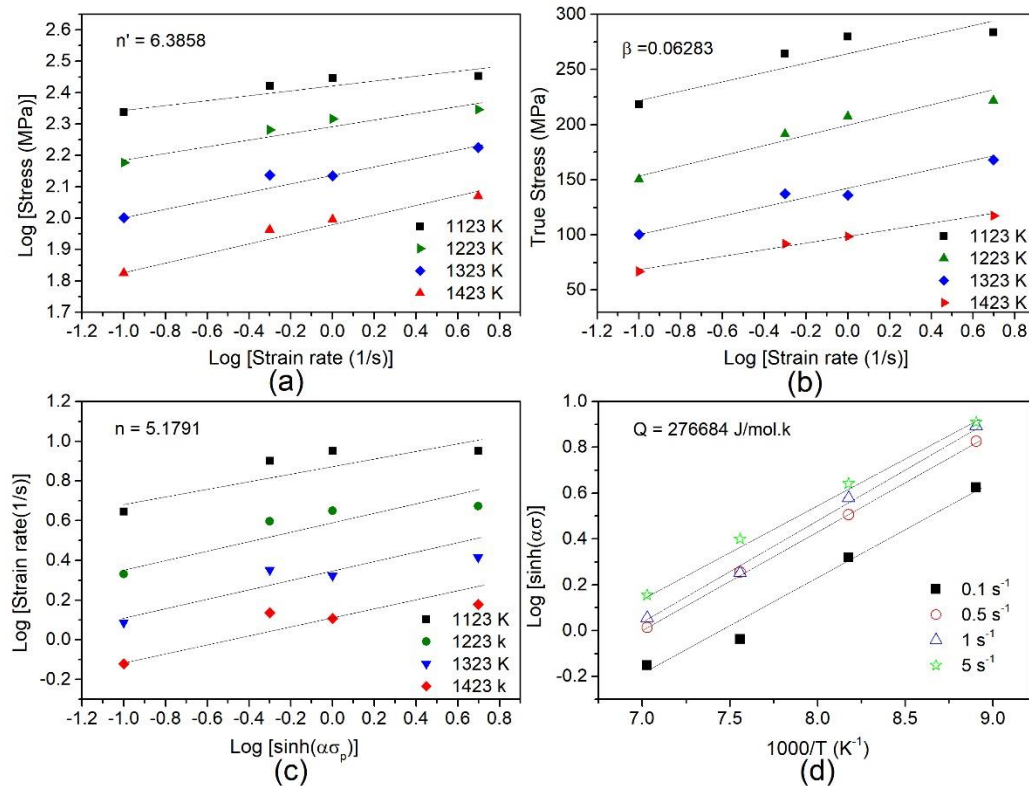


**Figure 3.2.5.** Peak stress and peak strain relationship to determine the coefficients: (a)  $n'$ , (b)  $\beta$ , (c)  $n$ , (d)  $Q$ .

Correlations were established based on these equations to determine the constants  $\alpha$ ,  $n$ ,  $n'$ ,  $Q$  and  $A'$ ,  $A''$ ,  $A$ , for the peak flow stress ( $\sigma_p$ ) and steady- state stress ( $\sigma_{ss}$ ) into determined strain.

$$Z = \dot{\epsilon} \exp\left(\frac{Q}{RT}\right) \quad (3.2.3)$$

$$A' \sigma^{n'} = f(\sigma) = \frac{\dot{\epsilon}}{A} \exp\left(\frac{Q}{RT}\right) \quad (3.2.4)$$

$$A'' \exp(\beta\sigma) = f(\sigma) = \frac{\dot{\epsilon}}{A} \exp\left(\frac{Q}{RT}\right) \quad (3.2.5)$$

$$[\sinh(\alpha\sigma_p)]^n = \frac{Z}{A} = \frac{\dot{\epsilon}}{A} \exp\left(\frac{Q}{RT}\right) \quad (3.2.6)$$

Where  $\dot{\epsilon}$  is the strain rate ( $s^{-1}$ ),  $n$  represent the stress exponent,  $A$  is a material constant,  $Q$  the activation energy ( $J.mol^{-1}K^{-1}$ ) and  $R$  is the universal gas constant ( $8.314 J.mol^{-1}.K^{-1}$ ) multiplied by the absolute temperature in Kelvin (K). The Eq. 3.2.7 is used to determine ( $Q$ ) [11,19,20].

$$Q = Rn \left[ \frac{\partial \log [\sinh(\alpha\sigma_p)]}{\partial \left(\frac{1}{T}\right)} \right] \quad (3.2.7)$$

After obtaining the coefficients  $\alpha$ ,  $n'$ ,  $\beta$  and  $Q$  it was possible to determine the mean value of the coefficient  $A$  and taking the logarithm of Eq. 3.2.8 the equation Eq. 3.2.9 was obtained. Fig. 3.2.6 shows the relationship between  $\log[\sinh(\alpha\sigma)]$  and  $\log Z$  which presents a good correlation for the data plot, therefore,  $\log A$  can be found by the interception of the curve. Finally, an average of the material constant  $A$  is defined as  $7.61 \times 10^{11}$ .

$$\log Z = \log A + n \log[\sinh(\alpha\sigma)] \quad (3.2.8)$$

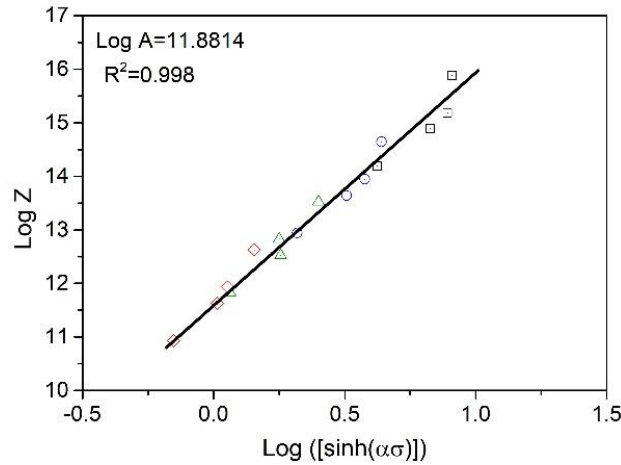


**Figure 3.2.6.** Linear correlation between  $\log[\sinh(\alpha\sigma)]$  and  $\log Z$  under different hot work conditions for the bainitic steel.

As a result, the Zener-Hollomon  $Z$  in ( $s^{-1}$ ) equation for the steel can be described as follows:

$$\dot{\varepsilon} = 7.61 \times 10^{11} [\sinh(0.009838\sigma_p)]^{5.179} \exp\left(\frac{-276684}{RT}\right) \quad (3.2.9)$$

### 3.2.3.3 Determination of recovery (DRV) and (DRX) parameters ( $\sigma_{WH}$ , $\sigma_{sat}$ , $\sigma_p$ , $\sigma_c$ , $\sigma_{SS}$ , $\varepsilon_c$ , $\varepsilon_p$ )

Dislocation density  $\rho$  dependency on plastic strain  $\varepsilon$  is considered by Estrin and Mecking approach [24] and are described in Eq. 3.2.10. Where ( $h$ ) represents the athermal coefficient of work hardening and,  $r$  is the coefficient of dynamic recovery when the strain  $\varepsilon = 0$ ,  $\rho = \rho_0$ , where  $\rho_0$  represents the initial dislocation density. The ratio of  $h/r$  is used to define  $\sigma_{sat}$ , details concerning the equations used in this work can be consulted in [7]. The work hardening rate method ( $\theta = \frac{\partial \sigma}{\partial \varepsilon}$ ) was used in this work to determine these parameters from the flow curves [11].

$$\frac{\partial \rho}{\partial \varepsilon} = h - r\rho \quad (3.2.10)$$

The results lead to the following equation, Eq. 3.2.11, giving the work hardening stress ( $\sigma_{WH}$ ) at the beginning of the compression test and Eq. 3.2.12 describing the overall flow curve:

$$\sigma_{WH} = (\sigma_{sat}^2 - (\sigma_{sat}^2 - \sigma_0^2) \exp(-r\varepsilon))^{1/2} \quad (3.2.11)$$

$$\sigma \frac{\partial \sigma}{\partial \varepsilon} = 0.5r\sigma_{sat}^2 - 0.5r\sigma^2 \quad (3.2.12)$$

Where ( $\sigma_{sat}$ ) is the saturation stress during the hot working conditions.

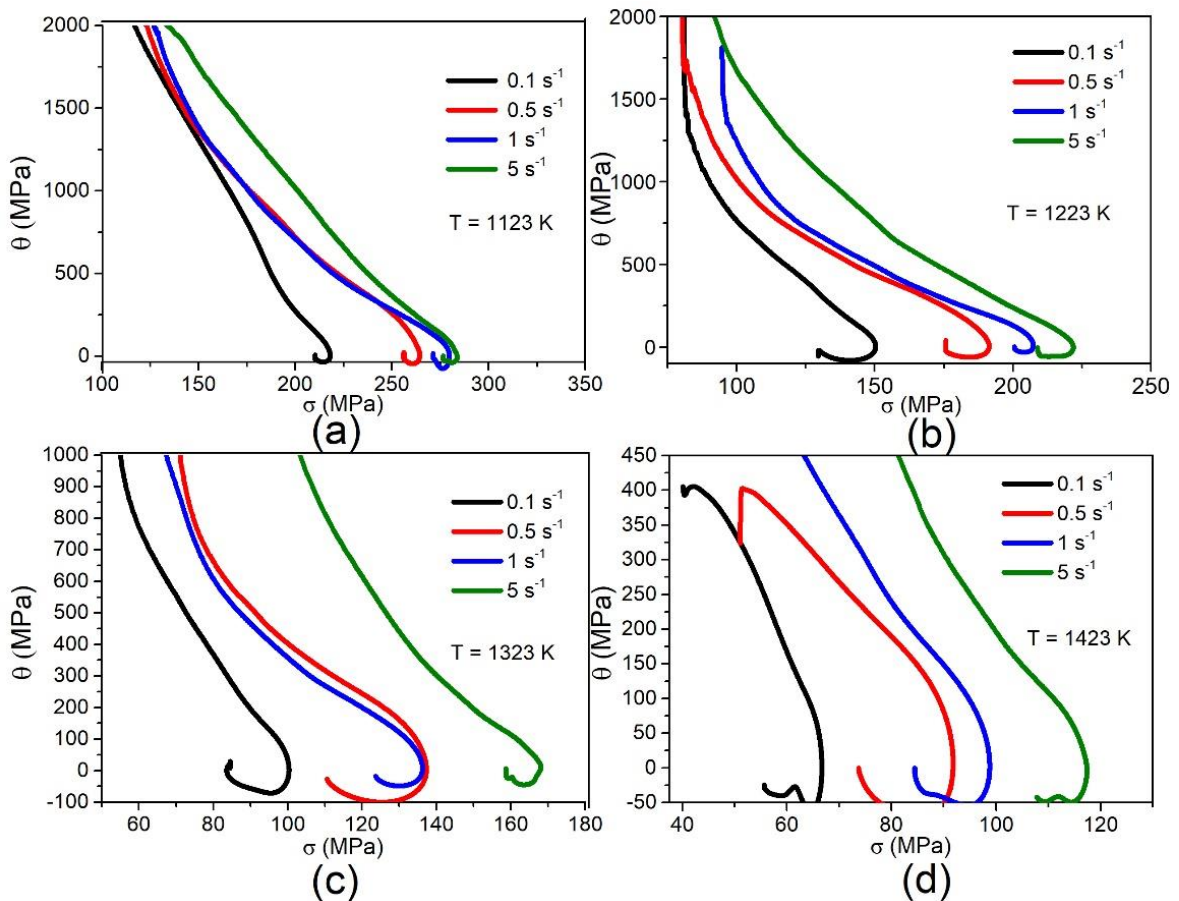


**Figure 3.2.7.**  $\theta$ - $\sigma$  curves on different temperatures and strain rates: (a) 1123 K; (b) 1223 K; (c) 1323 K; (d) 1423 K.

Fig. 3.2.7 shows the specific curvature of the first derivation of work hardening used to determine the  $r$ -coefficient, which generates the curve calculated by  $\theta\sigma$  and plotted as a function of the stress  $\sigma^2$ , as can be seen in the example of Fig. 3.2.8. The slope  $m$  of tangent was used by [7,22] to determine the  $r$  value ( $r = -2m$ ).

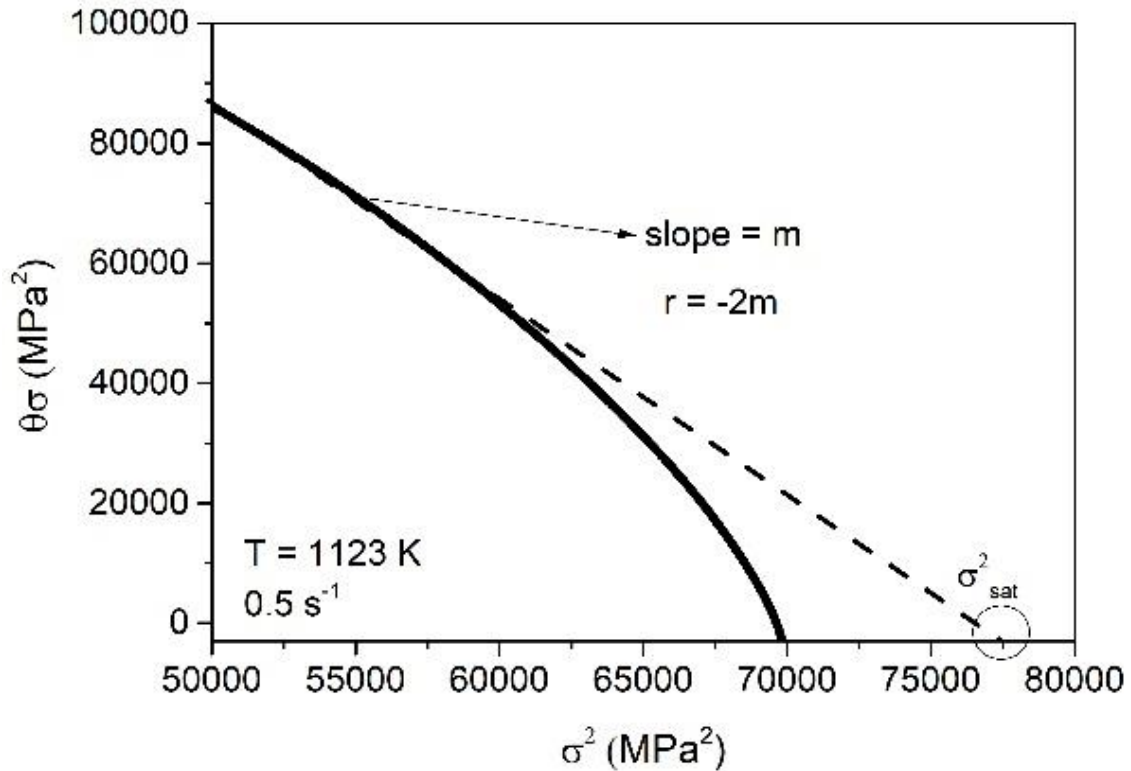


**Figure 3.2.8.** Plot of  $\theta\sigma$  vs.  $\sigma^2$  employed to determine the slope  $m$  for the steel at different temperatures and strain rates.

Table 3.2.2 shows that  $r$  value has a decreasing tendency when the peak stress increase. Moreover, higher values of  $r$  lead the material to develop a saturation stress ( $\sigma_{sat}$ ) more quickly.

The high  $r$ -value is associated with the moderate stacking fault energy (SFE) value of the material, which makes thermomechanically activated mechanisms difficult [23]. This makes dynamic recovery more active during the process, delaying dynamic recrystallization kinetics. According to [7], the addition of alloying elements has a reasonable effect on these parameters changing with strain rate increase. For the DIN 18MnCrSiMo6-4 bainitic steel, in defined conditions of hot working, the  $r$ -value is between 6 and 18.

**Table 3.2.2.** Dynamic recovery parameter ( $r$ ) obtained from the flow curves of DIN 18MnCrSiMo6-4.

Temperature (K)	DRV Parameter $r$ (-)	Peak Stress $\sigma_p$ (MPa)	Saturation stress $\sigma_{sat}$ (MPa)	Strain rate $\dot{\epsilon}$ ( $s^{-1}$ )	Zener Parameter $Z$ ( $s^{-1}$ )
1123	<b>18.3918</b>	218.1109	222.7409257	0.1	1.54282E+14
1123	<b>9.66284</b>	264.395	281.9367837	0.5	7.71412E+14
1123	<b>7.9326</b>	279.68	292.970647	1	1.54282E+15
1123	<b>9.804</b>	283.74	293.211596	5	7.71412E+15
1223	<b>19.54</b>	150.33627	153.0959121	0.1	8.83948E+12
1223	<b>6.9</b>	191.3793	211.6737081	0.5	4.41974E+13
1223	<b>5.9</b>	207.28417	223.8875164	1	8.83948E+13
1223	<b>7.88</b>	221.8566	228.984113	5	4.41974E+14
1323	<b>12.86</b>	100.39	104.6984241	0.1	6.74686E+11
1323	<b>6.14</b>	137.2563	157.6362173	0.5	3.37343E+12
1323	<b>6.1</b>	136.1869	151.4524348	1	6.74686E+12
1423	<b>11.24</b>	167.88	171.2639858	5	3.37343E+13
1423	<b>13.18</b>	66.67	71.02664711	0.1	84634659177
1423	<b>7.34</b>	91.77	113.8972212	0.5	4.23173E+11
1423	<b>7.52</b>	98.78	108.410065	1	8.46347E+11
1423	<b>9.14</b>	117.37	121.586857	5	4.23173E+12

To evaluate the  $h$ - parameter associated with each presented flow curve, the [Eq. 3.2.13](#) was used.

$$h = r_{|T\dot{\epsilon}|} \frac{\sigma_{sat|T\dot{\epsilon}|}^2}{(\alpha\mu b)^2} \quad (3.2.13)$$

Where  $\mu$  is the shear modulus, which was considered 36.06 GPa, according to [7]. The constant  $b$  is the magnitude of Burgers vector of dislocation of austenite, in this work is equal to 0.3606858 nm, according to the equation proposed by [25].

As a result, [Fig. 3.2.9](#) displays the variation of athermal work hardening parameter  $h$  for different peak stresses. It can be observed that  $h$ - parameter increases linearly with the peak stress. The parameter  $h$ -parameter can be interpreted as the mean free path of the dislocations during the plastic strain at the flow curves [7].

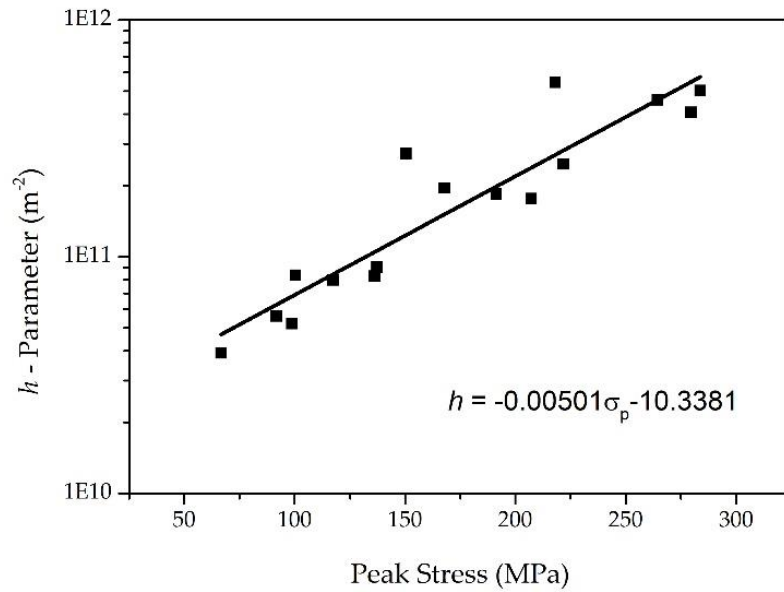


**Figure 3.2.9.** Athermal work hardening ( $h$ ) as a function of peak stress for DIN 18MnCrSiMo6-4 steel.

Fig. 3.2.10a shows the relationship between critical stress, peak stress, critical strain, and peak strain ( $\sigma_p, \sigma_c, \varepsilon_c, \varepsilon_p$ ) respectively, and Fig. 3.2.10b the relation of steady-state stress and Z parameter. It can be noted that there is a linear relationship between the plotted values. As the strain rate increases, the corresponding  $h$ - parameter increase. Therefore, the equations describing the critical strains and peak strain  $\varepsilon_c$ , and  $\varepsilon_p$  for the investigated material, can be written:

$$\varepsilon_c = 0.002375Z^{0.138275} \quad (3.2.14)$$

$$\varepsilon_p = 0.0017575Z^{0.118425} \quad (3.2.15)$$

For the critical and the peak stress  $\sigma_c$  and  $\sigma_p$ :

$$\sigma_c = 6.095475Z^{0.1138} \quad (3.2.16)$$

$$\sigma_p = 9.522275Z^{0.10955} \quad (3.2.17)$$

These values play an essential role to represent the critical condition for initiation of DRX, while the steady-state stress  $\sigma_{ss}$  is related to the competition between dislocation generation and dynamic recovery at hot deformation conditions. Both increase when  $Z$  value increases in a linear correlation, therefore the ratio of  $\sigma_p/\sigma_c$  is about 0.974 and  $\varepsilon_c/\varepsilon_p$  0.54.

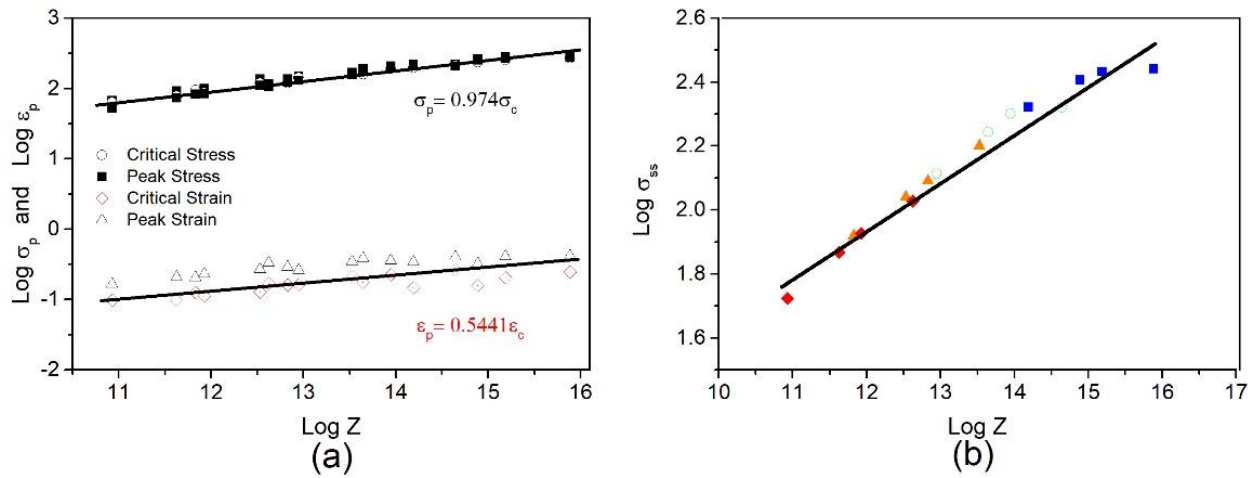


**Figure 3.2.10.** Linear relationship between (a)  $\sigma_p, \sigma_c, \varepsilon_c, \varepsilon_p$  and (b) Steady-state stress for  $Z$  parameter.

Peak flow stress ( $\sigma_p$ ) which is set as a reference to derive the flow stress at any strain ranging from approximately 0 to 0.7, is calculated from the acquired coefficients, and can be described by Eq. 3.2.18.

$$\sigma_p = \frac{1}{\alpha} \ln \left[ \left( \frac{Z}{A} \right)^{1/n} + \sqrt{\left( \frac{Z}{A} \right)^{2/n} + 1} \right] \quad (3.2.18)$$

Therefore, the general equation can be presented in Eq. 3.2.19 for the DIN 18MnCrMoSi6-4 bainitic steel during the hot compression tests, after all, regression analysis.

$$\sigma_p = \frac{1}{0.0098} \ln \left[ \left( \frac{Z}{7.61 \cdot 10^{11}} \right)^{0.1934} + \sqrt{\left( \frac{Z}{7.61 \cdot 10^{11}} \right)^{0.3868} + 1} \right] \quad (3.2.19)$$

### 3.2.3.4 Analysis of the Dynamic Recrystallization DRX Kinetics

The softened fraction ( $X$ ) is presented in Eq. 3.2.20, at any point in the process, is described by the ratio between the differences of DRV and DRX. Where  $\sigma_{WH}$  is the stress at a specific strain given by Eq. 11, and  $\sigma_{sat}$  comes from the square root of the tangent of work hardening showed in Fig.3.2.8.

$$X_{DRX} = \frac{\sigma_{WH} - \sigma}{\sigma_{sat} - \sigma_{ss}} \quad (3.2.20)$$

A consolidate description of DRX kinetics based on the JMAK phenomenological equation, was employed in the present work is indicated by Eq. 3.2.21.

$$X_{DRX} = 1 - \exp \left[ -b \left( \frac{\varepsilon - \varepsilon_c}{\varepsilon_p} \right)^\tau \right] \quad (3.2.21)$$

The exponent ( $b$ ) represents the Avrami coefficient, therefore it is sensitive to variations in temperature while, the Avrami exponent ( $\tau$ ) is related to the mechanism of phase transformation. Thereby, combining Eq. 3.2.20 and Eq 3.2.21, and taking natural logarithm on the kinetic model of DRX can give Eq. 3.2.22.

$$\ln. \ln \left( \frac{1}{X} \right) = \ln b + n \ln \left( \frac{\varepsilon - \varepsilon_c}{\varepsilon_p} \right) \quad (3.2.22)$$

As a result of the substitution of obtained values ( $\sigma_{WH}, \sigma_{sat}, \sigma_p, \sigma_{ss}, \varepsilon_c, \varepsilon_p$ ) under all process conditions into Eq. 3.2.19, the Avrami coefficient ( $\tau$ ) and exponent ( $b$ ) can be found by linear regression at different levels of strain rate and temperature. All the softening data from the flow curves were converted into time (s) format using the ratio between the strain and strain rate ( $s^{-1}$ ) as presented in Eq. 3.2.23 [7]. Fig. 3.2.11 displays the JMAK plot for the steel in different temperatures. As mentioned by [7], when increasing the temperature, the kinetics rises the softening rate during the plastic deformation.

$$t = \left( \frac{\varepsilon - \varepsilon_c}{\dot{\varepsilon}} \right) \quad (23)$$

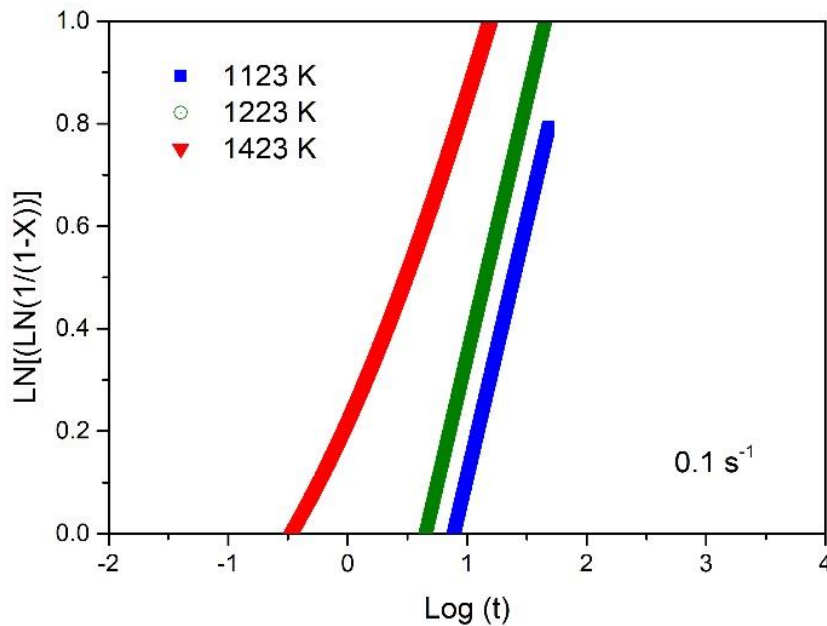


**Figure 3.2.11.** JMAK plot for 18MnCrSiMo6-4 during the hot compression showing the effect of the temperature in the softening rate.

The slope of the curves gives the Avrami's exponent, which decreases according to the reduction in temperature, as can be seen in Fig. 3.2.11. After a series of adjustments in different temperatures and strain rates, it was verified that the average value of the coefficients ( $b$ ) and ( $\tau$ ) are 0.597 and 1.798, respectively. Eq. 3.2.24 shows the JMAK equation for DIN 18MnCrSiMo6-4 bainitic steel:

$$X_{DRX} = 1 - \exp \left[ \left( -0.597 \left( \frac{t}{t_{0.5}} \right) \right)^{1.798} \right] \quad (3.2.24)$$

Where  $t_{0.5}$  is [6]:

$$t_{0.5} = A'Z^{-q}d_o^v \exp\left(\frac{Q}{RT}\right) \quad (3.2.25)$$

The coefficient ( $b$ ) and ( $\tau$ ) are close to the values found in the literature [11] for high carbon silicon-rich bainitic steels. Parameters  $q$  and  $v$  are considered as 0.4 and 2 respectively, according to [7]. Fig. 3.2.12a and Fig. 3.2.12b represents two possibilities of the time reduction for the complete recrystallization mechanism, one when increasing the temperature and other due to the high strain rate levels.

Hence, the time required for 50% of the softened fraction to occur during deformation depends on both process condition. The value of  $t_{0.5}$  decreases with the increase in temperature and has a considerable influence on the strain rate. It is known that high strain rates increase the driving force for nucleation mechanisms to occur during dynamic recrystallization [8, 11, 16]. Therefore, the increase of migration rate of dislocations and grain boundaries is one of the consequences of accelerating the DRX process. It can be observed in Fig. 12b, that at the higher strain rates, there is no time available for the new recrystallized grains to grow up and therefore a finer grain size is expected [11,16].

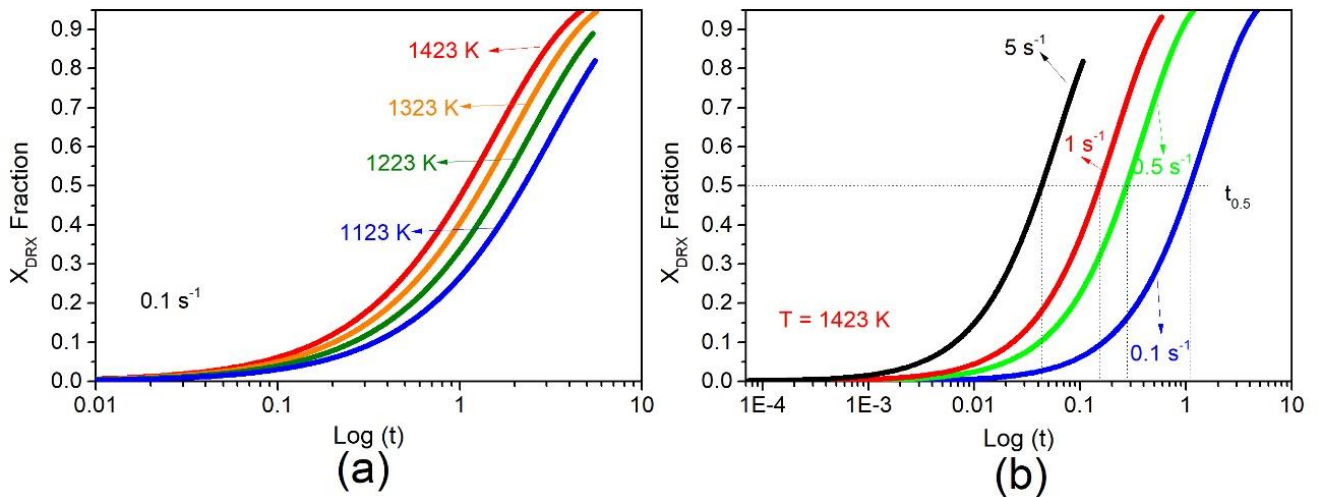


**Figure 3.2.12.**  $X_{DRX}$  volume fraction of recrystallized grains during the hot working condition as a function of (a) Temperature, (b) Strain rate.

### 3.2.3.5 Modelling Flow Curves

After the acquisition of all the coefficients necessary to obtain the parameters of work hardening, dynamic recrystallization and dynamic recovery, the models proposed by [15] and [16] were applied. It was compared the accuracy of the proposed flow curves model for bainitic steel. The flow curves were modeled taking into account higher plastic deformation values for two models.

The model [15] considers, the effect of plastic strain temperature as well as the strain rate based on the Arrhenius model. They are represented by the Zener-Hollomon parameter, as given in Eq. 3.2.26:

$$\sigma_{mod1} = \frac{k_0}{\alpha} \varepsilon^{k_1} \exp(-k_2 \varepsilon) \sigma_p \quad (3.2.26)$$

Where  $k_0$ ,  $k_1$  and  $k_2$  are constants of the material, and the variation depending on the degree of plastic deformation and temperature as well as  $\sigma_p$  is the peak stress from Eq. 3.2.17. After linear regressions, a relation of these parameters was obtained with the Zener-Hollomon parameter, and they are presented in Eq. 3.2.27, 3.2.28 and 3.2.29.

$$k_0 = 3.17 \ln(Z) + 0.12 \quad (3.2.27)$$

$$k_1 = 0.02 \ln(Z) - 0.09 \quad (3.2.28)$$

$$k_2 = 0.05848 \ln(Z) + 0.795 \quad (3.2.29)$$

These relations were compared with the Avrami-type model proposed by Laasraoui and Jonas [26] and applied by [16,17] in Eq. 3.2.30, which takes into account the work-hardening, dynamic recrystallization and dynamic recovering parameters. Thereby, it is possible to extrapolate these flow curves for non-achievable laboratory parameter testing [7,16], for example in hot forging processes for where the strain rates can reach values above  $100 \text{ s}^{-1}$  with screw presses, for example [18].

$$\sigma_{mod2} = \sigma_{WH} - [\sigma_{sat} - \sigma_{ss}] \left( 1 - \exp \left( -b \left( \frac{t}{t_{0.5}} \right)^\tau \right) \right) \quad (3.2.30)$$

Fig. 3.2.13 compares experimental plastic flow curves with those modelled analytically for different conditions of strain rate and temperature. It is noticeable that in general, there is a good agreement between the experimental results with the proposed model by [15], the combination of Eq. 3.2.19 and Eq. 3.2.26 and therefore, is possible to implement in numerical models.

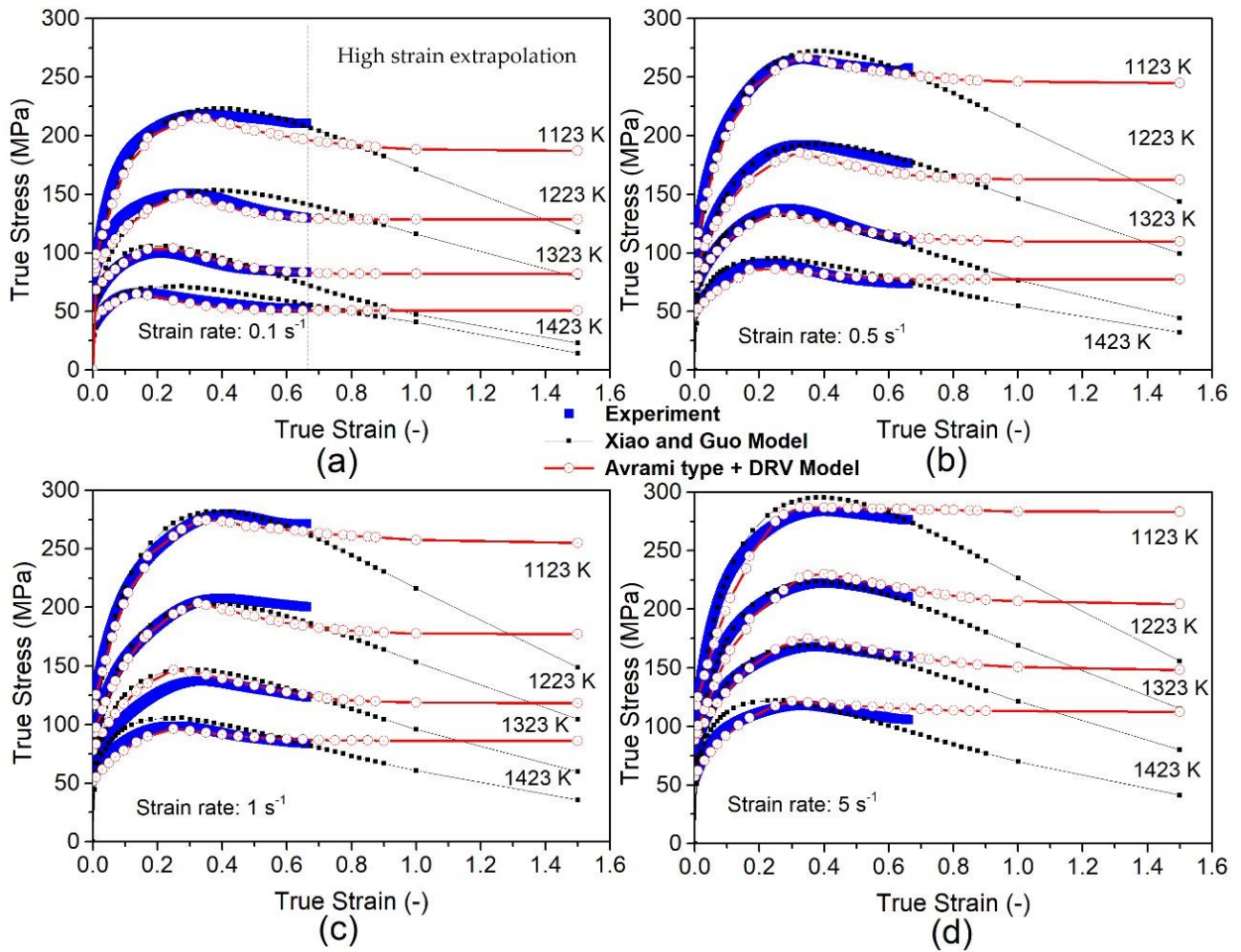


**Figure 3.2.13.** Comparison between experiment flow curves and the two different models with high strain extrapolation for the DIN 18MnCrSiMo6-4 steel for different strain rates and temperatures, (a) Strain rate  $0.1\text{ s}^{-1}$ , (b)  $0.5\text{ s}^{-1}$ , (c)  $1\text{ s}^{-1}$  and (d)  $5\text{ s}^{-1}$ .

However, the relation offered by [16], for more considerable plastic strain tends to reach zero or even negative values which do not represent a physical behaviour when compared to the

model proposed by [15]. Hence, to represent a real material flow after the stress dropping due to *DRX* behaviour, the state saturations stress ( $\sigma_{sat}$ ) may be considered to remain constant at the steady-state stress ( $\sigma_{ss}$ ), which was better described by Avrami model given by [Eq. 3.2.30](#).

### 3.2.4 Conclusions

This paper showed detailed investigations to experimentally determined and numerically model the flow curves of low-carbon high silicon bainitic steel DIN 18MnCrSiMo6-4 in hot working conditions by isothermal compression test. The following main conclusions were obtained:

1. Algebraic equations of the flow curves have been derivated of hyperbolic sine, which showed a linear behaviour with the Zener-Hollomon parameter. The general equation of the peak stress for the steel has been defined.
2. Dependence on the increasing of dislocation density with the plastic deformation was taken into account during the plastic strain to model implementation. Therefore, the dynamic recovery parameters (DRV) were determined in the different process conditions, expanding the application for higher high strain rates than those achievable laboratory testing.
3. The parameters of JMAK equation governing behaviour during dynamic recrystallization for the specific steel under investigation were determined.
4. Finally, two different models were compared to experimental obtained flow curves, and then used to extrapolate the results to higher strains. Both models gave a good approximation with the experimental values up to 0.69 of plastic strain. However, only the Avrami-Type model physically demonstrated the dynamic recovery behavior remaining the stress constant for higher strain levels. Therefore, this model should be preferentially implemented in massive forming operation which can lead to very high strain levels.

## Acknowledgement

The authors acknowledge the *Brazilian agency CAPES (Project 1844/2017) and the Deutsch Forschungsgemeinschaft (German Research Foundation – DFG)* via project EP 128/6-2 (*Project number 327887503*) for the financial support within the BRAGECRIM program (*Brazilian German Cooperation Research in Manufacturing*). The authors also thanks the Metal Forming Institute IBF- RWTH Aachen in Germany for the support during experimental data acquisition. Thiago M. Ivaniski and Alexandre da S. Rocha also acknowledge CNPq (process numbers 167948/2017-2 and 308773/2018-7) for the grants.

### 3.2.5 References

- [1] Bhadeshia, H. K. D. H.; Gomez, G.; Pe, T. Air cooled bainitic steels for strong , seamless pipes Part 2 – properties and microstructure of rolled material. *Mater. Sci. Tech.* 2009 [s. l.], v. 25, n. 12, p. 1–5.
- [2] Caballero, F. G.; Capdevila, C.; Chao, J. The Microstructure of Continuously Cooled Tough Bainitic Steels. *2nd International Conference of Super-High Strength Steels*, 2010 [s. l.], p. 10–18.
- [3] Roelofs, H. et al. Continuously cooled bainitic steel HSX ® Z12 : one decade of experience. *4th Int. Conf. On Steels in Cars and Trucks*, 2014, [s. l.].
- [4] Silveira, A. C. de F. et al. Influence of Hot Forging Parameters on a Low Carbon Continuous Cooling Bainitic Steel Microstructure. *Metals*, 2020 [s. l.], v. 10, n. 5, p. 601.
- [5] Shkatov, Valeriy; Mazur, Igor. Modeling the dynamic recrystallization and flow curves using the kinetics of static recrystallization. *Materials*, 2019 [s. l.], v. 12, n. 18.
- [6] Jorge Junior, A.M.; Balancin, O. Prediction of steel flow stresses under hot working conditions. *Materials Research*, 2005 [s. l.], v. 8, n. 3, p. 309–315.
- [7] Jonas, J. J. et al. The Avrami kinetics of dynamic recrystallization. *Acta Materialia*, 2009 [s. l.], v. 57, n. 9, p. 2748–2756.

- [8] Ivaniski, T. M. et al. Austenitic grain size prediction in hot forging of a 20MnCr5 steel by numerical simulation using the JMAK model for industrial applications. *Materials Research*, 2019 [s. l.], v. 22, n. 5.
- [9] Irani, Missam; Joun, Mansoo. Determination of JMAK dynamic recrystallization parameters through FEM optimization techniques. *Computational Materials Science*, 2018, [s. l.], v. 142, p. 178–184.
- [10] Bylya, Olga et al. Applicability of JMAK-type model for predicting microstructural evolution in nickel-based superalloys. *Procedia Engineering*, 2017, [s. l.], v. 207, n. January, p. 1105–1110.
- [11] Yang, Z. et al. Study on hot deformation behaviour and processing maps of low carbon bainitic steel. *Materials and Design*, 2015 [s. l.], v. 66, n. PA, p. 258–266.
- [12] Han, Y. et al. Hot deformation and processing window optimization of a 70MnSiCrMo carbide-free bainitic steel. *Materials*, 2017 [s. l.], v. 10, n. 3, p. 1–18.
- [13] Han, Ying et al. Effects of temperature and strain rate on the dynamic recrystallization of a medium-high-carbon high-silicon bainitic steel during hot deformation. *Vacuum*, 2018, [s. l.], v. 148, p. 78–87.
- [14] Bevilaqua, W. L et al. In Situ Investigation of the Bainitic Transformation from Deformed Austenite During Continuous Cooling in a Low Carbon Mn-Si-Cr-Mo Steel. *Metallurgical and Materials Transactions A: Physical Metallurgy and Materials Science*, 2020, [s. l.], v. 51, n. 7, p. 3627–3637.
- [15] Xiao, Y. H.; Guo, C. Constitutive modelling for high temperature behavior of 1Cr12Ni3Mo2VNbN martensitic steel. *Materials Science and Engineering A*, 2011 [s. l.], v. 528, n. 15, p. 5081–5087.
- [16] Mirzadeh, H.; Najafizadeh, A. Extrapolation of flow curves at hot working conditions. *Materials Science and Engineering A*, 2010 [s. l.], v. 527, n. 7–8, p. 1856–1860.
- [17] Chen, X. M. et al. Dynamic recrystallization behavior of a typical nickel-based superalloy during hot deformation. *Materials and Design*, [s. l.], 2014, v. 57, p. 568–577.

- [18] Prasad, Y. V. R. K.; Rao, K. P.; Sasidhara, S. Hot working guide: A compendium of processing maps. 2015 ASM International, [s.l: s.n.].
- [19] Han, Ying et al. A comparative study on constitutive relationship of as-cast 904L austenitic stainless steel during hot deformation based on Arrhenius-type and artificial neural network models. *Computational Materials Science*, 2013, [s. l.], v. 67, p. 93–103.
- [20] Liu, M; Ma, Q; Luo, J. Microstructure Evolution and Flow Stress Model of a 20Mn5 Hollow Steel Ingot during Hot Compression. *Materials*, 2018 [s. l.], p. 1–15.
- [21] Sellars, C. M.; Whiteman, J. A. Recrystallization and grain growth in hot rolling. *Metal Science*, 1978 [s. l.], v. 13, n. April, p. 187–194.
- [22] Zou, D. N. et al. On dynamic recrystallisation under hot working of superaustenitic stainless steel. *Materials Science and Technology*, 2014 [s. l.], v. 30, n. 4, p. 411–417.
- [23] Silva, E. S. et al. Hot deformation behavior of an Nb- and N-bearing austenitic stainless steel biomaterial. *Materials Science and Engineering A*, 2012 [s. l.], v. 543, p. 69–75.
- [24] Estrin, Y.; Mecking, H. A unified phenomenological description of work hardening and creep based on one-parameter models. *Acta Metallurgica*, 1984 [s. l.], v. 32, n. 1, p. 57–70.
- [25] Seki, Ichiro; Nagata, Kazuhiro. Lattice constant of iron and austenite including its supersaturation phase of carbon. *ISIJ International*, 2005 [s. l.], v. 45, n. 12, p. 1789–1794.
- [26] Laasraoui, A. , Jonas, J.J. Prediction of steel flow stresses at high temperatures and strain rates. *Metallurgical and Materials Transactions A*, 1991, [s. l.], v. 22, n. 7, p. 1545–1558.

**Numerical and experimental study of an industrial case for grain size evolution in bainitic steel in controlled hot forging and its influence on mechanical performance**

Artigo publicado no periódico Materials Research, Volume 23, N° 5, 2022. Páginas. 1-17.

### 3.3 Numerical and experimental study of an industrial case for grain size evolution in bainitic steel in controlled hot forging and its influence on mechanical performance

Ivaniski T. M.<sup>a\*</sup>, Castro P. J.<sup>a</sup>, Rodrigues D.<sup>a</sup>, Épp J<sup>b,c</sup>., Nunes, R. M.<sup>a</sup>., Rocha A. da S.<sup>a</sup>

<sup>a</sup> Laboratório de Transformação Mecânica – Centro de Tecnologia –Departamento de Metalurgia-  
Universidade Federal do Rio Grande do Sul – Porto Alegre, RS, Brazil;

<sup>b</sup> Leibniz-Institut für Werkstofforientierte Technologien – IWT, Bremen, Germany

<sup>c</sup> MAPEX Centre for Materials and Processes, University of Bremen, Germany

[\\*thiago.ivaniski@ufrgs.br](mailto:*thiago.ivaniski@ufrgs.br)

**Abstract:** Controlling the recrystallization is an important way to reach grain size refinement and outstanding strength and toughness on alloy metals. This study sets out the application and investigation of mathematical microstructure modeling of a newly designed bainitic steel for hot forging industrial applications. The macro-scale model was used to observe and predict the austenitic grain size behavior during the controlled forging of a gear. Arrhenius grain growth kinetic and recrystallization model for a new class of bainitic steel was established for the given ranges of strain rate and temperatures. This model was calibrated through microscopic analysis and used to simulate the unpublished constants of low alloyed bainitic forging steel DIN 18MnCrSiMo6-4 microstructure module using DEFORM® commercial finite element code. The increased temperature due to the adiabatic effect was investigated by numerical analysis, demonstrating its influence on grain coarsening. Local tensile test and Charpy-V notch were compared at different industrial hot forging temperatures and local plastic strain. Changes in yield strength and ductility have demonstrated the grain size influence on the processing parameters. The employed numerical model was an efficient tool to predict and present an alternative path to develop robust industrial forging using semi-empirical models.

**Key Words:** *Hot Forging, Grain Size, JMAK, Mechanical Properties, Bainitic Steel.*

#### 3.3.1 Introduction

Engineers and scientists have transformed how low alloyed carbon steels are designed and processed in the last decades. The relationship between tailored metals processing, microstructure, and mechanical properties remains challenging, especially when more energy-efficient and environmentally friendly products are on the global manufacturing agenda. Advanced bainitic steels have stood out in the last decades [1,2,3,4] due to the excellent combinations of mechanical properties such as yield strength and toughness caused by their microconstituents. One way to obtain such mechanical properties is prior austenitic grain size modification. It is known that coalescence of the bainite laths is avoided by grain refinement, and it increases the volume fraction and stability of retained austenite in isothermal heat treatment [5]. Although it is an excellent

method for this diffusional transformation, its mechanical performance is achieved at the cost of high energy consumption, making it less attractive in hot forged parts manufacturing chains.

As an alternative, the thermomechanical process in continuous cooling bainitic steels can lead to energy savings and tailored mechanical performance by controlling forging and cooling conditions, replacing long isothermal treatments such as quenching and tempering (Q&T) [2,4]. Therefore, understanding how these steels perform in hot forging applications is undoubtedly necessary to achieve excellent mechanical properties. Efforts in understanding the bainitic transformation after the lower plastic strain was reported by [6] using in situ XRD experiments coupled with a dilatometer. Microstructure transformations in continuous cooling were accelerated after compression, and simultaneously, the granular bainite and retained austenite were refined. Another work [7] showed the effect of the plastic strain of metastable austenite on resulting bainite morphology by physical simulation. It has presented the doorway for the forging application using the DIN 18MnCrSiMo6-4 steel in different thermomechanical routes.

Silveira and co-workers [8] found that, besides the forging having a significant impact on the morphology of the bainite, at 1200 °C, a predominantly bainitic microstructure was formed from the coarse austenitic grains. They also summarized that plastic deformation at high temperatures inhibits the formation of pro-eutectoid ferrite, thus favoring the transformation of austenite into bainite [7,8]. When the temperature was reduced to 1100 °C or 1000 °C, in addition to displaying more refined grains, there was an increase in the amount of polygonal ferrite and a reduction in retained austenite fraction. In summary, the austenitic grain significantly impacts the final microstructure of DIN 18MnCrSiMo6-4 steel.

In this way, and as acquired in an early work [9], the modeling of the flow curves of this material, as well as the (JMAK) "Johnson-Mehl-Avrami-Kolmogorov" parameters [10], are necessary for assessing its microstructural evolution such as in recrystallization kinetics. Thus, enabling the application of "semi-empirical" numerical models, based on methods previously proposed by [11-17], which can simulate the complexity of the hot forging process and the grain size evolution.

Although the new methodology [11,13] is excellent for predicting grain size evolution and flow curves through the JMAK equation, it has not yet been applied in industrial hot forging in high strain rate presses (above 50 s<sup>-1</sup>) in this bainitic steel. Also, the kinetics of austenitic grain

growth industrial closed die hot forging after load release has not been discussed using a finite element FEM method approach. A higher strain rates increase dislocation density and stored energy during the plastic deformation, affecting recrystallization kinetics and possibly the grain growth [10]. In closed die forging, such behavior is expected. Therefore, in the present research, the suitability of these proposed methods was addressed in industrial hot forging conditions in a high strain rate press.

This work aimed at validating a macroscale model of the grain size evolution using numerical simulation for a new continuously cooled bainitic steel DIN 18MnCrSiMo6-4 hot forged. Some aspects regarding recrystallization during forging were addressed and what effects the process caused on grain growth. The synergetic effect between closed die forging parameters in response to austenitic grain size at the end of the process has been verified. Finally, it has compared two temperature levels on the mechanical properties.

### 3.3.2 Materials and Methods

#### 3.3.2.1 Grain Growth Kinetic of Annealing test

All experiments were performed with the steel DIN 18MnCrSiMo6-4, classified as a low-carbon carbide-free bainitic steel grade. The chemical composition is given in [Table 3.3.1](#).

**Table 3.3.1.** Chemical composition for steel 18MnCrSiMo6-4, mass percentage.

Element	C	Si	Mn	Ni	Cr	Cu	Mo	Al	Ti	N	Fe
Ma. %	0.18	1.19	1.42	0.063	1.17	0.10	0.27	0.005	0.004	0.01	Bal.

The evolution of the austenitic grain size of this steel was studied by [8], considering the same sample mass of 515.47 g in a cylindrical geometry under isothermal conditions. The authors heated the samples at temperatures of 1000 °C, 1100 °C, and 1200 °C. It was found that the abnormal grain growth occurred at 1200 °C, which was attributed to the dissolution of precipitates formed by microalloying elements such as Ti, N, and Al in this steel. The reported results significantly explain the grain growth equation values, where the methodology is shown below to

be discussed in the results section. Fig. 1 shows the as received prior austenitic grain size PAGS and the microstructure of the steel revealed as the same methodology written in **section 3.3.2.3**.

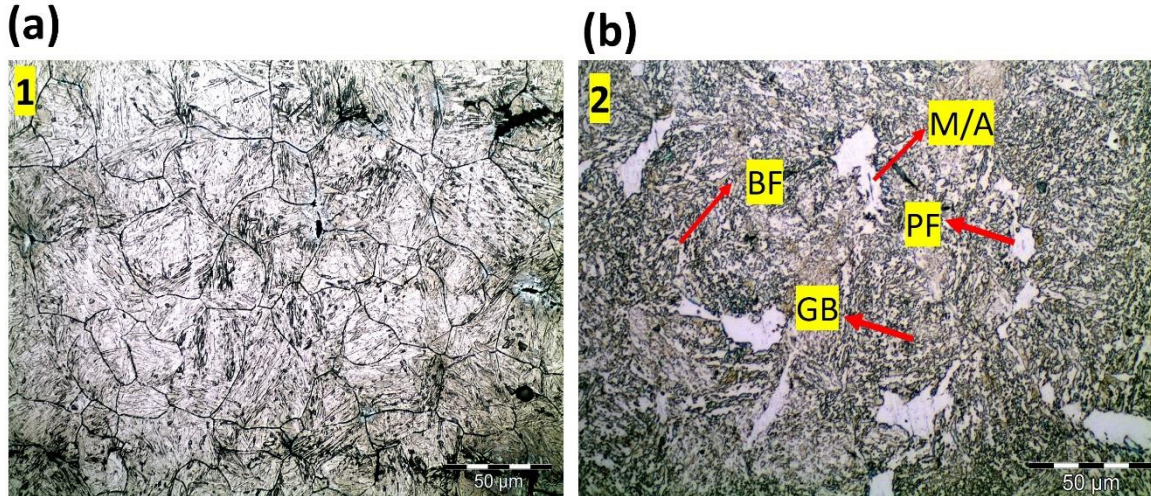


**Figure 3.3.1.** (a) 1 PAGS as received 23,5 μm, (b) 2 Initial Microstructure BF – Bainitic Ferrite, GB – Granular Bainite, PF – Polygonal Ferrite, A – Retained Austenite, M – Martensite.

The constitutive Arrhenius equation was used to describe the kinetics of grain growth [13]. In addition, the activation energy for this bainitic steel was determined, according to Eq. 3.3.1 implemented in DEFORM® V. 11.0 subroutine.

$$d = d_0^m + a_9 t \exp\left(-\frac{Q_{gg}}{RT}\right)^{1/m} \quad (3.3.1)$$

The initial and final grain sizes are given by  $d_0$  and  $d$ , while  $Q_{gg}$  describes the activation energy necessary for the grain growth to occur. The inverse of the time  $t$  exponent for grain growth is given by  $m$ , and  $a_9$  is a constant that depends on the chemical composition of the steel [18]. The R-value is the universal gas constant (8,314 J/mol.K), and  $T$  the absolute temperature in Kelvin (K). By applying natural logarithm to both sides of Eq. 3.3.1), we can determine  $m$  (Eq. 3.3.2) and  $Q_9$  (Eq. 3.3.3) values, and it can be expressed as [13]:

$$\frac{1}{m} = \left(\frac{\partial \ln d}{\partial \left(\frac{1}{t}\right)}\right)_T \quad (3.3.2)$$

$$Q_9 = -mR \left( \frac{\partial \ln d}{\partial \ln T} \right)_t \quad (3.3.3)$$

In this case, it is important to emphasize that the equation describing growth does not consider prior plastic deformation. Moreover, the grain size distribution was assumed to be homogeneous since the measurements of the grain size were the same in distinct parts of the cylindrical rod obtained.

### 3.3.2.2 Flow Curves and Microstructure Analysis

Hot isothermal compression tests for flow curves determination were conducted in a DIL 805A/T dilatometer. Cylindrical samples with 10 mm x 5 mm were heated at a rate of 10 °C/s and held for five (5) minutes for homogenization before compression. Strain rates of 0.1 s<sup>-1</sup>, 0.5 s<sup>-1</sup>, 1 s<sup>-1</sup>, and 5 s<sup>-1</sup> and temperatures of 850 °C, 950 °C, 1050 °C, and 1150 °C with a fixed true plastic strain of 0.69 were set up for testing.

### 3.3.2.3 Metallography Analysis

After isothermal compression and quenching, the austenitic grain size samples were prepared and analyzed by optical microscopy according to DIN EN ISO 643 and ISO 14250 using the line-intercept method. A saturated picric acid solution revealed the grain boundary (AGB) with 42 mL of wetting agent, 58 mL of distilled water, and 2.3 g of picric acid. Wetted cotton was swabbed into the steel surface for 5 min to reveal the (AGB). The overall microstructure was etched by immersion in a Nital 2% solution for 10 s.

Electron backscatter diffraction (EBSD) was performed using a Philips XL 30 to determine the distribution of the crystallographic units. The instrument operated at 25 keV, with a working distance of 8.4 mm, a sample tilt angle of 75 degrees, and a step size of 0.1 μm. The data were processed in Orientation Imaging Microscopy for two quenched samples in temperatures of 950 °C and 1150 °C at  $\dot{\epsilon} = 0.1 \text{ s}^{-1}$  of plastic strain rate.

### 3.3.2.4 Recrystallization Model

The modeled flow curves obtained by compression tests and the JMAK recrystallization coefficients were implemented in DEFORM® finite element code V11.0. Fig. 3.3.2 shows the flowchart used for the acquisition of the coefficients.

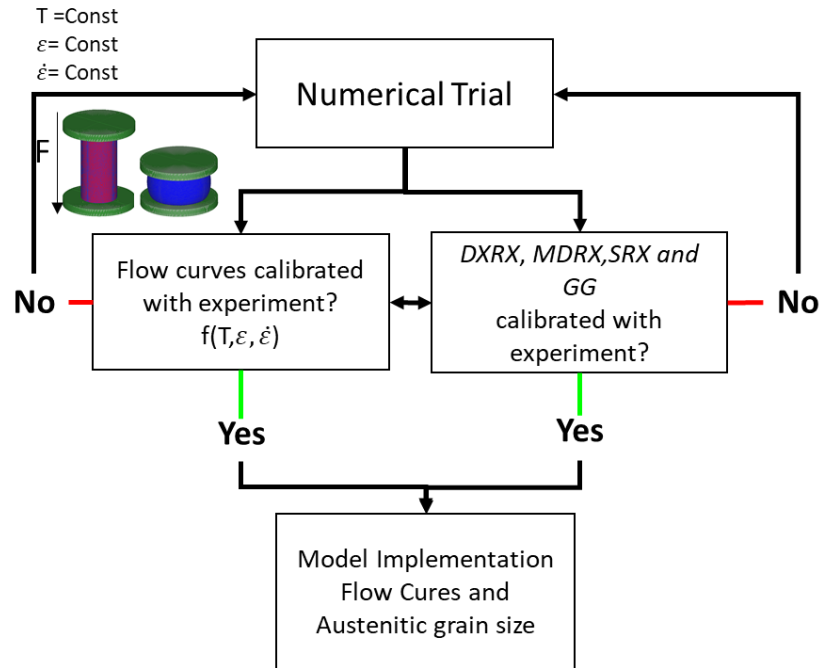


Figure 3.3.2. Flowchart of modeling interaction to calibrate the experiment.

The Zener-Hollomon parameter  $Z$  was calculated using Eq. 3.3.4, and the overall equation that depends on it is shown in Eq. 5.

Where  $Z$  is:

$$Z = \dot{\varepsilon} \cdot \exp\left(\frac{Q}{RT}\right) \quad (3.3.4)$$

In Eq. 3.3.5,  $n$ ,  $\alpha$ , and  $A$  are the material-dependent constants, determined by experimental flow curve results, and  $Q$  is the activation energy in (J/mol.K) for the onset of dynamic recrystallization.

The parameters determined from flow stress curves for the DIN 18MnCrSiMo6-4 steel were  $\alpha = 0.009833 \text{ MPa}^{-1}$ ,  $n = 5.3$ ,  $A(T, \dot{\epsilon}) = 7.6 \times 10^{11}$  and  $Q_{Total} = 276684 \text{ J/mol.K}$  [9]. The peak stress  $\sigma_p$  was defined by deriving the stress and strain from the flow curves ( $\theta = \frac{\partial \sigma}{\partial \epsilon}$ ).

$$\dot{\epsilon} = A[\sinh(\alpha \sigma_p)]^n \exp\left(\frac{Q}{RT}\right) \quad (3.3.5)$$

The modeled flow stress in the subroutine of the finite element code is shown in Eq. 3.3.6, where the work hardening  $\sigma_{WH}$  represents the stress caused by the increase in dislocation motion of the material up to  $\sigma_p$ .

$$\sigma_{WH} = \sqrt{(\sigma_{sat}^2 - (\sigma_{sat}^2 - \sigma_0^2) \exp(-r\epsilon))} \quad (3.3.6)$$

Where  $\sigma_{WH}$  is derived from the saturation stress  $\sigma_{sat}$ , which is the first stage in which flow stress increases. Where  $r$  is the dynamic recovery coefficient that decreases as the strain rate increases in DIN 18MnCrSiMo6-4 bainitic steel [9], this coefficient has an essential function in this work, as it improves the model accuracy at high strain rates in the hot forging process.

Since these coefficients are obtained by linear fitting from the experimental results already determined by [9], the stress model can be calculated via Eq. 3.3.7. The  $\sigma_{ss}$  represents the stress at a steady-state when complete dynamic recrystallization  $X_{DRX}$  occurs.

$$\sigma_{mod} = \sigma_{WH} - [\sigma_{sat} - \sigma_{ss}] \cdot X_{DRX} \quad (3.3.7)$$

A more detailed description of these hyperbolic constitutive equations and how these results were obtained for this steel can be found in [9].

The mathematical model of the critical strain before reaching a steady-state is presented in the following equation (Eq. 3.3.8) and has been proposed in several previous works [16,18,19] for

C-Mn steels. When the critical strain ( $\varepsilon_c$ ) is exceeded, as described in Eq. 3.3.7, new grains nucleate and grow during the strain step only for  $\bar{\varepsilon} > \varepsilon_c$ .

$$\varepsilon_c = a_2 \cdot \varepsilon_p \quad (3.3.8)$$

In Eq. 3.3.8 and Eq. 3.3.9,  $a_1, a_2, n_1, m_1$ , and  $\varepsilon_p$  are the dependent material parameters and the peak strain, respectively, which is equal to the peak stress  $\sigma_p$  derived from the flow curves.

The activation energy  $Q_1$  ( $\text{J}\cdot\text{mol}^{-1}$ ), gas constant  $R$  ( $\text{J}\cdot\text{mol}^{-1}\cdot\text{K}^{-1}$ ), and the initial grain size  $d_0$  depend on the effective strain rate  $\dot{\varepsilon}$ , and the temperature  $T$ . Thereby, Eq. 3.3.8, Eq. 3.3.9, and Eq. 3.3.10 describe the overall kinetics of dynamic recrystallization  $X_{DRX}$ .

$$\varepsilon_p = a_1 \cdot d_0^{n_1} \cdot \dot{\varepsilon}^{m_1} \cdot \exp\left(\frac{Q_1}{RT}\right) \quad (3.3.9)$$

$$X_{DRX} = 1 - \exp\left(\beta_d \cdot \left(\frac{\varepsilon - \varepsilon_p \cdot a_{10}}{\bar{\varepsilon}_{0.5}}\right)^{k_d}\right) \quad (3.3.10)$$

In Eq. 3.3.10, the exponent ( $\beta_d$ ) represents the Avrami coefficient which is sensitive to variations in temperature. The Avrami exponent ( $k_d$ ) is determined by polymorphic changes, discontinuous precipitation, and interfacial growth control, among other factors [18,19]. The  $\bar{\varepsilon}_{0.5}$  described in Eq. 3.3.11 is the strain when 50% of the recrystallized fraction is reached, where  $a_5, h_5, m_5$ , and  $n_5$  are material parameters.

$$\bar{\varepsilon}_{0.5} = a_5 d_0^{h_5} \dot{\varepsilon}^{m_5} \varepsilon^{n_5} \exp\left(\frac{Q_5}{RT}\right) + C_5 \quad (3.3.11)$$

Finally, Eq. 3.3.12 and Eq. 3.3.13 provide the recrystallized grain size  $D_{DRX}$  after full  $X_{DRX}$  and the average grain size  $D_{AVG}$ , respectively.

$$D_{DRX} = a_8 d_0^{h_8} \dot{\varepsilon}^{m_8} \varepsilon^{n_8} \exp\left(\frac{Q_8}{RT}\right) \quad (3.3.12)$$

$$D_{AVG} = X_{DRX} D_{DRX} + (1 - X_{DRX}) d_0 \quad (3.3.13)$$

If, after the interruption of deformation, the cumulative strain during the industrial forging process is higher than the critical strain ( $\varepsilon_c$ ) then metadynamic recrystallization occurs [18]. In  $M_{DRX}$ , new nuclei appear during forming, but grain growth occurs after the onset of plastic strain. Eq. 3.3.14 and Eq. 3.3.15 describe the kinetics:

$$X_{MDRX} = 1 - \exp\left(\beta_m \cdot \left(\frac{t}{t_{0.5}}\right)^{k_m}\right) \quad (3.3.14)$$

$$t_{0.5} = a_4 \bar{\varepsilon}^{n_4} d_0^{h_4} \dot{\varepsilon}^{m_4} \exp\left(\frac{Q_4}{RT}\right) \quad (3.3.15)$$

Where  $t_{0.5}$  is the time required for 50% metadynamic recrystallization, which is dependent on the effective strain  $\bar{\varepsilon}^{n_4}$ , initial grain size  $d_0^{h_4}$  and strain rate  $\dot{\varepsilon}^{m_4}$  exponents. Eq.3.3.16 describes the grain size diameter for a complete metadynamic recrystallization after plastic strain:

$$D_{MDRX} = a_7 \bar{\varepsilon}^{h_7} d_0^{h_7} \dot{\varepsilon}^{m_7} \exp\left(\frac{Q_7}{RT}\right) \quad (3.3.16)$$

Static recrystallization, described in Eq.3.3.17, occurs when the cumulative strain is lower than the critical strain ( $\varepsilon_c$ ). During this phenomenon, nuclei of recrystallized grains appear and grow after the forging step. The equation is given by:

$$X_{SRX} = 1 - \exp\left(\beta_s \left(\frac{t}{t_{0.5}}\right)^{k_s}\right) \quad (3.3.17)$$

Where  $t_{0.5}$ , Eq.3.3.18 is:

$$t_{0.5} = a_3 \bar{\epsilon}^{n_3} d_0^{h_3} \dot{\epsilon}^{m_3} \exp\left(\frac{Q_3}{RT}\right) \quad (3.3.18)$$

Grain growth for a full  $S_{RX}$  is given in Eq. 3.3.19:

$$D_s = a_6 \bar{\epsilon}^{n_6} d_0^{h_6} \dot{\epsilon}^{m_6} \exp\left(\frac{Q_6}{RT}\right) + C \quad (3.3.19)$$

After full dynamic, static and metadynamic recrystallization, equiaxed grains may coarsen due to grain growth, as described in Eq. 3.3.20, which is considered temperature-dependent.

$$d_f^{m(T)} = d_{0drx}^{m(T)} + a_9 \exp\left(-\frac{Q_9}{RT}\right) \cdot t \quad (3.3.20)$$

Here,  $d_0$  is the full-recrystallized grain size,  $t$  is the time after complete recrystallization,  $Q_9$  is the apparent activation energy, and  $m$  and  $a_9$  are the material and process-dependent constants.

### 3.3.2.5 Forging Trial and Numerical Modeling

The industrial closed die forging tests were performed using a friction press with an energy of 240 kJ. Table 3.3.2 shows the forging conditions and targets used in this work. A cylindrical billet was forged at two different temperature conditions. The thermomechanical route and a forged specimen are shown schematically in Fig. 3.3.3.

**Table 3.3.2.** Processing conditions in the industrial forging experiments.

Forging type	Initial geometry (mm)	Temperature (°C)/Induction coil power (kW)	Forming speed (mm/s)	Cooling program	Cooling rate (°C/s)	Revealing type
Closed die	54 x 38	1030, 32.9	1645	Water quenching	~ 45	Austenite grain boundaries
		1130, 40.6		Continuous cooling	~ 0.7, 0.65	bainite, ferrite, martensite

After forging, two dwell times, which represent the interval before quenching, were estimated with the aid of recorded videos. The first dwell time represents the interval where the lower and upper dies touch, 2 seconds. The second dwell time represents the interval in which the upper die was lifted, allowing the workpiece to be manipulated/moved. The workpiece was then quenched with moderate agitation at a water temperature of 23 °C.

After the first methodology was used for forging and quenching, other samples were forged and cooled to room temperature (25 °C) in calm air. Three representative sample regions were analyzed to determine the average grain size after hot forging. Prior austenitic grain size (PAGS) after quenching with water was revealed using a 3% picric acid solution and quantified by optical microscopy at 500x magnification. The circular intercept method was used for grain size determination of the hot-forged samples according to the ASTM E112 standard.

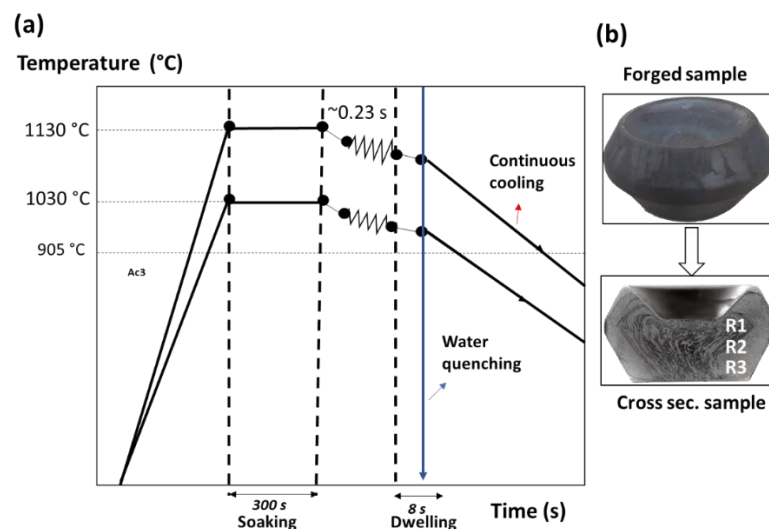


**Figure 3.3.3.** (a) Thermomechanical routes on industrial environment steps, (b) Experiment forged samples indicating the regions of metallography analysis.

The evolution of the grain size of steels by induction coil heating at 1030 °C and 1130 °C after 300 seconds was studied in annealing tests, which gave values of 26  $\mu\text{m}$  for 1030 °C and 54  $\mu\text{m}$  for 1130 °C. After removing the samples from the induction furnace, the surface temperature was measured using a Fluke®, Ti - 400 thermal camera. The forging temperatures in this work were chosen to be 1030 °C and 1130 °C based on the results of [8] to avoid abnormal austenitic grain growth.

The coupled simulation of heat transfer and microstructure evolution was performed using a rigid-viscoelastic code in DEFORM® V.11.0. The multi-operation code was used to represent the industrial conditions in the numerical simulation. Fig. 3.3.4 shows the proposed forging model corresponding to the industrial conditions and the tracked points representing the average grain size of twelve points in the measured regions (R1, R2, and R3).

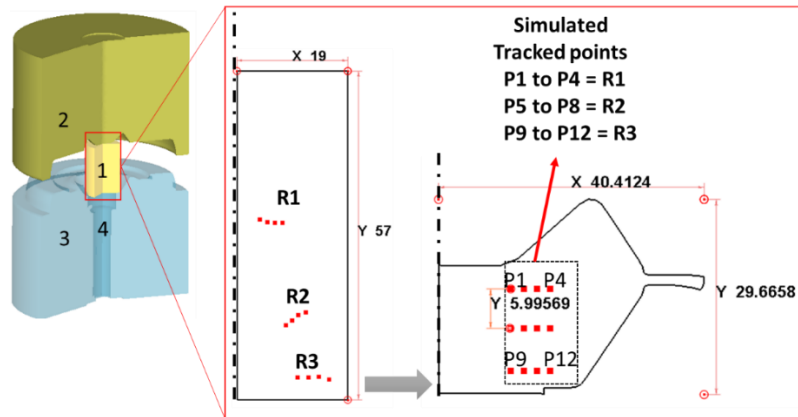


**Figure 3.3.4.** The axisymmetric model implemented in DEFORM for gear forging and a cross-section of the simulated forging profile of the preform showing the analyzed areas. 1 - Billet, 2 - Upper die, 3- Lower die, 4 - Knock-off.

Hexahedral elements were used to discretize the components using a coupled thermomechanical process. Elasto-plastic bodies were considered in the upper, lower, and knock-off dies, with 250 °C as the initial temperature in the forming dies. Since high plastic strains lead to severe mesh distortion, the automatic remeshing technique was used. This method solves problems related to the inability to model geometry and state variables [19].

The boundary conditions of the process are listed in [Table 3.3.3](#), according to the industrial environment and the steel properties. The thermal conductivity and heat capacity were taken from Castro and co-workers' inverse heat transfer analysis for this steel [20]. The friction factor  $\mu$  was set at 0.3, corresponding to the use of graphite and water in the closed die hot forging condition [14].

**Table 3.3.3.** Thermal properties in the numerical model.

Item	Value
Density (g/cm <sup>3</sup> )	7.83
Heat transfer with pressure considering scale field (N/sec/mm/°C)	11
Air convection coefficient (N/sec/mm/°C)	0.01
Quenching convection coefficient (N/sec/mm/°C)	11

### 3.3.2.6 Strength and Toughness Analysis

This study performed tensile testing of the miniature specimen to determine strength in specific forged areas, as shown in [Fig. 3.3.5](#). A hydraulic testing machine MTS 810 250 kN with a laser strain gage, was used to perform the tests. For each analyzed region, seven (7) samples were prepared for testing to achieve good repeatability of the experiments. The samples were produced by wire EDM, as suggested by [21], using the standards DIN EN 2002:2006, DIN EN ISO 6892-:2009-12, and DIN 50100.

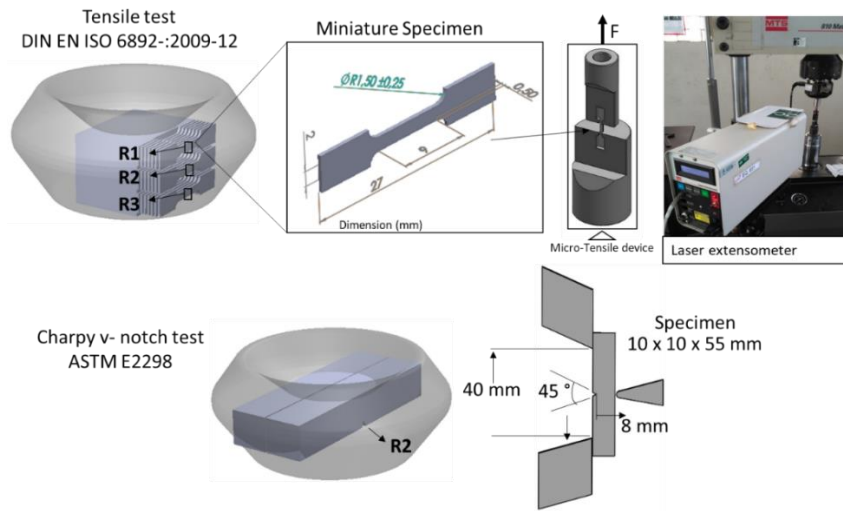


**Figure 3.3.5.** Representative and machined zone of collected samples for the miniature tensile test specimen and Charpy V-notch.

Four specimens were taken from two forged test pieces for each temperature proposed in this study to determine the bar impact energy by the Charpy notched bar impact test. The specimens were tested at a room temperature of 23.5 °C in a standard atmosphere in both tests. The specimens were processed following ASTM E2298.

### 3.3.3 Results and Discussion

#### 3.3.3.1 Grain Growth Model of Annealing

Fig. 3.3.6a and Fig. 3.3.6b show a parallel trend in grain growth with increasing time and temperature. Linear regression was used to estimate the mean values of the coefficients  $m$ ,  $a_0$ , and  $Q_0$  given in Eq. 3.3.21.

From these data fitting, Fig. 3.3.6c shows the results of the isothermal numerical simulation of austenitic grain growth compared to the experiments performed by [8]. In the current study, it was necessary to consider a homogeneous grain size distribution to find a reasonable agreement between the experiment and predicted results.

$$d = d_0^{5,25} + 4.56 \cdot 10^{16} t \exp\left(-\frac{299500}{RT}\right)^{0.1904} \quad (3.3.21)$$

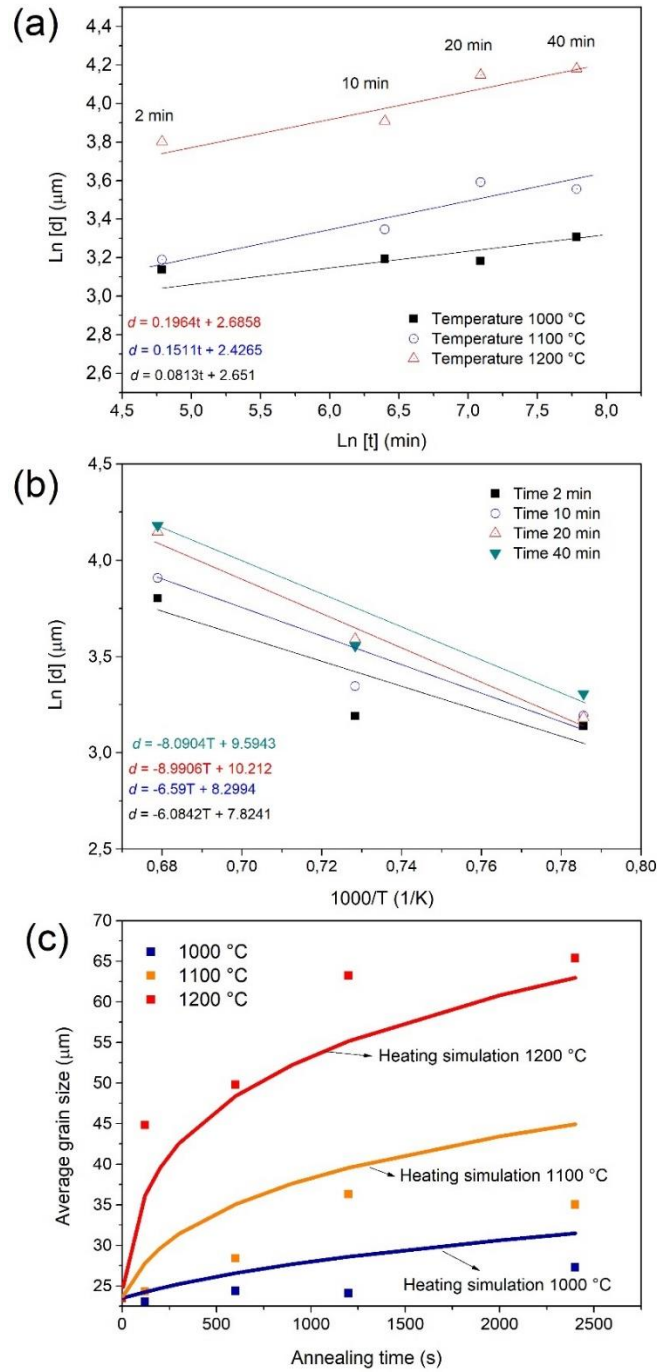


**Figure 3.3.6.** Modeled Annealing curves for 18MnCrSiMo6-4 steel; (a) Natural logarithm of grain size and time, (b) Grain size and inverse of temperature, (c) Comparison between experiment and simulation grain growth evolution.

Fig. 3.3.6c also shows that grain growth exhibits exponential behavior, with final size strongly affected by temperature after a short time. At a specific annealing time, say 1200 seconds, a variation in grain size deviates from the exponential trend. It is possible that at this point, a change in activation energy occurs, possibly changing the exponent ( $m$ ) in Eq.3.3.1 of grain growth. In particular, this is caused by the dissociation of precipitates that reduce grain growth's boundary motion or coalescence due to Zener pinning [8].

It is well known that carbon diffuses rapidly because of its interstitial characteristics, facilitating dissolution in the austenitic matrix. Therefore, it requires less self-diffusion activation energy. The opposite is true in the presence of substitutional elements such as  $Mn$  and  $Ti$ , which require higher self-diffusion activation energy [22].

The abrupt increase in austenite grain size at 1200 °C is the result of the dissolution of carbides formed by microalloying elements in this steel. These elements are responsible for forming precipitates such as manganese sulfides  $MnS$  and  $TiC$ , which causes pinning effects to be a barrier to grain growth [8]. Molybdenum carbides ( $MoC$ ) may have formed since a small amount (~0.27%  $Mo$ ) is present, affecting grain growth stabilization.

The theoretical implications may suggest that the total grain boundary area, in this case, is higher than the 1200 °C austenitization condition. Therefore, the system's total energy may be higher [22]. In other words, it can be assumed that the activation energy increased.

The value of the activation energy of 18MnCrSiMo6-4 is (299 kJ/mol.K), which is slightly higher than the results calculated by [13] (230.992 kJ/mol.K), which was determined for a steel grade with a higher carbon content of 0.3% C and lower amount of manganese 0.81% Mn. However, after the annealing test, the obtained grain size in this work is smaller than the steel studied by [13] (about 7.8 times lower).

### 3.3.3.2 Model Validation

This work's industrial application model has been based on validating the numerical model of grain growth after the recrystallization kinetics from the compression test. The interactive mode presented in Fig. 3.3.2 determines the coupling of the flow curve and grain size model throughout

the experimental results. Table 3.3.4 displays the overall constants calibrated for the microstructure modeling.

**Table 3.3.4.** Constants used in DEFORM® after calibration of the experiment for microstructural modeling of DIN 18MnCrSiMo6-4 steel.

Constants of Microstructure Evolution							
Critical Strain $\epsilon_c$	Values	$X_{DRX}$ and $D_{DRX}$	Values	$M_{DRX}$ and $D_{MRX}$	Values	$S_{RX}$ and $D_{SR}$	Values
$a_1$	0.00479	$\beta_d$	-0.597	$\beta_m$	0.69417	$\beta_s$	-0.6931
$a_2$	0.54	$k_d$	1.798	$k_m$	2	$k_s$	1
$n_1$	0	$a_5$	0.1129	$a_4$	2.13E-6	$a_3$	2.5E-19
$m_1$	0.1238	$h_5$	0.32	$h_4$	0	$h_3$	0
$Q_1$	44500	$n_5$	0	$n_4$	0	$n_3$	-4.0
		$m_5$	0.03	$m_4$	-0.62	$m_3$	2.0
		$Q_5$	3450	$Q_4$	133000	$Q_3$	270000
		$c_5$	0	$a_7$	1804.6	$a_6$	0.5
		$a_{10}$	0	$h_7$	0.63	$h_6$	0.67
		$a_8$	8103	$n_7$	-0.25	$n_6$	-1
		$h_8$	0	$m_7$	-0.12	$m_6$	0
		$n_8$	0	$C_7$	0	$c_6$	0
		$m_8$	-0.16	$Q_7$	-73778	$Q_6$	0
		$c_8$	0				
		$Q_8$	-74880				

The accuracy of the results of the FEM model can be seen in the flow stress shown in (Fig. 3.3.7a), which shows what would be the flow curves at high strain and strain rate levels ( $100 \text{ s}^{-1}$ ). These curves were converted into time (s) format using the ratio between the strain and strain rate ( $\text{s}^{-1}$ ) [9,10], as shown in Eq. 22. In (Fig. 3.3.7b), the predicted values of recrystallization fraction in different strain rates are shown.

$$t = \left( \frac{\epsilon - \epsilon_c}{\dot{\epsilon}} \right) \quad (3.3.22)$$

With the increase of strain rate at constant T (1150 °C), the  $X_{DRX}$  time decrease [18]. As reported by [10,23], high strain rate increases the migration rate of dislocations and grain boundaries, therefore, accelerating the  $X_{DRX}$  process after the  $\varepsilon_c$  is reached [23].

Fig. 3.3.7c and Fig. 3.3.7d show the predicted results of the experimental punch load of the numerical model during the compression test and FEM recrystallization results, respectively.

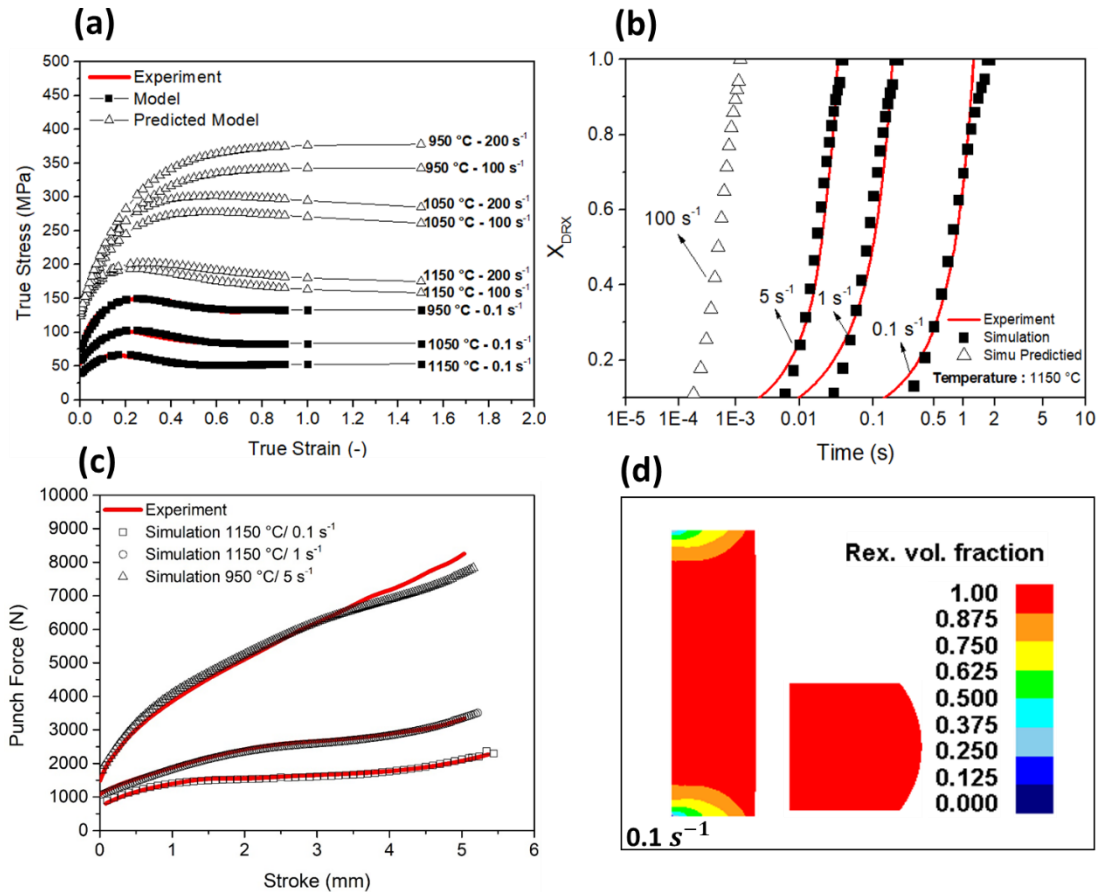


**Figure 3.3.7.** (a) Modeled flow curves and predicted for high strain rates on temperature dependence [9], (b)  $X_{DRX}$  kinetics on strain rate dependence, modeled and predicted, (c) Comparison between experiment and prediction of a load of a compression test, (d) FEM recrystallization results.

A good approximation of the computational simulation results with the force and displacement experiments has been shown, using the model proposed by [9] for a continuous cooling bainitic steel. A slight variation of the experimental forces compared to the simulation can be seen at the

temperature and strain rate of 950 °C and 5 s<sup>-1</sup>, respectively. It is assumed that this condition is more prone to adiabatic heating variation for the calculated model when compared to the phenomena occurring during the experiment. The chemical interactions and the activation energy vary with the degree of plastic strain and strain rate. Therefore, this can sensitively vary the force and displacement results. Moreover, friction was kept constant during the computer simulation, not depicting the natural behavior during the hot forging process. A dynamic friction coefficient could be preferred to solve this issue.

Fig. 3.3.8 shows the cross-section view of the experimentally measured and numerically calculated fully recrystallized austenitic microstructure after being compressed at 950 °C (Fig. 3.3.8a) and 1150 °C (Fig. 3.3.8b), respectively. Three points on the specimens were measured and compared to the simulation. What stands out in this figure is that small nucleate recrystallized grains can be observed at different temperatures, with grains being more refined at 950 °C.

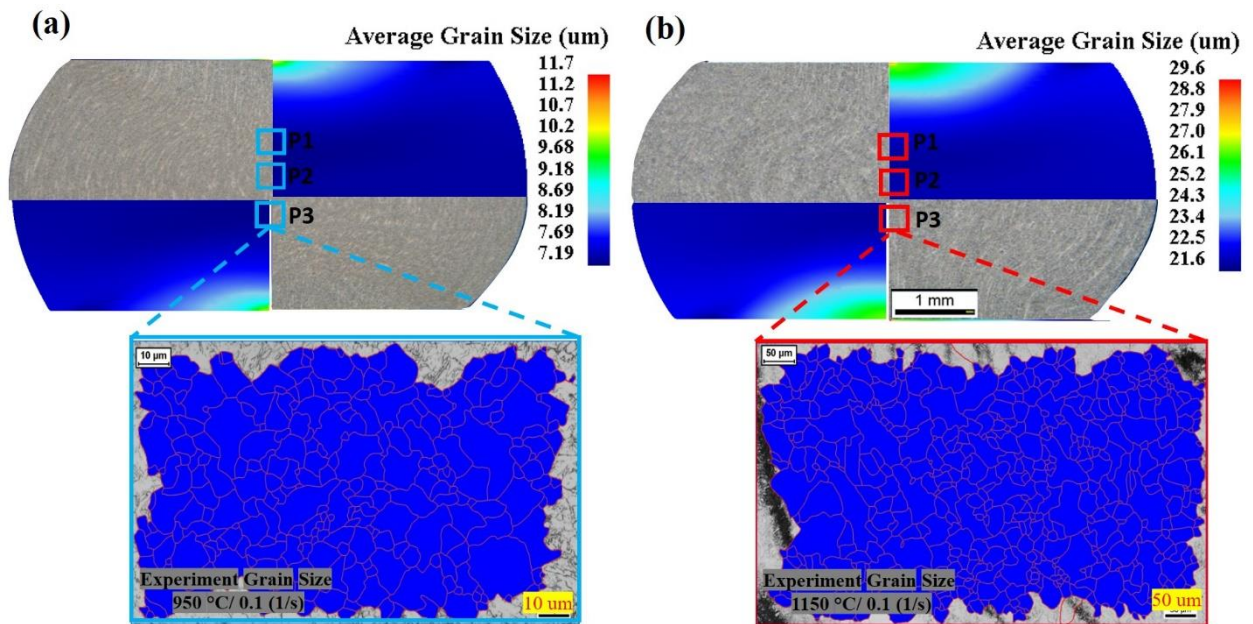


**Figure 3.3.8.** Simulation of austenitic grain size in isothermal compression test (a) 950 °C 0.1 (1/s), (b) 1150 °C 1150 °C 0.1 (1/s).

Fig. 3.3.9 illustrates the experimental and simulated austenitic grain size variation at different temperatures and strain rates. The most interesting aspect of this graph is that not only the temperature influenced the austenitic grain refinement, but also the strain rate. The values show

that increasing the strain rate by 10 times at 1150 °C caused a higher variation in grain size is seen compared to 950 °C. The variation was of 40.74% at a constant temperature of 1150 °C. Comparing the temperature from 1150 °C to 950 °C, a percentage variation of 82.87% in grain size refinement was obtained. However, at 950 °C, the strain rate did not influence the grain refinement considerably. This can be related to a decrease in driving force where the temperature dominates the recrystallization mechanism activation [9,15].

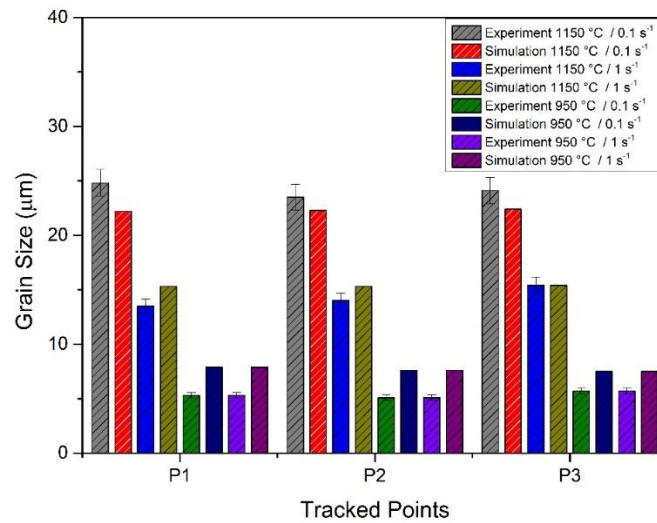


**Figure 3.3.9.** Predicted austenitic grain size of hot compressed samples  $\varepsilon = 0.69$ .

The EBSD map in Fig. 3.3.10 shows these results in the crystallographic unit sizes (UC) of quenched samples, and Fig. 3.3.11 shows a histogram of the UC. Smaller crystallographic units were seen in the sample compressed at 950 °C (Fig. 3.3.10a) than in the samples at 1150 °C (Fig. 3.3.10b). At 950 °C, less UC size distribution was observed, as shown in (Fig. 3.3.11a) in comparison to the higher forming temperatures (Fig. 3.3.11b), which showed a more extensive UC distribution. Also, a morphological variation, where more granular packages were seen at lower temperatures whereas, at higher temperatures, large packages with laths were observed.

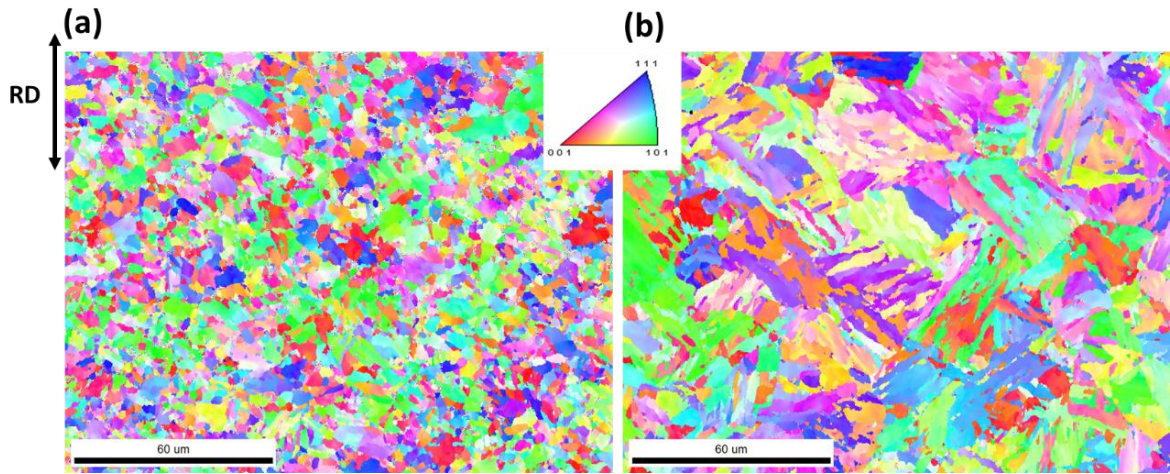


**Figure 3.3.10.** EBSD map showing the temperature dependence in different sizes of crystallographic units. (a) P3 -  $T = 950\text{ }^{\circ}\text{C} / \dot{\epsilon} = 0.1\text{ s}^{-1}$ , (b) P3 -  $T = 1150\text{ }^{\circ}\text{C} / \dot{\epsilon} = 0.1\text{ s}^{-1}$ .

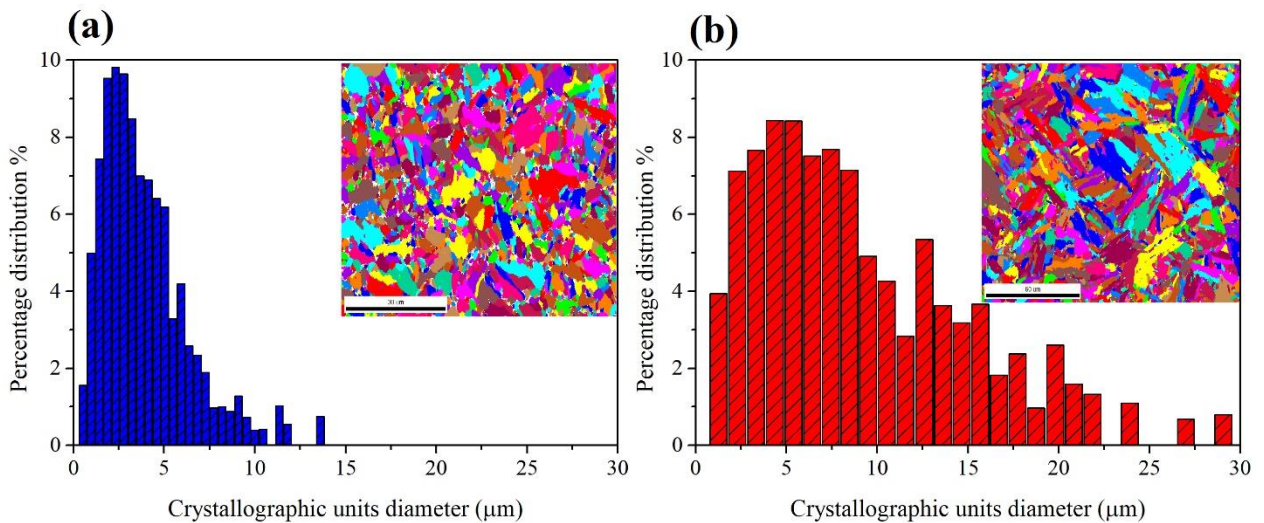


**Figure 3.3.11.** Histogram of measured crystallographic units grain sizes, (a)  $T = 950\text{ }^{\circ}\text{C} / \dot{\epsilon} = 0.1\text{ s}^{-1}$ , (b)  $T = 1150\text{ }^{\circ}\text{C} / \dot{\epsilon} = 0.1\text{ s}^{-1}$ .

It is assumed that the smaller austenitic grain sizes were responsible for the smaller crystallographic UC. This will contribute to the increase in high-angle grain boundaries (HAGB), which, according to the literature [23], improves the material's toughness and strength.

### 3.3.4 Industrial Application

#### 3.3.4.1 Microstructure Simulation in the bainitic steel

A point-tracked section of DIN 18MnCrSiMo6-4 helical gear was analyzed in the simulation results. The average temperature of the tracked points displayed in (Fig. 3.3.4), representing each analyzed region (R1, R2, and R3) in the simulation, is shown in Fig. 3.3.12.

The temperature rises due to the energy dissipation in the form of heat (adiabatic heating) caused by strain rate and plastic strain, showed in (Fig. 3.3.13a) and (Fig. 3.3.13b). The simulation results show that the energy dissipation is higher during forging with the initial temperature of 1030 °C than 1130 °C due to mechanical energy available to be converted into heat being higher in lower temperatures. There was an increase of 50 °C from the temperature of 1030 °C and 30 °C at the temperature of 1130 °C.

The conduction between the workpiece and dies provokes a decrease in temperature on both surfaces, which is more pronounced for the lower die, as shown after a dwelling of 2.023 seconds. Moreover, the heat flux from region R3 in direction to region R2 and R2 to R1 maintains R2's temperature constant for a longer time and, therefore, causes an increase in the austenitic grain size by grain coarsening. This behavior is shown in (Fig. 3.3.12a) for forging at 1030 °C and (Fig. 3.3.12b) for forging at 1130 °C.

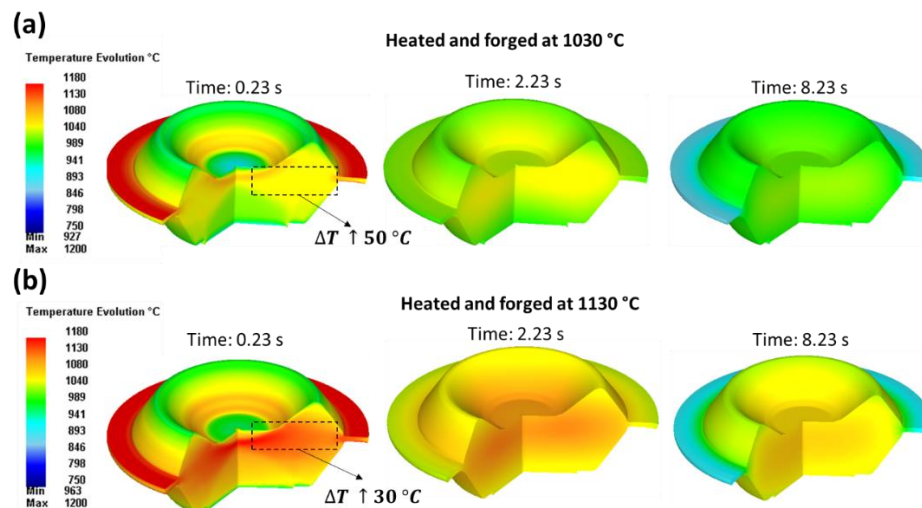


**Figure 12.** Temperature evolution of forging and cooling simulation in the forged preform; (a) Austenitization at 1030 °C; (b) Austenitization at 1130 °C.

Lower temperatures also increase the force required for the plastic flow to occur and, therefore, the system's energy [19]. Even with the increase in energy dissipation in higher strain rates, forging at lower temperatures (1030 °C) does not exceed the value of 1100 °C-in this way, avoiding the excessive grain coarsening.

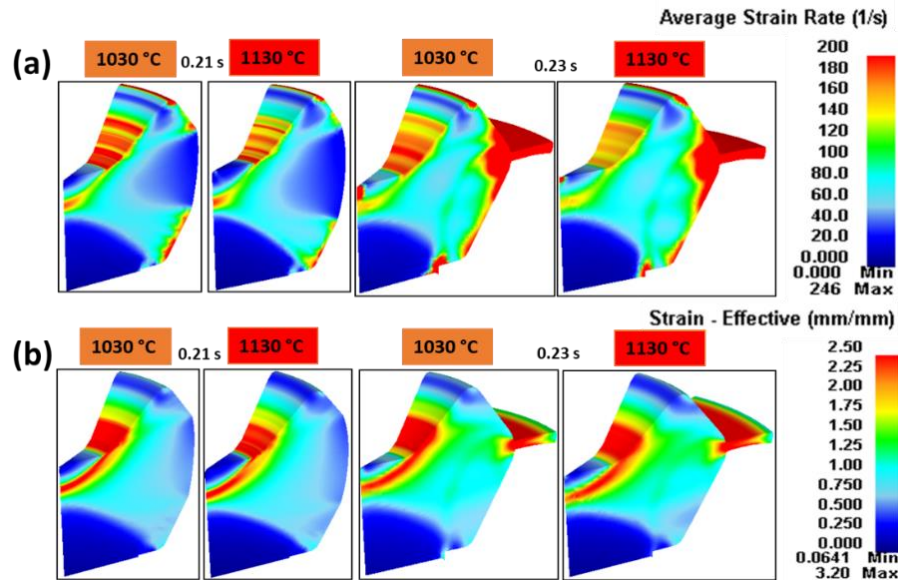


**Figure 3.3.12.** Simulated evolution of (a) average strain rate ( $\dot{\epsilon}$ ) and (b) effective strain ( $\bar{\epsilon}$ ) on the industrial preform forged gear.

Although these behaviors are expected, it is only through FEM that it can accurately quantify the local distribution of strain throughout the billet, allowing evaluation of mechanical properties after the tensile and impact tests. The numerical simulation showed a significant difference between the effective strain rate fields in the R2 region and R3 caused by the upper die piercing in the billet, changing the plastic flow rate.

Even though the increase in strain rate should reduce the recrystallization fraction due to the increase in critical strain for  $X_{DRX}$  [16], we must take into account the adiabatic heating in high-speed closed die forging, which interacts in two ways: First, through the heterogeneous plastic strain, which was higher in R1 than in R2 and R3, and second, through the heterogeneous strain rate, which changes the parameter ( $Z$ ) responsible for the magnitude of  $D_{DRX}$ . Thus, the simultaneous increase in plastic strain and strain rate in R1 resulted in a higher  $X_{DRX}$  fraction due to the temperature increase, which delayed the time of grain growth by increasing the dynamically recrystallized grains  $D_{DRX}$ .

Different mechanisms such as  $X_{DRX}$ ,  $M_{DRX}$ , and  $S_{RX}$  can be qualitatively analyzed through FEM by the JMAK macro-scale model results. Fig. 3.3.14 provides the results obtained from the numerical simulation of these phenomena, and Fig. 3.3.15 shows the grain size evolution. According to these results, when ( $\bar{\epsilon} > \epsilon_c$ ), there is a predominance of  $X_{DRX}$  (Fig. 3.3.14a), which is proportional to the plastic strain in each selected region.

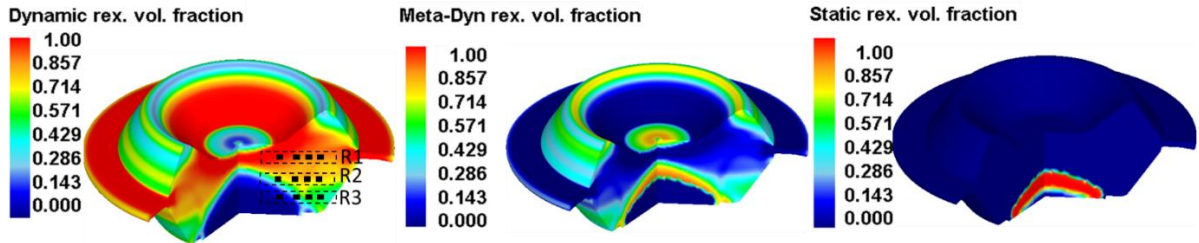


**Figure 3.3.13.** Recrystallization kinetics of the modeled pre-form hot forged; (a)  $X_{DRX}$ ; (b)  $M_{DRX}$ ; (c)  $S_{RX}$ .

Nonetheless, compared to the analyzed regions R1, R2 and R3, the strain rate may also be responsible for the lower  $X_{DRX}$  values found in R2 and R3. It is well known that strain rate affects the dynamic recrystallization kinetics due to the increase in dislocation density [16]. Higher strain rates may decrease the mobility of these dislocations in R2 and R3, which consequently reduces annihilation or rearrangement. In contrast, in the R1 region, which may increase mobility due to higher temperature, over 95% of complete recrystallization was achieved.

The regions that were submitted to minor plastic strain and lower than critical strain  $\epsilon_c$  was recrystallized Metadynamically ( $M_{DRX}$ ) and statically ( $S_{RX}$ ), respectively, as shown in Fig. 3.3.14b and Fig. 3.3.14c. An apparent phenomenon is that the  $M_{DRX}$  is slower than the  $DRX$ 's kinetics and is observed in R1. Therefore, the significant difference between each recrystallization phenomenon is that the final nucleated grain size may be larger than the  $X_{DRX}$  at the same deformation time as holding. The main reason for this phenomenon is the lack of dislocation multiplication during the  $M_{DRX}$  process [26].

In the case of closed-die forging, such a mechanism could be compensated by the temperature rise caused by the stored energy due to the plastic strain, strain rate, and the heat dissipation itself. The higher forging temperature (1130 °C) and strain rate may provide more thermal energy for grain boundary migration [27]. In R2, the temperature was higher than in R1

after 8.23 s, shown in Fig. 3.3.12b, and therefore more thermally activated for the grain growth mechanism (Fig. 3.3.15b).

### 3.3.4.2 Grain Growth Simulation after Hot Forging

Based on the results in Fig. 10 and the discussion in the previous section, we have considered the grain growth exponent  $m$  (Eq. 3.3.20) as a variable, which depends on the grain size distribution [18], plastic deformation degree, and temperatures.

Hodgson and Gibbs [28] also stated that high values of  $m$  are strongly dependent on annealing temperatures and a weak function of the initial recrystallized grain size and holding time. However, in the case of short holding times in closed die forging, the exerted heterogeneous plastic strain distribution, strain rate, and adiabatic heating result in different grain size distribution and recrystallization mechanisms (Fig. 3.3.11, Fig. 3.3.12, Fig. 3.3.13, and Fig. 3.3.14). Therefore, a constant value of the growth exponent is not sufficient to predict the austenite grain growth. Such consideration about this behavior can also be associated with the high-temperature peak condition caused by the adiabatic heating, in which all fine precipitates are dissolved [29].

To distinguish between these parameters with Hillert's theory for ideal growth mechanism [30], we assumed that above 1100 °C, exponent  $m > 4$  represents the increase of the growth rate, while  $m$  between 3-4 would represent a decrease in growth rate. This makes the magnitude of the collision factor of the atoms decrease in terms of the reactions based on Arrhenius's theory. The modified empirical grain growth exponent values are shown in Table 3.3.5.

**Table 3.3.5.** Values of  $m$  exponent implemented in DEFORM®, computed as a temperature function in non-isothermal condition after  $D_{RX}$ ,  $M_{DRX}$  and  $S_{RX}$ .

Temperature °C	$m$ -value	$1/m$
1200	5.3	0.1886
1160	4.9	0.2040
1150	4.2	0.2380
1100	3.8	0.2631
1030	3.3	0.3033
1000	3.3	0.3033

As shown in Fig. 3.3.15, in the first 2 seconds, most of the heat transfer is between the billet's surface and the lower and upper dies. The pressure of the mechanical system also raises, increasing the temperature in regions R1 and R2 and, therefore, may increase the growth rate for temperatures above 1100 °C.

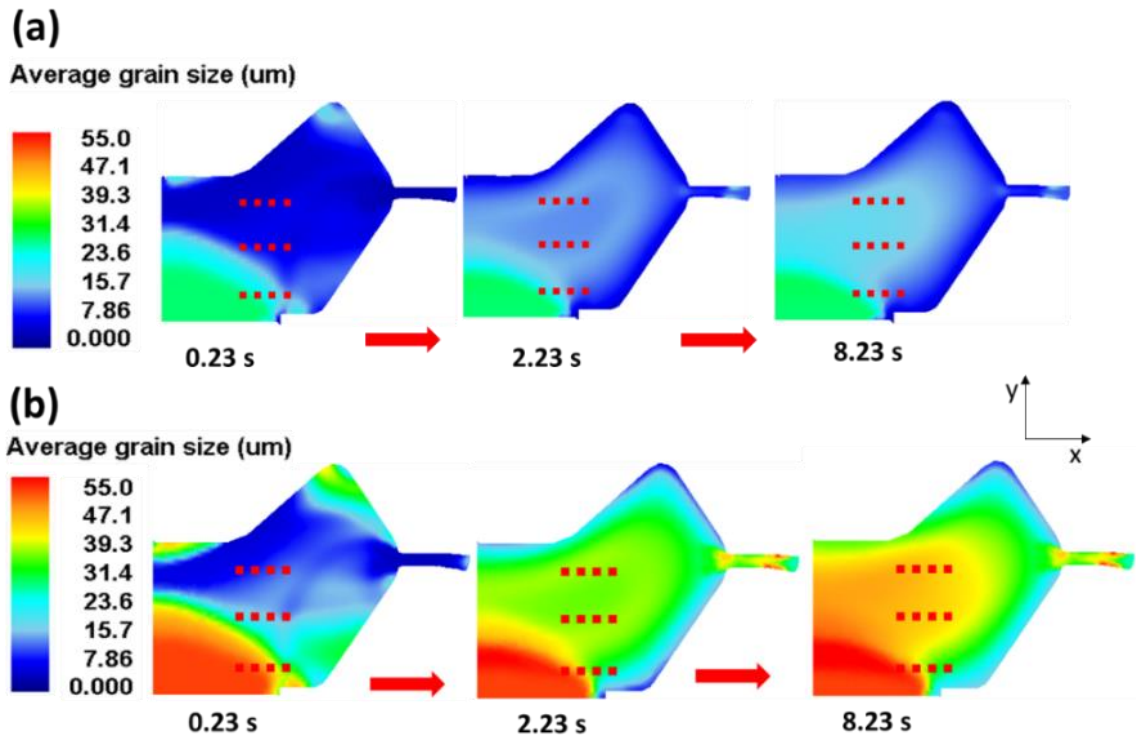


**Figure 3.3.14.** X-Y Plane view of the grain size evolution computed on the tracked points: (a) Forged at 1030 °C, (b) Forged at 1130 °C.

Fig. 3.3.16 shows the comparison of the predicted results of the grain size with  $m$  as a constant value, and  $m$  in function of the temperature in the different regions for this proposed study. The modification of the growth exponent as a temperature function demonstrated an improvement of model in comparison of constant  $m$  exponent, being closer to experiment results. The temperature had the main influence on the austenitic grain size variation when comparing both cases. However, for the forging done at 1130 °C, the local strain also exerted a major influence on the grain size variation.

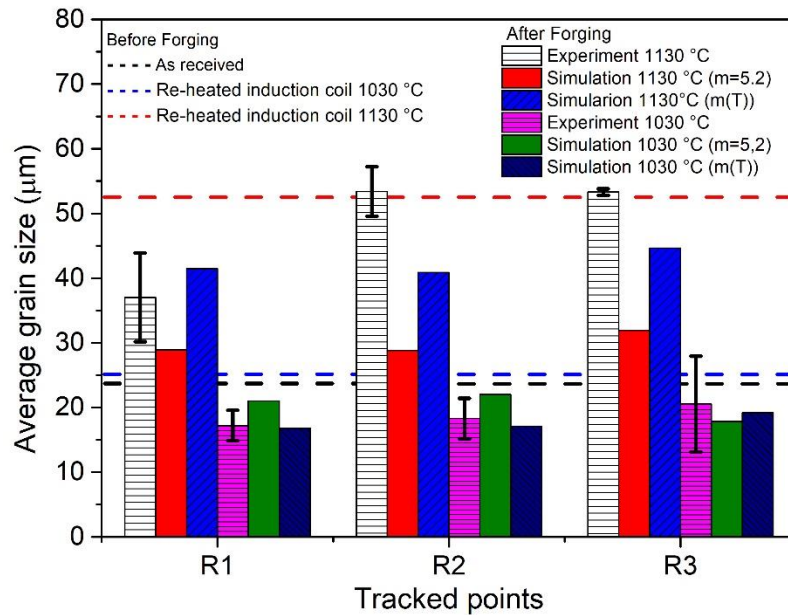


**Figure 3.3.15.** Local austenitic grain size comparison after industrial hot forging between experiment and numerical simulation results.

Silveira and co-workers [8] showed that in a hot forging experiment above 1100 °C at a low strain rate of about  $0.17 \text{ s}^{-1}$ , the austenitic grain size remained large due to the extended periods the continuous cooling required. In contrast, this work employed high strain rates reaching up to  $50 \text{ s}^{-1}$  showing the influence of this parameter when combined with high plastic strain, which resulted in grain refinement when forging above 1100 °C due to adiabatic heating. This can be seen by comparing the R1 and R3 regions. The increase in the strain rate delays the onset of dynamic recrystallization kinetics. i.e., the critical strain  $\varepsilon_c$  is the trigger for this reaction; therefore, this variation can be explained by the local strain rate gradient.

### 3.3.4.3 Mechanical Properties response

Experimental results of austenitic grain size were used to validate the accuracy of the numerical simulation. It is important to remind that in this present study, the bainitic phase transformation was not modeled, thus only the grain size model during hot forging and their influence on mechanical properties is addressed.

Fig. 3.3.17 shows the experimental grain size in the R2 region and the final microstructure after quenching of the forged part at temperatures of 1030 °C (Fig. 3.3.17a) and 1130 °C (Fig.

3.3.17b), respectively. As can be seen, more refined austenitic grain forms when forged at 1030 °C, which shows the importance of controlling the forging temperature of this steel. As already mentioned, the temperature variation was influenced due to the mobility of the dislocations, which likely decreased the growth rate of the dynamically recrystallized grains. This grain size variation resulted in different bainitic morphologies in the microstructure after continuous air cooling, as can be seen at lower magnification in Fig. 3.3.17b, and Fig. 3.3.17e forged at 1030 °C and 1130 °C, respectively. Visually, it is possible to observe a considerable amount of polygonal ferrite PF in the 1030 °C (Fig. 3.3.17c), when compared to 1130 °C (Fig. 3.3.17f), which showed less PF fraction in this region and more Lath-like bainite LB.

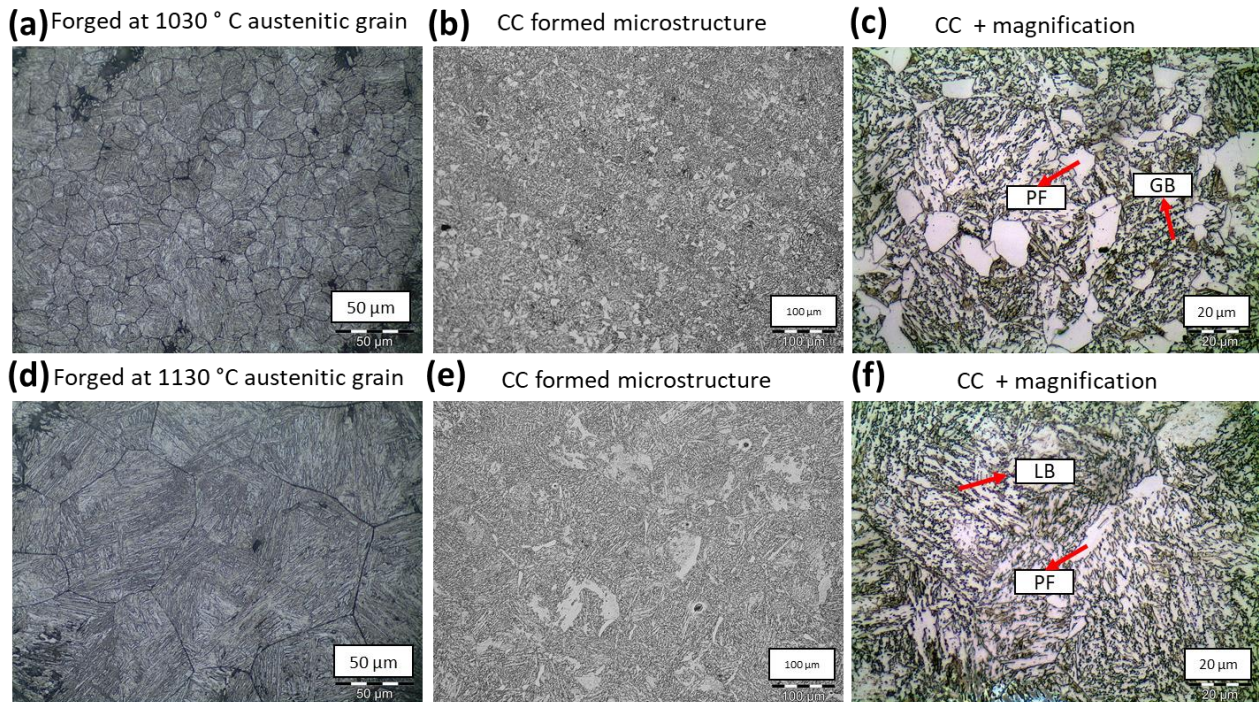


**Figure 3.3.16.** Austenitic grain and continuously cooled microstructure in R2 region: (a,b) and (c) Forged at 1030 °C, quenched and cooled in calm air; (d,e) and (f) forged at 1130 °C quenched and cooled in calm air.

Austenitic grain refinement increases the amount of ferrite nucleation sites due to the increase in the grain boundary area. The increase in the dislocation density caused by plastic deformation, as well as the strain rate, are responsible for more retained austenite in the microstructure, as

reported by [8,29]. The increase of defects caused by plastic strain, increases the number of possible nucleation sites due to the growth of A3 austenite-ferrite transformation [8].

Even at high strain rates, the metallurgical evolution of the ferritic bainite transformation was the same as reported by [6,7,8]. The temperature significantly influenced the transformations. By forging at 1130 °C a larger fraction of the granular GB bainite can be observed, as well as lath-like LB bainite.

Finally, the mechanical properties are analyzed. Fig. 3.3.18a shows the boxplot of the yield YS and Fig. 3.3.18b the tensile strength US results from the micro tensile tests for the three selected regions of the industrial hot forged component. Fig. 3.3.19a shows the toughness response of the material to the Charpy impact tests whereas the elongation (EL) is shown in Fig.3.3.18b.

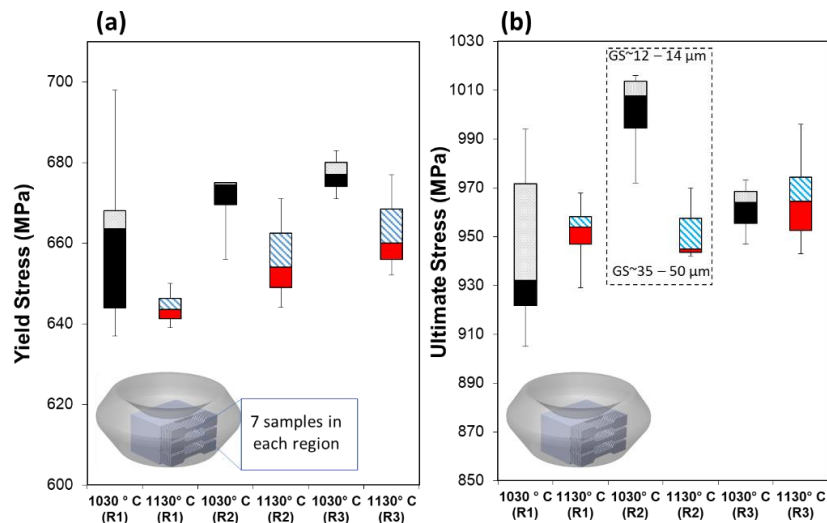


**Figure 3.3. 17.** Boxplot results of the (a) Yield stress YS and (b) Ultimate stress US in MPa.

The results suggest that the forging temperature was mainly responsible for the increase in the YS (Fig. 3.3.18a) and US (Fig. 3.3.18b), where the calculated average stress ratios ( $YS_{avg}/US_{avg}$ ) were 0.70 at 1030 °C and 0.68 at 1130 °C. However, by taking the R2 region into account, the plastic strain rate at low temperature also exerted a considerable effect on the YS and TS. This result can be explained through the numerical simulation, which showed that, by the time of forging unloading, the energy accumulated in the R1 region was greater than R2, which accelerated grain growth due to adiabatic heating, as shown in Fig. 3.3.12 and Fig. 3.3.15, respectively.

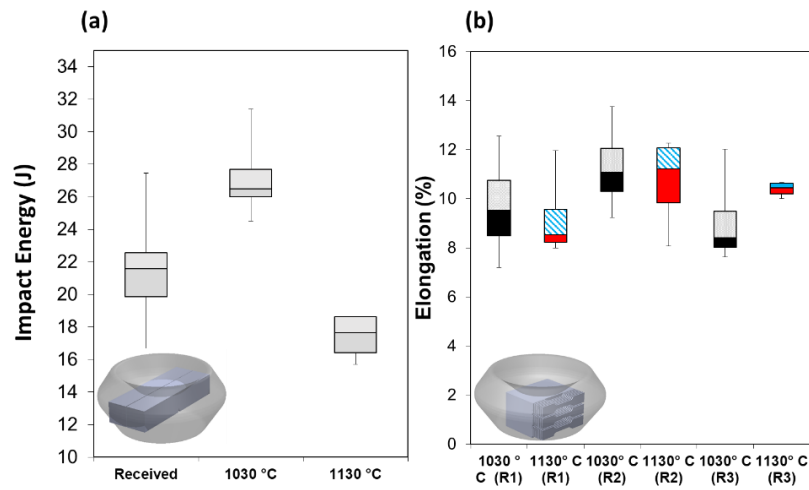


**Figure 3.3.18.** (a) Impact energy through of Charpy- V notch tests; (b) Local Elongation in %.

Fig. 3.3.20 shows the microstructure from the micro-tensile samples in a magnified scale. It can be seen the different bainitic morphology revealed by scanning electron microscopy (SEM) in the three regions.

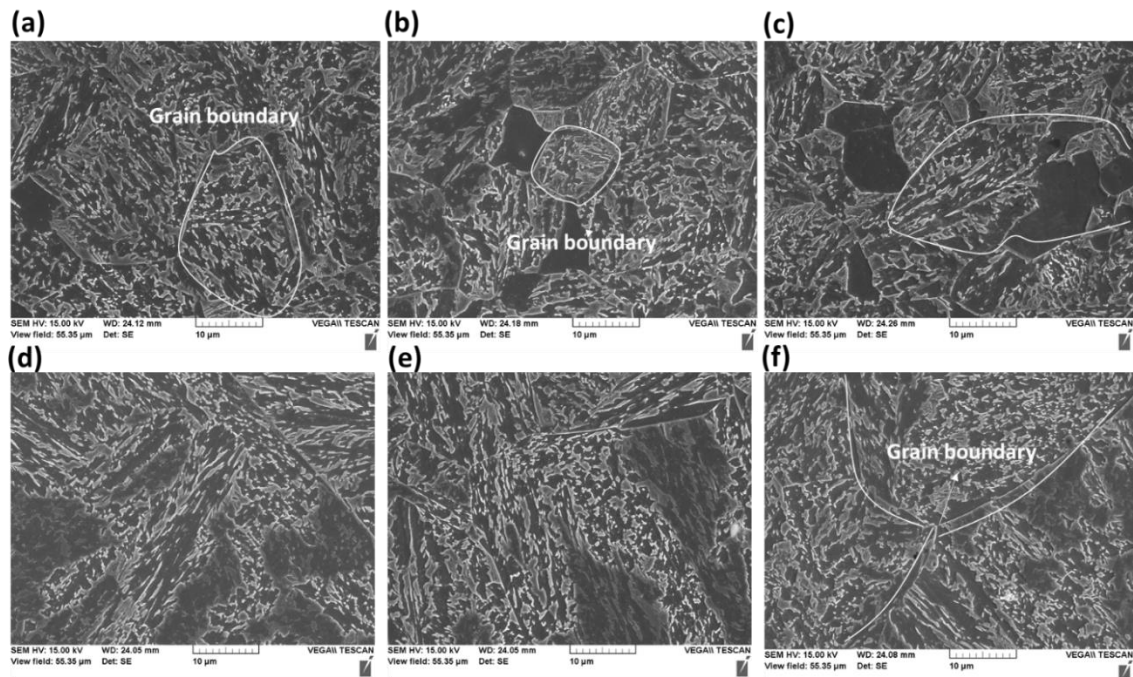


**Figure 3.3.19.** SEM results of the micro-tensile specimen regions showing the final continuous cooled microstructure of pre-form gear. (a) R1, (b) R2 and (c) R3 Forged at 1030 °C; (d) R1, (e) R2 and (f) R3 Forged at 1130 °C, respectively.

The physical simulations performed by [6,7] with controlled temperature in continuous cooling rate and low strain rate [8] has shown a similar bainitic structure [6,7,8]. However, in this work, it has shown the influence of the temperature variation in high strain rate the microstructure evolution in the industrial hot forged condition. Fig. 3.3.20a (R1), Fig. 3.3.20b (R2) and Fig. 3.3.20c (R3) forged at 1030 °C, revealed different sizes of grain boundaries compared to the samples forged at 1130 °C (Fig. 3.3.20d, Fig. 3.3.20e and Fig. 3.3.20f). The aid by finite element analysis showed for each region of both hot forged conditions, the located temperature, plastic strain, and strain rate variation, as consequence of the new recrystallized grains. The temperature variation due to the energy dissipation through plastic strain and strain rate has possibility made the austenite grains in R1 and R2 smaller than R3. At 1030 °C, the grains have more homogeneity and refined in comparison of the 1130 °C forged temperature.

The toughness of the component forged at 1030 °C increased compared to the material as received and forged at 1130 °C. This result is shown in Fig. 3.3.19a and confirms that the decrease in crystallographic unity (UC), previously shown by the EBSD in Fig. 3.3.10a. The UC decrease provides a less heterogeneous microstructure package, thus promoting higher toughness in this bainitic steel, due to the lower UC distributions, as seen in Fig. 3.3.11a.

The hot forging at 1030 °C, promoted a greater fraction of polygonal ferrite, which, according to [8], results in a chemical heterogeneity in the remaining austenite. This phenomenon causes the formation of martensite in regions with lower concentrations of carbon and alloying elements [31]. This composition heterogeneity is more predominant in R2, which favored the increase in the strength, and at the same time in elongation due to the small grain size packet formed, as can be seen in Fig. 3.3.19b.

### 3.3.5 Conclusion

This work employed the semi-empirical JMAK models to simulate the recrystallization and grain growth after closed die forging for new continuously cooled bainitic steels. The influence of hot forging temperatures on local micro tensile strength and ductility (toughness) by Charpy V-notch tests were also verified. The following conclusions could be drawn:

- Grain growth exponent, which depend on activation energy as well as geometric, and frequency factors, based on the Arrhenius relationship can vary during the heating and forging steps. Due to the variation of the recrystallized grain size distribution (Fig. 10) according to temperature, different exponent values ( $m$ ) were determined. The results of grain growth after recrystallization were, therefore, closer considering the temperature variation.

- From the numerical simulation results, adiabatic heating, caused by high strain rates and plastic deformation may be primarily responsible for the rapid grain growth in forging. It was also observed that in hot forging below 1130 °C, the austenitic grain size was more refined and abnormal grain growth was absent. This leads us to believe that there is no influence on the variation of the exponent  $m$  at temperatures below 1100 °C.

- The hot forging results below 1130 °C led to higher austenitic grain refinement and no abnormal austenitic grain growth. This confirmed previous results in forging tests using a hydraulic press.

- The austenitic grain size favored the formation of different morphologies of bainite, and at forging temperatures below 1100 °C, more refined grains were formed and consequently higher fraction of granular bainite.

- The localized variations of the bainitic microstructure resulted in different mechanical properties. The temperature of 1030°C in R2 achieved the highest yield strength and the highest ratio between tensile strength and maximum stress, while the toughness could be improved, compared to forging at 1130 °C.

- These results showed us that even a temperature variation of around to 100 °C, the control of the temperature forging has a significant impact on the mechanical properties, and that the numerical simulation is an efficient tool to determine and optimize the austenitic grain evolution.

## **Acknowledgement**

The authors acknowledge the Brazilian agency CAPES (Project 1844/2017) and the *Deutsch Forschungsgemeinschaft* (German Research Foundation – DFG) via project EP 128/6-2 (Project number 327887503) for the financial support within the BRAGECRIM program (Brazilian German Cooperation Research in Manufacturing). The authors also thank the *INPEL S.A* industry

for the research partnership. To Metal Forming Institute IBF- RWTH Aachen in Germany for the support during experimental data acquisition. Thiago M. Ivaniski and Alexandre da S. Rocha also acknowledge CNPq (process numbers 167948/2017-2 and 308773/2018-7) for the grants.

### 3.3.6 References

- [1] Shimanov, M. et al. Bainitic steels, their characteristics and applications. *Key Engineering Materials*, [s. l.], v. 684, p. 104–110, 2016. Available from: <https://doi.org/10.4028/www.scientific.net/KEM.684.104>
- [2] Caballero, F. G.; Capdevila, C.; Chao, J. The Microstructure of Continuously Cooled Tough Bainitic Steels. 2nd International Conference of Super-High Strength Steels, [s. l.], p. 10–18, Congress; 2010, Oct 27–30; Verona, Italy.
- [3] Roelofs, H. et al. Continuously cooled bainitic steel HSX ® Z12: one decade of experience. 4th Int. Conf. On Steels in Cars and Trucks, 2014, [s. l.], Congress; 2014, Jun 15 – 19; Braunschweig, Germany.
- [4] Caballero, F.G.; Garcia-Mateo, C.; Cornide, J.; Allain, S.; Puerta, J.; Crouvizer, M.; Mastrorillo, T.; Jantzen, L.; Vuorinen, E.; Lindgren, L.E.; et al. New Advanced Ultra High Strength Bainitic Steels: Ductility and Formability. *Res. Fund Coal Steel Eur. Commission* 2013, 1–124. Available from: <https://op.europa.eu/en/publication-detail/-/publication/9f8dc6ba-d882-48da-9b7b-aa8d7f00dd24>.
- [5] Lan HF, Du LX, Li Q, Qiu CL, Li JP, Misra RDK. Improvement of strength-toughness combination in austempered low carbon bainitic steel: The key role of refining prior austenite grain size. *J Alloys Compd.* 2017;710:702–10.
- [6] Lemos Bevilaqua W, Epp J, Meyer H, Da Silva Rocha A, Roelofs H. In Situ Investigation of the Bainitic Transformation from Deformed Austenite During Continuous Cooling in a Low Carbon Mn-Si-Cr-Mo Steel. *Metall Mater Trans A Phys Metall Mater Sci.* 2020;51(7):3627–37.

- [7] Hatwig RA, Dong J, Epp J, Rocha A da S. Effect of Compressive Deformations on the Final Microstructure of a Low Carbon High Silicon Bainitic Steel Thermomechanically Processed. *Mater Res*. 2021;24(1):1–7.
- [8] Silveira AC de F, Bevilaqua WL, Dias VW, de Castro PJ, Epp J, Rocha A da S. Influence of Hot Forging Parameters on a Low Carbon Continuous Cooling Bainitic Steel Microstructure. *Metals (Basel)* [Internet]. 2020;10(5):601. Available from: <https://www.mdpi.com/2075-4701/10/5/601>.
- [9] Ivaniski T.M, de Souza T, F., Épp J, Rocha A da S. Constitutive Modelling of High Temperature Flow Behaviour for a Low Carbon High Silicon Bainitic Steel. *Mater Res*. 2020;23(5).
- [10] Jonas JJ, Queleñec X, Jiang L, Martin É. The Avrami kinetics of dynamic recrystallization. *Acta Mater*. 2009;57(9):2748–56.
- [11] Irani M, Lim S, Joun M. Experimental and numerical study on the temperature sensitivity of the dynamic recrystallization activation energy and strain rate exponent in the JMAK model. *J Mater Res Technol* [Internet]. 2018;(December). Available from: <https://doi.org/10.1016/j.jmrt.2018.11.007>.
- [12] Razali MK, Joun M. A new approach of predicting dynamic recrystallization using directly a flow stress model and its application to medium Mn steel. *J Mater Res Technol* [Internet]. 2021;11:18:81–94. Available from: <https://doi.org/10.1016/j.jmrt.2021.02.026>.
- [13] Chamanfar A, Chentouf SM, Jahazi M, Lapierre-Boire L-P. Austenite grain growth and hot deformation behavior in a medium carbon low alloy steel. *J Mater Res Technol* [Internet]. 2020;9(6):121:02–14. Available from: <https://doi.org/10.1016/j.jmrt.2020.08.114>
- [14] Moraes ALI, Balancin O. Numerical Simulation of Hot Closed Die Forging of a Low Carbon Steel Coupled with Microstructure Evolution. *Mater Res*. 2015;18(1):92–7.
- [15] Ivaniski T.M, Epp J, Zoch H-W, Da Silva Rocha A. Austenitic grain size prediction in hot forging of a 20mncr5 steel by numerical simulation using the JMAK model for industrial applications. *Mater Res*. 2019;22(5).
- [16] Sellars CM, Whiteman J a. Recrystallization and grain growth in hot rolling. *Met Sci* [Internet]. 1978;13(April):187–94. Available from: <http://www.scopus.com/inward/record.url?eid=2-s2.0-0017938495&partnerID=40&md5=df6c38ede5e9a1ce26344842938e17b2>.

- [17] Henke T, Hirt G, Bambach M. Optimization of a Closed Die Forging Process to Manufacture a Gear Wheel by the Use of a Response Surface Model. *Adv Mater Res.* 2014;922:254–9.
- [18] Koenraad MAJ, George F, Dierk R, Britta N, Ernst K, Miodownik. *Computational Materials Engineering, An Introduction to Microstructure Evolution.* 2007. 359 p.87-89 -181-184.
- [19] JIANGUO, Pietrzyk Maciej Balint Daniel Lin. *Microstructure Evolution in Metal Forming Processes: Modelling and Applications.* [s.l: s.n.]. p.67-74, 2012.
- [20] Castro PJ de, Silveira AC de F, Ivaniski TM, Turra CJ, Epp J, Rocha A da S. Two-Step Continuous Cooling Heat Treatment Applied in a Low Carbon Bainitic Steel. *Mater Res.* 2021;24(2).
- [21] Kashaev N, Horstmann M, Ventzke V, Riekehr S, Huber N. Comparative study of mechanical properties using standard and micro-specimens of base materials Inconel 625, Inconel 718 and Ti-6Al-4 v. *J Mater Res Technol.* 2013;2(1):43–7.
- [22] Vasilyev AA, Sokolov SF, Kolbasnikov NG, Sokolov DF. Effect of alloying on the self-diffusion activation energy in  $\gamma$ -iron. *Phys Solid State.* 2011;53(11):2194–200.
- [23] Guo-Zheng Q, Yang W, Ying-Ying L, Jie Z. Effect of temperatures and strain rates on the average size of grains refined by dynamic recrystallization for as-extruded 42CrMo steel. *Mater Res.* 2013;16(5):1092–105.
- [24] Li X, Ma X, Subramanian S V., Shang C. EBSD characterization of secondary microcracks in the heat affected zone of a X100 pipeline steel weld joint. *Int J Fract.* 2015;193(2):131–9.
- [25] Białobrzaska B, Konat Ł, Jasiński R. The influence of austenite grain size on the mechanical properties of low-alloy steel with boron. *Metals (Basel).* 2017;7(1):1–20.
- [26] Cho SH, Kang KB, Jonas JJ. Dynamic, static and metadynamic recrystallization of a Nb-microalloyed steel. *ISIJ Int.* 2001;41(1):63–9.
- [27] Hodgson, P. D.; Gibbs RK. A Mathematical Model to Predict Hot Rolled C-Mn and Microalloyed the Mechanical Properties of Steels. *ISIJ International*, 1992; 32(12):329–38.
- [28] Banerjee K, Militzer M, Perez M, Wang X. Nonisothermal austenite grain growth kinetics in a microalloyed x80 linepipe steel. *Metall Mater Trans A Phys Metall Mater Sci.* 2010;41(12):3161–72.
- [29] M. Hillert. On the theory of normal and abnormal grain growth. *Acta Metall.*, 13:227, 1965.

- [30] Aranda MM, Kim B, Rementeria R, Capdevila C, De Andrés CG. Effect of prior austenite grain size on pearlite transformation in A hypoeutectoid Fe-C-Mn steel. *Metall Mater Trans A Phys Metall Mater Sci.* 2014;45(4):1778–86.
- [31] A. Lambert, A. Lambert, J. Drillet, A.F. Gourgues, T. Sturel & A. Pineau (2000) Microstructure of martensite–austenite constituents in heat affected zones of high strength low alloy steel welds in relation to toughness properties, *Science and Technology of Welding and Joining*, 5:3, 168-173, DOI: 10.1179/136217100101538164.

## CAPÍTULO 4 - CONCLUSÕES

### 4.1 Conclusões gerais da pesquisa

Embora cada artigo apresentado, que compõe esta tese tenha suas conclusões, a seguir são revisitadas os principais achados e avanços conseguidos com este trabalho. Com a simulação numérica computacional, o efeito de diferentes rotas de forjamento a quente sobre a estrutura dos grãos dos Aços DIN 20MnCr5 e DIN 18MnCrSiMo6-4 foram investigadas sob condições industriais. As seguintes conclusões gerais desta pesquisa, embasado nos resultados e nas discussões dos três artigos publicados, são mostrados a seguir:

No primeiro artigo, a simulação numérica computacional do tamanho de grão austenítico, utilizando o modelo de JMAK após o forjamento a quente, mostrou uma boa concordância com os resultados experimentais para o aço DIN 20MnCr5. Detalhes como a heterogeneidade do tamanho de grão austenítico distribuídas em regiões da peça forjada (recalcada) foram vistas em função das diferentes taxas de deformação e deformação plástica. O parâmetro de Zener-Hollomon mostrou esses efeitos para este aço, porém concluiu-se que, há uma necessidade de melhorias nas condições de contorno, levando em conta a variação das curvas de escoamento causada pela transiência de temperatura.

No segundo artigo, com a estratégia de modelamento já definida no primeiro artigo, constituiu-se algebricamente as equações que descrevem as curvas de escoamento para a implementação de um novo aço bainítico DIN 18MnCrSiMo6-4, em trabalho a quente. Até então, não havia informações detalhadas sobre o comportamento reológico deste aço sob diferentes condições de processamento a quente que permitisse avaliar como este aço poderia ser transformado em forjarias e implementado em simulação computacional. Com o objetivo de melhorar as condições de contorno em processo industrial que envolveu taxas de deformação acima  $50 \text{ s}^{-1}$  no forjamento em matriz fechada, modelou-se a dependência do aumento e da aniquilação das discordâncias durante altas deformações plásticas. Com isso, definiu-se os parâmetros de recristalização e de recuperação dinâmica utilizando JMAK para a implementação dos dados em softwares comerciais de elementos finitos. Pode-se obter uma melhor representação física do comportamento da curva de escoamento plástico deste aço.

No terceiro artigo, regressões não-lineares para obtenção dos parâmetros de JMAK, bem como a implementação das curvas de escoamento plástico do DIN 18MnCrSiMo6-4 foram implementadas no software DEFORM®. Com a melhoria nas condições de contorno, implementado as curvas de escoamento, com o método proposto no Artigo II, um ajuste nos expoentes responsáveis pela cinética de recristalização foi realizado.

Os efeitos causados pela deformação plástica, taxas de deformação e temperatura foram responsáveis por diferentes mecanismos cinéticos de recristalização durante o forjamento a quente. Deu-se o enfoque na distribuição cristalográfica do tamanho destes grãos, vistos em simulação física, que gerou uma hipótese diferente com respeito ao expoente ( $m$ ), dentro da equação que representa o crescimento de grão austenítico após o forjamento em matriz fechada. Foi proposto um método de variação do expoente ( $m$ ) durante o crescimento de grão após o forjamento a quente com base nos resultados da variação da distribuição do tamanho de grão e a temperatura da peça. Os resultados foram mais próximos as do tamanho de grão austenítico experimental em comparação ao modelo utilizado convencionalmente.

Houve um aumento significativo na resistência ao impacto e ao mesmo tempo na relação resistência e ductilidade nas peças forjadas a 1030 °C. Pode-se concluir que este aumento está relacionado ao tamanho de grão austenítico que modifica a morfologia da microestrutura bainítica obtida ao final do processo de forjamento.

Por fim, o aço DIN 18MnCrSiMo6-4 mostra-se promissor para aplicações em forjamento a quente e resfriamento ao ar calmo, pois manteve-se uma microestrutura bainítica com boas propriedades mecânicas. Viu-se que o controle da temperatura é fundamental para manter uma homogeneidade e grãos mais refinados, forjando este aço abaixo de 1030 °C.

## 4.2 Sugestões para trabalhos futuros

Realização de microscopia de transmissão (MET) nas amostras forjadas em diferentes taxas de deformação a fim de constatar que o acúmulo de energia mecânica em altas taxas de deformação é também responsável pela recristalização completa do forjado.

Modelar a fração de perlita poligonal em função do tamanho de grão austenítico.

Elaboração de modelos utilizando Automato Celular (CA) com grandes áreas de ampliação (500 mm x 500 mm) a fim de observar com o uso de modelos de fluxo de calor, diferentes frentes de crescimento de grão após a recristalização de uma peça forjada.

Elaboração de modelos em redes neurais para a determinação direta de parâmetros de recristalização e crescimento de grão em forjarias com a metodologia usada neste trabalho.

Inserir os dados das propriedades mecânicas adquiridas em função dos respectivos microconstituintes presentes após diferentes taxas de resfriamento contínuo, a fim de criar um banco de dados que servirá de auxílio na tomada de decisões nas forjarias.

### 4.3 Referências complementares

AVRAMI, M. Kinetics of phase change, I. General theory. J. Chem. Phys. 1939, 7, 1103–1112.

EPE - EMPRESA DE PESQUISA ENERGÉTICA. Resenha Mensal do Mercado de Energia Elétrica - Janeiro 2020. [S. l.: s. n.], 2020. Available at: [https://www.epe.gov.br/sites-pt/publicacoesdados\\_abertos/publicacoes/PublicacoesArquivos/publicacao-153/topico-510/Resenha Mensal - Janeiro 2020 v4.pdf](https://www.epe.gov.br/sites-pt/publicacoesdados_abertos/publicacoes/PublicacoesArquivos/publicacao-153/topico-510/Resenha%20Mensal%20-%20Janeiro%202020_v4.pdf)

BEVILAQUA, W. L. Observação in situ da reação bainítica durante o resfriamento contínuo em um aço C-Mn-Si-Cr-Mo sob influência de processamento termomecânico. Tese de Doutorado, Universidade Federal do Rio Grande do Sul, Escola de Engenharia; 2021.

BHADESHIA, H. K. D. H. Bainite in Steels Theory and Practice. 3aed. [S. l.: s. n.], 2019.

BLESGEN, T. A variational model for dynamic recrystallization based on Cosserat plasticity, Composites Part B. (2016) 1-8.

BYLYA O, RESHETOV A, STEFANI N, ROSOCHOWSKA M, BLACKWELL P. Applicability of JMAK-type model for predicting microstructural evolution in nickel-based superalloys. Procedia Eng [Internet]. 2017;207 (January):1105–10. Available from: <https://doi.org/10.1016/j.proeng.2017.10.1067>.

COLOMBO, T. C. A; BRITO, A.M.G; SCHAEFFER L. Numerical Simulation of Thermomechanical Processes Coupled with Microstructure Evolution. Comput Sci Eng. 2014;1521-9615/(April):10–5.

CHEN X.; ZHANG J.; DU Y.; WANG G.; HUANG T. Dynamic recrystallization simulation for x12 alloy steel by CA method based on modified L-J dislocation density model. Metals (Basel). 2019;9(12).

DALCIN, RAFAEL LUCIANO; MARQUES DE MENEZES, VALCIR ; OLIVEIRA, LEONARDO FONSECA ; HENRIQUE DA SILVA, CARLOS ; KLEIN DAS NEVES, JULIO CESAR ; THEIS SOARES DIEHL, CARLA ADRIANA ; DA SILVA ROCHA, ALEXANDRE . Improvement on Pitting Wear Resistance of Gears by Controlled Forging and Plasma Nitriding. Journal of Materials Research and Technology-JMR&T, v. 18, p. 4698-4713, 2022.

HAN Y., SUN Y., ZHANG W., CHEN H. Hot deformation and processing window optimization of a 70MnSiCrMo carbide-free bainitic steel. *Materials (Basel)*. 2017;10(3):1–18.

HANAMURA T, TORIZUKA S, TAMURA S, ENOKIDA S, TAKECHI H. Effect of Austenite Grain Size on Transformation Behavior, Microstructure and Mechanical Properties of 0.1C–5Mn Martensitic Steel. *ISIJ Int* [Internet]. 2013;53(12):2218–25. Available from: <http://jlc.jst.go.jp/DN/JST.JSTAGE/isijinternational/53.2218?lang=en&from=CrossRef&type=abstract>.

HALLBERG H. Approaches to Modeling of Recrystallization. *Metals (Basel)* [Internet]. 2011;1(1):16–48. Available from: <http://www.mdpi.com/2075-4701/1/1/16/>.

HIRT G., SCHÄFER D. Phenomenological microstructure simulation of incremental bulk metal forming using a multi mesh method. *AIP Conf Proc*. 2010;1252:1142–9.

HOFER, C. et al. Structural characterization of “carbide-free” bainite in a Fe–0.2C–1.5Si–2.5Mn steel. *Materials Characterization*, [s. l.], v. 102, p. 85–91, 2015. Available at: <https://doi.org/10.1016/j.matchar.2015.02.020>. Acesso em: 23 nov. 2020.

HU F., HODGSON P.D., WU K.M. Acceleration of the super bainite transformation through a coarse austenite grain size. *Mater Lett*. 2014;122:240–3.

JOHNSON, W.; MEHL, R. Reaction kinetics in processes of nucleation and growth. *Trans. Am. Inst. Min. Metall. Eng.* 1939, 135, 416–458.

KOLMOGOROV, A. Statistical theory of crystallization of metals (in Russian). *Bull. Acad. Sci. USSR Ser. Math.* 1937, 1, 355–359.

LI, B. et al. Effect of M–A constituents formed in thermo-mechanical controlled process on toughness of 20CrNi2MoV steel. *Journal of Iron and Steel Research International*, [s. l.], v. 26, p. 1340–1349, 2019. Available at: <https://doi.org/10.1007/s42243-019-00244-8>

MENEZES, V. M. Estudo para manufatura energeticamente eficiente de engrenagens através do emprego de aço bainítico de resfriamento contínuo. Dissertação de Mestrado, Universidade Federal do Rio Grande do Sul, Escola de Engenharia; 2021.

PEROZZO T. Análise da influência dos parâmetros de processo no processamento termomecânicos de aços bainíticos por dilatométrica. Dissertação de Mestrado, Universidade Federal do Rio Grande do Sul, Escola de Engenharia; 2019.

RAMACHANDRAN, D. C. et al. Classification of martensite-austenite constituents according to its internal morphology in high-strength low alloy steel. *Materials Letters*, [s. l.], v. 278, p. 128422, 2020. Available at: <https://doi.org/10.1016/j.matlet.2020.128422>

SILVEIRA A.C de F. Estudo para Aplicação do Aço Bainítico de Resfriamento Contínuo DIN 18MnCrSiMo6-4 em forjamento a quente. Dissertação de Mestrado, Escola de Engenharia, Universidade Federal do Rio Grande do Sul; 2019.

SILVEIRA, ANTONIO CARLOS DE FIGUEIREDO ; BEVILAQUA, WILLIAM LEMOS ; DIAS, VINICIUS WAECHTER ; DE CASTRO, PEDRO JOSÉ ; EPP, JEREMY ; Rocha, Alexandre da Silva . Influence of Hot Forging Parameters on a Low Carbon Continuous Cooling Bainitic Steel Microstructure. *Metals*, v. 10, p. 601, 2020.

SOURMAIL, T. Bainite and Superbainite in Long Products and Forged Applications. *HTM Journal of Heat Treatment and Materials*, [s. l.], v. 72, n. 6, p. 371–378, 2017. Disponível em: <<http://www.hanser-elibrary.com/doi/10.3139/105.110342>>.

TAKAYAMA, N.; MIYAMOTO, G.; FURUHARA, T. Chemistry and three-dimensional morphology of martensite-austenite constituent in the bainite structure of low-carbon low-alloy steels. *Acta Materialia*, [s. l.], v. 145, p. 154–164, 2018. Available at: <https://doi.org/10.1016/j.actamat.2017.11.036>

TURRA C.J. Caracterização Mecânica e Metalúrgica De Um Aço Bainítico De Resfriamento Contínuo Aplicado no Processo Industrial de Forjamento a Quente. Dissertação de Mestrado, Escola de Engenharia, UFRGS; 2021. Disponível em: <https://lume.ufrgs.br/handle/10183/231572>

XU, D. et al. A new study on the growth behavior of austenite grains during heating processes. *Scientific Reports*, [s. l.], v. 7, n. 1, p. 1–13, 2017. Available at: <https://doi.org/10.1038/s41598-017-04371-8>

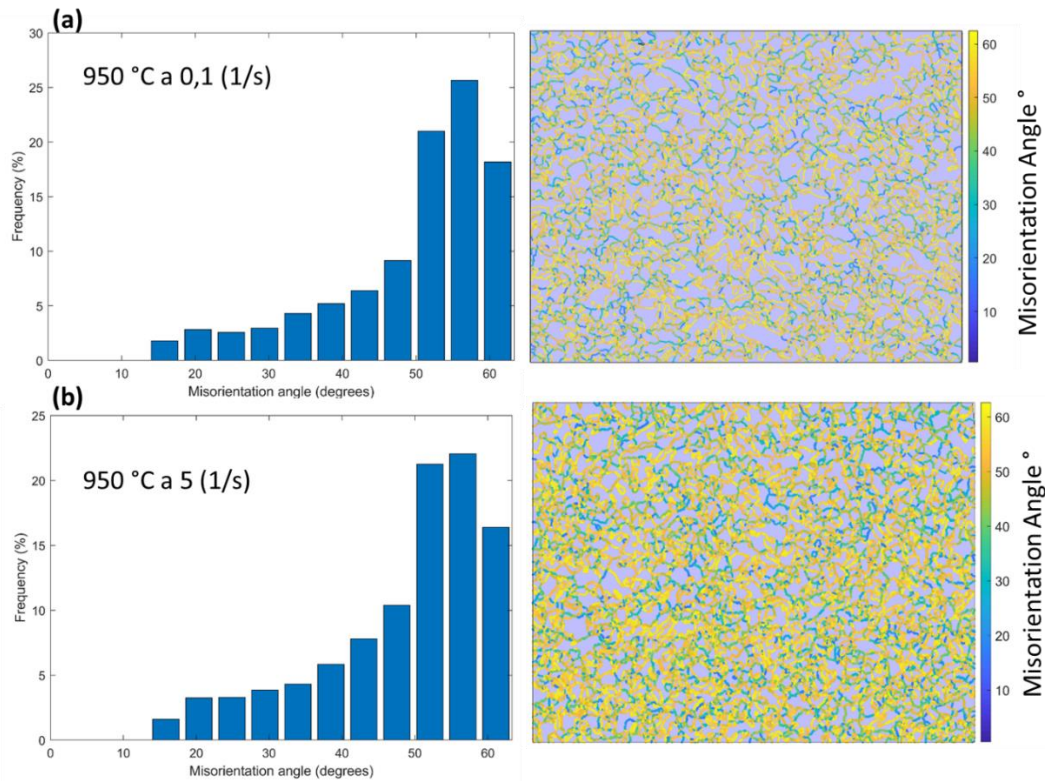
XU, Z. et al. Mechanical properties of a microalloyed bainitic steel after hot forging and tempering. *Journal of Iron and Steel Research International*, [s. l.], v. 24, n. 11, p. 1085–1094, 2017. Available at: [https://doi.org/10.1016/S1006-706X\(17\)30158-9](https://doi.org/10.1016/S1006-706X(17)30158-9)

ZOUARI, M.; BOZZOLO N.; LOGE R. E., Mean field modelling of dynamic and post-dynamic recrystallization during hot deformation of Inconel718 in the absence of  $\delta$  phase particles, *Materials Science&Engineering A*. 655 (2016) 408–424.

## APÊNDICE 1A Difração de Elétron Retroespalhados (*Back Scattering Diffraction- 'EBSD)* por microscopia eletrônica de varredura (MEV)

No **Apêndice 1A** são mostrados alguns resultados experimentais obtidos pela microscopia ótica e MEV-EBSD. Nos ensaios de EBSD, constatou-se que houve recristalização dinâmica descontínua, como já estimado nas condições analisadas durante a simulação física e corroboraram com os resultados publicados no Artigo 2 e Artigo 3. O dados foram tratados utilizando o pacote de análise “*Misorientation*” do MTEX <https://mte-toolbox.github.io/MisorientationTheory.html> que mostram os contornos de (baixo  $2^\circ < \theta < 15^\circ$ ) e alto ângulo ( $\theta > 15^\circ$ ).

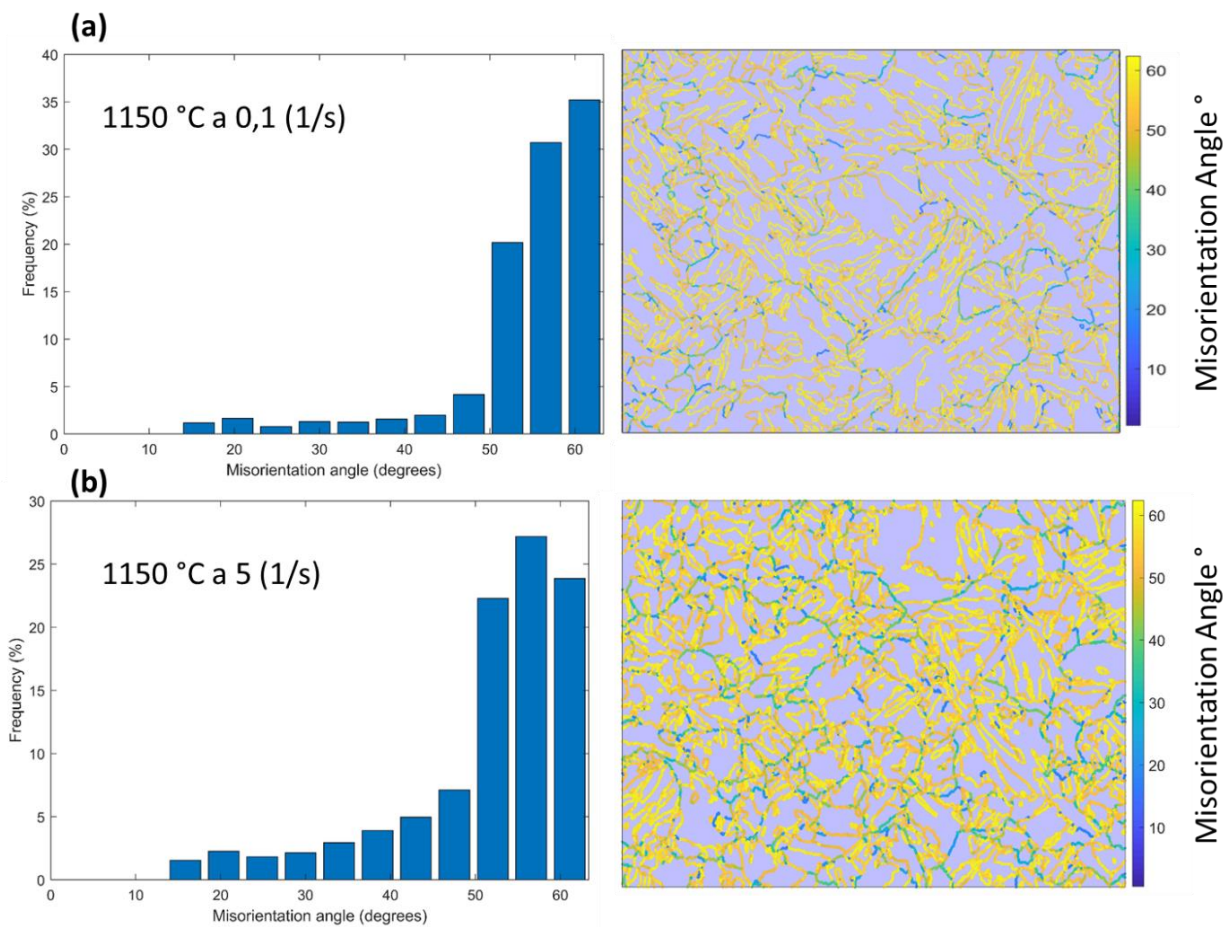
Análise de *EBSD* das amostras comprimidas a  $950^\circ\text{C}$  nas taxas de deformação de  $0,1\text{ s}^{-1}$  e  $5\text{ s}^{-1}$  mostrando o ângulo de desorientação dos contornos de grão.



Fonte: O autor.

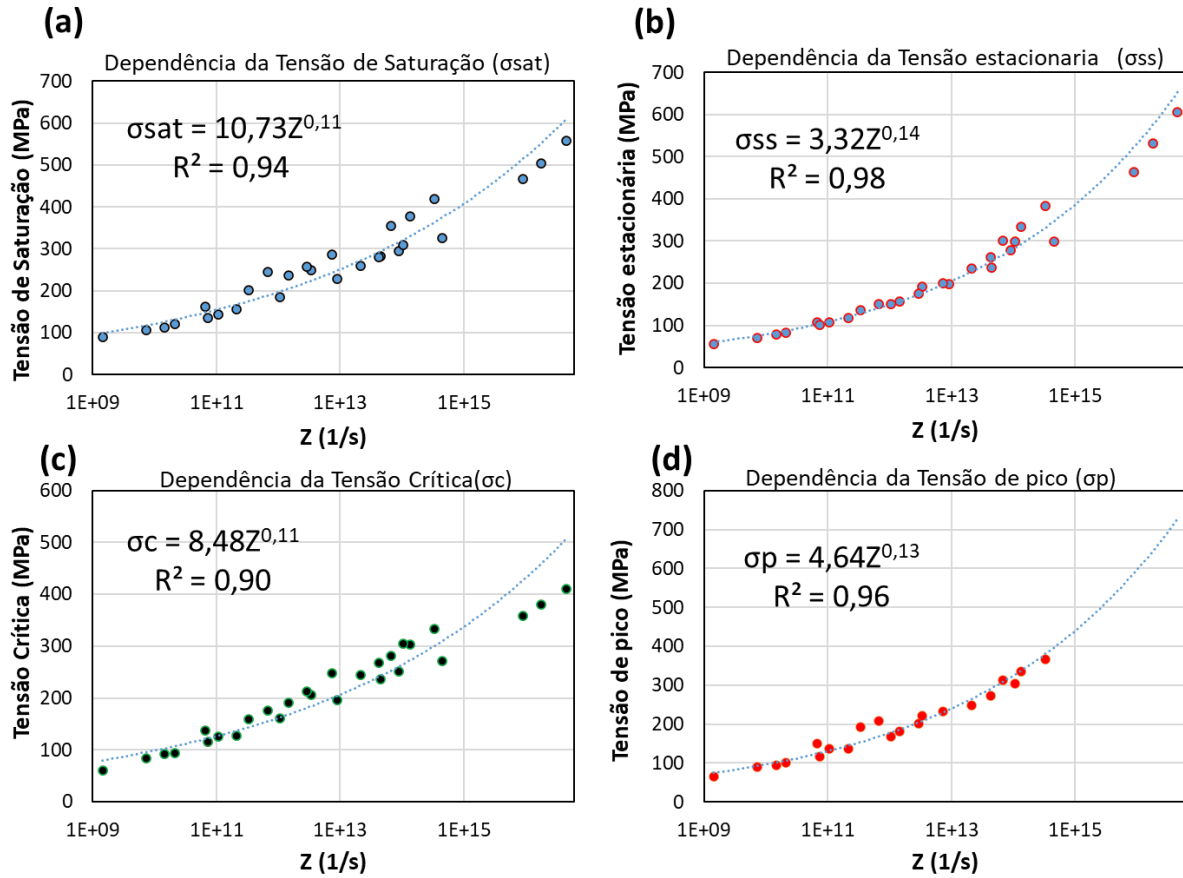
Percebe-se que o acúmulo de energia mecânica e o aquecimento adiabático fez com que gerassem contornos de grão de alto ângulo (HAGB) em taxas de deformação de  $5\text{ s}^{-1}$ . Isso fará com que a taxa de nucleação, ou seja, a cinética de recristalização seja mais rápida.

Análise de *EBS*D das amostras comprimidas a 1150 °C nas taxas de deformação de 0,1 s<sup>-1</sup> e 5 s<sup>-1</sup> mostrando o ângulo de desorientação dos contornos de grão.



Fonte: O autor.

Parâmetros dependentes para o cálculo das tensões em cada incremento de deformação plástica nas curvas de escoamento em função do parâmetro Z.

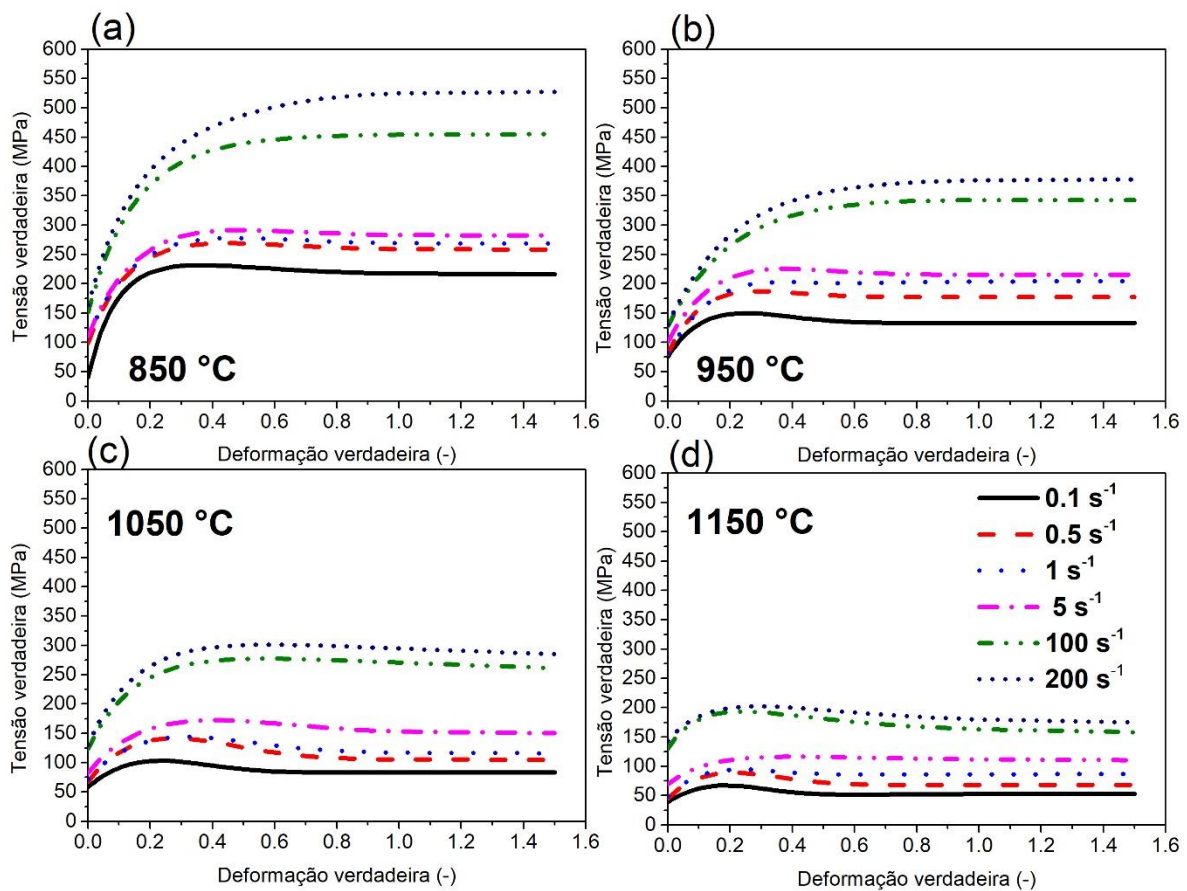


Fonte: O autor.

## APÊNDICE 1B Curvas de Escoamento e Validação da Força de Recalque

No **Apêndice 1B** é mostrado as curvas de escoamento modelados e inseridos no banco de dados dos softwares DEFORM® e QFORM UK®, bem como é mostrado a comparação da força de recalque cilíndrico versus o deslocamento em três condições de temperaturas.

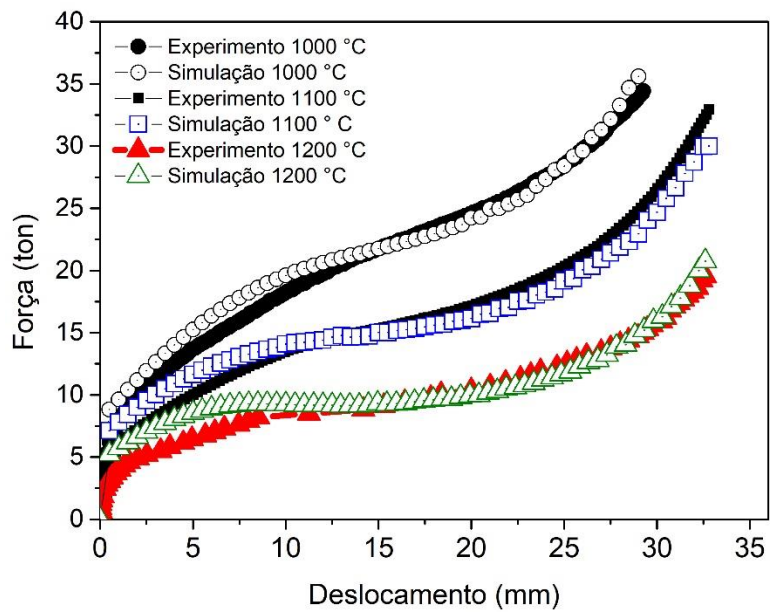
Curvas de escoamento plástico da austenita para o aço DIN 18MnCrSiMo6-4 modeladas e inseridas nos software DEFORM® e QFORM®.



Fonte: O autor.

Podemos perceber que há uma boa concordância nos resultados experimentais medidos com os resultados da simulação numérica, uma vez calibrada de forma adequada.

Comparação das forças de forjamento 4 (recalque cilíndrico) do Aço DIN 18MnCrSiMo6-em três temperaturas.



Fonte: o autor.

## APÊNDICE 1C Implementação de uma nova sub-rotina no software QFORM UK.

Subrotina escrita em linguagem (.lua) implementado no software comercial Qform UK para a determinação do tamanho de grão austenítico junto a variação do parâmetro ( $m$ ) de crescimento de grão e tamanho de grão ferrítico nos contornos de grão.

---



---

-- This subroutine was used to determine dynamic recrystallization and austenitic grain growth by dislocation density model. By Thiago M. Ivaniski.

```
if can_debug() then
```

```
    require('mobdebug').start()
```

```
end
```

```
set_target_workpiece()
```

```
r = 8.314 -- Gas constant
```

```
-- Parameters os saturations stress calculation (Ssat)
```

```
c1 = parameter("c1", 0.0154) -- coefficient of saturation stress
```

```
c2 = parameter("c2", 2.8469) -- exponent of saturation stress
```

```
qT = parameter("qT", 276864) -- Total activation energy (J/mol.K)
```

```
-- Parameters of Mean Free Path dislocations during the plastic strain
```

```
r1 = parameter("r1", 1.01e+03) -- Average recovery parameter for (0.1 to 200 1/s strain rate)
```

```
u = parameter("u", 3.6e+09) -- Shear Modulus (Pa)
```

```
b11 = parameter("b11", 3.6e-10) -- Burguer's Vector (m)
```

```
alpha = parameter("alpha", 9800) -- Regulation peak stress parameter (Pa-1)
```

M = parameter("M", 3) -- Taylor Factor

-- Parameters peak strain

a1 = parameter("a1", 0.00479)

a2 = parameter("a2", 0.54)

m1 = parameter("m1", 0.1238)

n1 = parameter("n1", 0)

q1 = parameter("q1", 45000)

d0 = parameter("d0", 45)

-- Parameters of dynamic recrystallization XDRX

a5 = parameter("a5", 0.0627)

h5 = parameter("h5", 0.32)

m5 = parameter("m5", 0.03)

n5 = parameter("n5", 0)

q5 = parameter("q5", 5200)

a10 = parameter("a10", 0)

beta = parameter("beta", -0.697) -- Avrami coefficient for dynamic recrystallization

kd = parameter("kd", 1.798) -- Avrami exponent Xdrx

-- DRX grain size

a8 = parameter("a8", 8103)

h8 = parameter("h8", 0)

m8 = parameter("m8", -0.16)

n8 = parameter("n8", 0)

q8 = parameter("q8", -74880)

-- Parameters of Metadynamic recrystallization MDRX

beta\_m = parameter("beta\_m", -0.693147) -- Avrami coefficient for metadynamic recrystallization

kdm = parameter ("kdm", 1.79) -- Avrami exponent Xmdrx

a4 = parameter("a4", 2.13e-06)

n4 = parameter("n4", 0)

m4 = parameter("m4", -0.62)

h4 = parameter("h4", 0)

q4 = parameter("q4", 133000)

-- MDRX grain size

a7 = parameter("a7", 1804.6)

h7 = parameter("h7", 0.63)

n7 = parameter("n7", -0.25)

m7 = parameter("m7", -0.12)

q7 = parameter("q7", -73778)

-- Strain rate boundary parameter to activate SRX

A = parameter("A", 0.001)

c11 = parameter("c11", 0)

c22 = parameter("c22", 0)

q2 = parameter("q2", 0)

-- Parameters of Static recrystallization SRX

beta\_s = parameter("beta\_s", -0.597) -- Avrami coefficient for SRX

kds = parameter ("kds", 1.798) -- Avrami exponent Srx

a3 = parameter ("a3", 2.5e-19)

```
h3 = parameter("h3", 2)
n3 = parameter("n3", -4)
m3 = parameter("m3", 0)
q3 = parameter("q3", 270000)

-- SRX grain size

a6 = parameter("a6",0.5)
h6 = parameter("h6", 0.67)
n6 = parameter("n6", -1)
m6 = parameter("m6", 0)
q6 = parameter("q6", 0)

-- Grain growth parameters

q9 = parameter("q9", 296000)
a9 = parameter ("a9", 4.48e+16)
a = parameter ("a", 0.3448)
b = parameter ("b", 0.0022)

-- Declaring user-defined fields

ec = result("ec", 0)
ecMax = result("ecMax", 0)
ep = result("ep", 0)
epMax = result("epMax", 0)
e_05 = result("e_05" , 0)
t_05m = result("t_05m", 0)
t_05s = result("t_05s", 0)
```

```

xdrx = result("xdrx", 0)
xmdrx = result("xmdrx", 0)
srx = result ("srx", 0)
ddrx = result("ddrx", 0)
dmdrx = result("dmdrx", 0)
dsrx = result("dsrx", 0)
ddrxavg = result("ddrxavg", 0)
Ssat = result("Ssat", 0)
h = result("h", 0)
rho = result("rho", 0)
m = result ("m", 0)
Grain_Growth = result("Grain_Growth", 0)
rate_of_T = result("rate_of_T", 0)
Zener_Hollomon = result ("Zener_Hollomon" , 0)
Dislocation_Stress = result ("Dislocation_Stress", 0)

```

**function UserFields** (prev\_ecMax, prev\_epMax, T, t, dt, strain\_plast, strain\_rate, prev\_e\_05, prev\_t\_05m, prev\_t\_05s, prev\_xdrx, prev\_xmdrx, prev\_srx, prev\_ddrx, prev\_dmdrx, prev\_dsrx, prev\_ddrxavg, stress\_flow, prev\_Ssat, prev\_T, prev\_h, prev\_rho, prev\_Zener\_Hollomon, prev\_Dislocation\_Stress)

```
-- Conversion of degrees Centigrade into degrees Kelvin
```

```
T = T + 273.15
```

```
-- Computation of Z parameter
```

```
Zener_HollomonTemp = 0
```

```
Zener_HollomonTemp = strain_rate * math.exp(qT / (r * T))
```

```
-- Computation of critical and peak strain
```

epTemp = 0

epTemp = a1 \* (d0 ^ n1) \* (strain\_rate ^ m1) \* math.exp(q1 / (r \* T))

epMaxTemp = math.max(prev\_epMax, epTemp)

ecTemp = 0

ecTemp = a2 \* epTemp

ecMaxTemp = math.max(prev\_ecMax, ecTemp)

-- Computation of Saturation Stress (Ssat)

SsatTemp = 0

SsatTemp = (c1 \* (math.log (strain\_rate \* math.exp (qT / (r \* T))))^c2)

-- Computation of Dislocation Density

hTemp = 0

hTemp = r1 \* (((SsatTemp ^ 2) \* 1e6) / ((alpha \* u \* b11) ^ 2))

rhoTemp = 0

rhoTemp = (stress\_flow ^ 2) / (M \* alpha \* u \* b11) ^ 2

-- Computation of Flow stress from dislocation density

Dislocation\_StressTemp = 0

Dislocation\_StressTemp = (((M \* alpha \* u \* b11) ^ 2) \* rhoTemp) ^ 0.5

-- Computation of 50% of Xdrx (e\_05)

e\_05Temp = 0

e\_05Temp = a5 \* (d0 ^ h5) \* (strain\_rate ^ m5) \* (strain\_plast ^ n5) \* math.exp (q5 / (r \* T))

-- Computation of time for 50% of XMDRX

t\_05mTemp = 0

t\_05mTemp = a4 \* (strain\_plast ^ n4) \* (d0 ^ h4) \* (strain\_rate ^ m4) \* math.exp (q4/(r \* T))

-- Computation of time for 50% of SRX

t\_05sTemp = 0

t\_05sTemp = a4 \* (strain\_plast ^ n3) \* (d0 ^ h3) \* (strain\_rate ^ m3) \* math.exp (q3/(r \* T))

-- Computation of Xdrx

xdrxTemp = 0

xdrxTemp = 1 - math.exp (beta\* (strain\_plast - epTemp \* a10 / e\_05Temp) ^ kd)

-- Computation of MXDRX

xmdrxTemp = 0

xmdrxTemp = 1 - math.exp (beta\_m \* (dt / t\_05mTemp) ^ kdm)

-- Computation of SRX

srxTemp = 0

```
srxTemp = 1 - math.exp(beta_s * (dt / t_05sTemp) ^ kds)
```

```
-- Computation of DRX grain size
```

```
ddrxTemp = 0
```

```
ddrxTemp = a8 * (d0 ^ h8) * (strain_rate ^ m8) * (strain_plast ^ n8) * math.exp(q8 / (r * T))
```

```
-- Computation of MDRX grain size
```

```
dmdrxTemp = 0
```

```
dmdrxTemp = a7 * (d0 ^ h7) * (strain_rate ^ m7) * (strain_plast ^ n7) * math.exp(q7 / (r * T))
```

```
--dmdrxtTemp = 1.5 * ddrxTemp
```

```
-- Computation of DSRX grain size
```

```
dsrxTemp = 0
```

```
dsrxTemp = a6 * (d0 ^ h6) * (strain_rate ^ m6) * (strain_plast ^ n6) * math.exp(q6 / (r * T))
```

```
-- Computation of DRX Average Grain Size
```

```
ddrxavgTemp = 0
```

```
ddrxavgTemp = xdrxTemp * ddrxTemp + (1 - xdrxTemp) * d0
```

```
-- Computation of Grain Growth
```

```
mTemp = 0
```

```
mTemp = a * math.exp(b * T)
```

```

Grain_GrowthTemp = 0
Grain_GrowthTemp = ((ddrxavgTemp ^ mTemp + a9 * math.exp (- q9 / (r * T)) * t) ^ (1 / mTemp)

-- Saving the variable for the field

store(ec, ecTemp)
store(ecMax, ecMaxTemp)
store(ep, epTemp)
store(epMax, epMaxTemp)
store(e_05, e_05Temp)
store(t_05m, t_05mTemp)
store(t_05s, t_05sTemp)
store(xdrx, xdrxTemp)
store(xmdrx, xmdrxTemp)
store(srx, srxTemp)
store(ddrx, ddrxTemp)
store(dmdrx, dmdrxTemp)
store(dsrx, dsrxTemp)
store(ddrxavg, ddrxavgTemp)
store(Ssat, SsatTemp)
store(h, hTemp)
store(rho, rhoTemp)
store(rate_of_T, rT)
store(Grain_Growth, Grain_GrowthTemp)
store (m, mTemp)
store(Zener_Hollomon, Zener_HollomonTemp)
store(Dislocation_Stress, Dislocation_StressTemp)

end

#####

```

De maneira algébrica, a implementação da sub-rotina que considera a densidade de discordâncias durante o forjamento é mostrado na equação abaixo, conforme Estrin-Mecking:

$$\rho = \frac{\sigma_{eq}^2}{(M\alpha\mu b)^2}$$

Onde,  $\sigma_{eq}$ , é a tensão equivalente de Von Mises, calculada pela sub-rotina do software, com base nas curvas de escoamento implementadas para o DIN 18MnCrSiMo6-4. O  $M$ , é o fator de Taylor, igual 3,  $\alpha$  uma constante do material (0,009837),  $\mu$  o módulo de cisalhamento (32,02 GPa) e  $b$  o vetor de Burgers (0,36 nm).

A tensão de saturação e a de encruamento, previamente determinada (Artigo II), permitiu a implementação das equações que descrevem a densidade de discordâncias média no software QFORM UK durante o início da deformação plástica, bem como quando o acúmulo e a aniquilação de discordâncias quando entram em seu regime de saturação:

$$\rho_c = \frac{\sigma_c^2}{(M\alpha\mu b)^2}$$

$$\rho_0 = \frac{\sigma_0^2}{(M\alpha\mu b)^2}$$

$$\rho_{sat} = \frac{\sigma_{sat}^2}{(M\alpha\mu b)^2}$$

Onde  $\rho_0$ ,  $\rho_c$ ,  $\rho_{sat}$  são a densidade de discordância inicial, crítica e de saturação, respectivamente. O  $r$  e o  $h$ , são os parâmetros de recuperação dinâmica e de encruamento, obtidos no Artigo II. Finalmente, calcula-se pelas equações abaixo, a densidade de discordância no estágio de encruamento e na recristalização:

$$\rho_{WH} = \rho_{sat} - (\rho_{sat} - \rho_0)\exp[-r(\varepsilon - \varepsilon_0)]$$

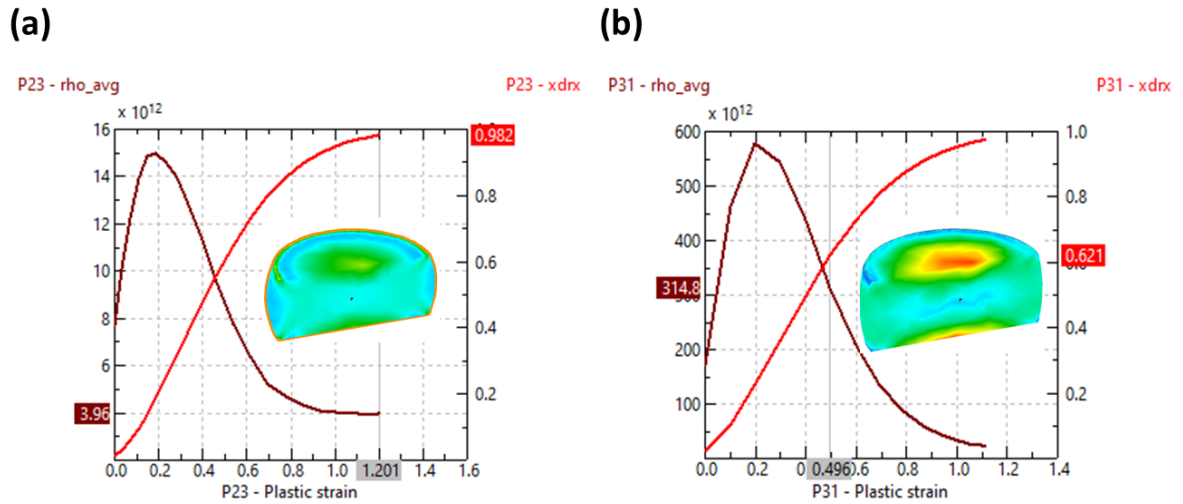
$$\rho_{xdrx} = \rho_c - (\rho_c - \rho_0)\exp[-h(\varepsilon - \varepsilon_c)]$$

E pela regra da mistura, calcula-se a densidade de discordâncias média:

$$\bar{\rho} = (1 - XDRX)\rho_{WH} + XDRX\rho_{xdrx}$$

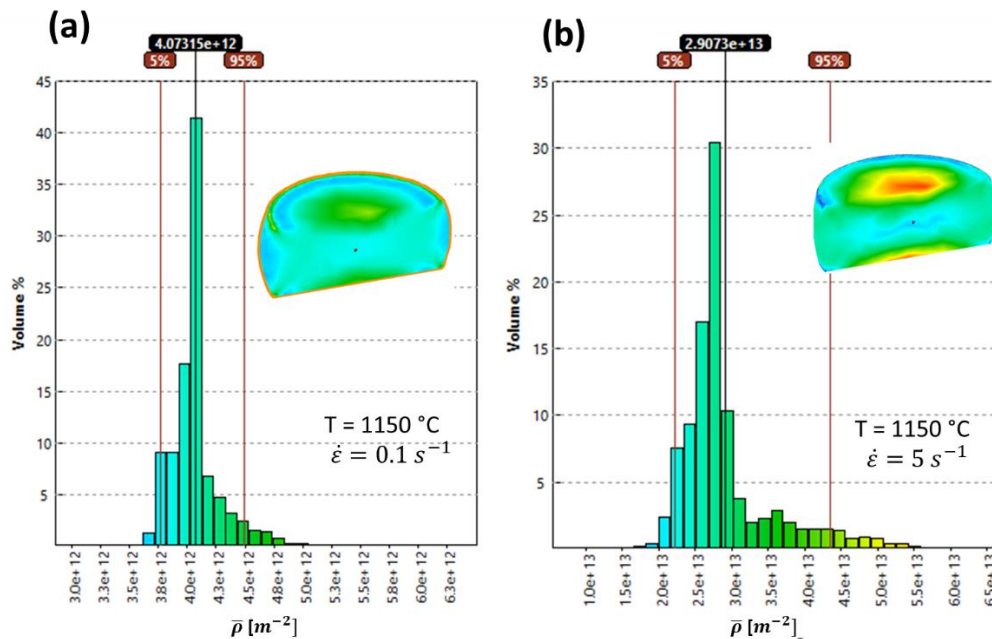
A Figura abaixo mostra a densidade de discordâncias média com relação a fração recristalizada *XDRX*.

Varição da densidade de discordâncias ( $m^{-2}$ ) e fração recristalizada *XDRX* durante a compressão axial do DIN 18MnCrSiMo6-4 (a) a  $0,1 s^{-1}$  e (b)  $5 s^{-1}$ .



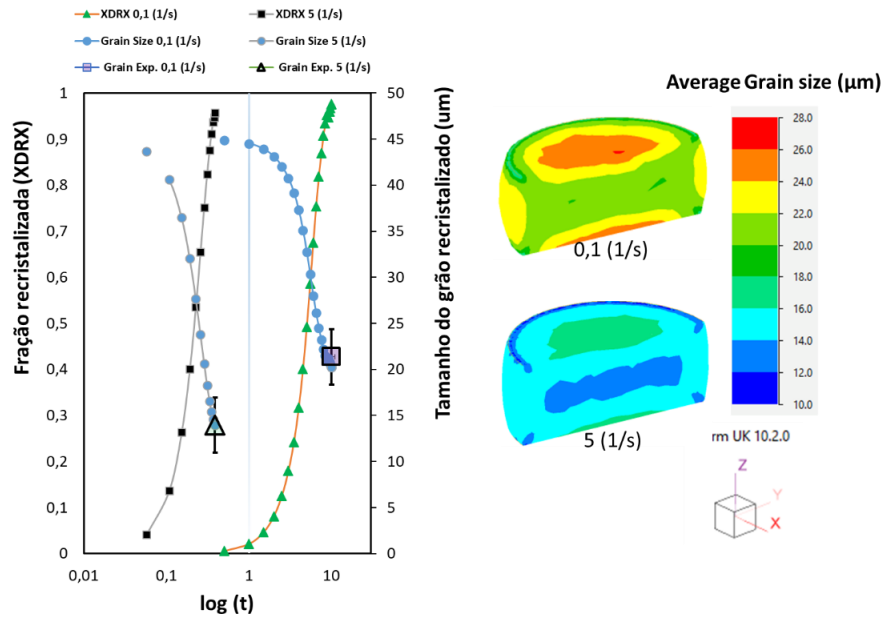
Fonte: O autor.

Densidade de discordâncias média do aço DIN 18MnCrSiMo6-4 na fase austenítica implementada na sub-rotina.



Fonte: O autor.

Evolução da fração recristalizada e tamanho de grão austenítico implementado na sub-rotina do software Qform UK



Fonte: O autor.